Electronic Properties of (Pseudo-) Two-Dimensional Materials

Janssen, V.A.E.C.

DOI
10.4233/uuid:0c9f992c-7390-4d8f-aa6d-d89f0e7866a0

Publication date
2020

Document Version
Final published version

Citation (APA)
Janssen, V. A. E. C. (2020). *Electronic Properties of (Pseudo-) Two-Dimensional Materials*. [Dissertation (TU Delft), Delft University of Technology]. https://doi.org/10.4233/uuid:0c9f992c-7390-4d8f-aa6d-d89f0e7866a0

Electronic Properties of (Pseudo-) Two-Dimensional Materials

Electronic Properties of (Pseudo-) Two-Dimensional Materials

Proefschrift

ter verkrijging van de graad van doctor
aan de Technische Universiteit Delft,
op gezag van de Rector Magnificus Prof.dr.ir. T.H.J.J. van der Hagen,
voorzitter van het College voor Promoties,
in het openbaar te verdedigen op maandaf 21 september 2020 om 10:00 uur.

door

Vera Apolonia Emerentiana Clara JANSSEN

Master of Science in Physics,
Universiteit Leiden, Leiden, Nederland,
geboren te Papendrecht, Nederland.

Dit proefschrift is goedgekeurd door de

promotor: Prof. dr. ir. H.S.J. van der Zant
promotor: Prof. dr. ir. S.J. van der Molen

Samenstelling promotiecommissie:

Rector Magnificus,	voorzitter
Prof. dr. ir. H.S.J. van der Zant,	Technische Universiteit Delft
Prof. dr. ir. S.J. van der Molen,	Universiteit Leiden
Onafhankelijke leden:	
Prof. dr. Y. Blanter,	Technische Universiteit Delft
Prof. dr. D.A.M. Vanmaekelbergh,	Universiteit Utrecht
Prof. dr. ir. T.H. Oosterkamp,	Universiteit Leiden
Dr. A. van Houselt,	Universiteit Twente
Prof. dr. L. Kuipers,	Technische Universiteit Delft, reservelid
Overige leden:	
Dr. J. Jobst,	Demcon

Dr. J. Jobst heeft in belangrijke mate aan de totstandkoming van het proefschrift bijgedragen.

Keywords: 2D materials, low energy electron microscopy (LEEM), angle-resolved reflected-electron spectroscopy (ARRES), nano-crystal supper lattices, transport, ionic-liquid gate.
Printed by: Gildeprint, Enschede
Front & Back: Sybren Renema

Casimir PhD Series, Delft-Leiden 2020-21

ISBN 978-90-8593-448-6

An electronic version of this dissertation is available at
http://repository.tudelft.nl/.

Voor papa

Contents

Summary

This thesis describes research into the interaction between electrons and various (pseudo) two-dimensional materials. This research is using two approaches: in Chapters 3 and 4 a low-energy electron microscope is used, and in Chapters 5 and 6 transport properties are studied.
Chapter 1 introduces the concept of a two-dimensional material. First, the various kinds of such materials are illustrated. Secondly, the specific materials used in this thesis will be treated. We will see that two-dimensionality can be achieved in different ways: first of all top-down in a method where layers are peeled off a crystal until a single atomic layer remains. Secondly: bottom-up, in a method where a single layer is created from smaller components.
Chapter 2 introduces the setup which was used for the measurements in Chapters 3 and 4. In these chapters, we will look at materials using electrons, in a low-energy electron microscope (LEEM). A regular microscope works by illuminating a sample with light. In a microscope, we observe bright and dark patches (corresponding to reflection and absorption of the light, respectively), as well as colors (corresponding to reflection and absorption of different wavelengths or energies of the light). We can also magnify objects using lenses. The LEEM works in a very comparable way, with the major difference that we do not use light (i.e. photons) but electrons to image the sample. An image is formed by electrons after interaction with the sample has taken place. This image can also be magnified, and contains bright and dark patches, from which the interaction of the material with the electrons can be established. Besides this, it is possible to change the electron energy in the setup, which makes it possible to measure the interaction at different energies.
In the third Chapter we use the LEEM's ability to measure the atomic orientation of thin layers of crystal. We look at graphene, a two-dimensional lattice of carbon atoms. This graphene was grown on a wafer. Contrary to peeling a crystal to atomically thin layers, this growth method is compatible with industrial processes, which require large slabs of graphene in predictable shapes. In developing these growing methods, it turns out to be difficult to grow large pieces of single-crystal material. With LEEM we look at differences in angular orientation in a layer of graphene. The motivation for this is that boundaries between such domains have a negative influence on the conductive properties of the material.
In the fourth Chapter a method is extended to measure and visualize band structures in two-dimensional materials. We look specifically at molybdenum disulfide (MoS_2) and hexagonal boron nitride (hBN). The method (scanning ARRES) rapidly scans the electron bream across the first Brillouin zone. This gives a complete image of the band structure of these materials at energies above the Fermi level plus work function.

The fifth and sixth Chapters concern single layer superstructures built out of nanocrystals. The building blocks are lead selenide (PbSe) single crystals in the form of a truncated cube, with a diameter of about 5 nm. By allowing these crystals to organize on a fluid surface, a single layer of crystals emerges. These crystals bond covalently in the direction of the atomic lattice. The material which emerges from this process can have multiple shapes, in this thesis we study the square structure. In Chapter 5 we study the conductance properties of such a structure at room temperature, under the influence of an ionic-fluid gate. This gate makes is possible to achieve high charge densities in these structures. We measure high mobilities for these systems, in the order of 1 cm^2/Vs.
In the sixth Chapter these samples are cooled to approximately 4 K. Despite the high mobilities measured in Chapter 5, the dependence of the conductance with temperature shows that transport is dominated by a hopping process and not by band transport, at the length scale of these samples.

Samenvatting

Dit proefschrift beschrijft onderzoek naar de interactie tussen elektronen en verschillende (pseudo) twee-dimensionale materialen. Dit wordt op twee verschillende manieren gedaan; in hoofdstuk 3 en 4 wordt gebruikgemaakt van een laag energetische electronen microscoop en in hoofdstuk 5 en 6 worden geleidingseigenschappen bestudeerd.
In hoofdstuk 1 wordt het concept twee-dimensionaal materiaal geïntroduceerd. Eerst wordt de verscheidenheid in deze famillie toegelicht. Vervolgens worden de specifieke materialen die in dit proefschrift langskomen beschreven. We zullen zien dat de twee-dimensionaliteit op verschillende manieren kan worden bereikt. Ten eerste top-down, in een methode waarin laagjes van een kristal worden afgepeld, totdat er nog maar een enkele atomaire laag over is. Ten tweede bottom-up, een methode waarin vanuit kleine bouwstenen een enkele laag wordt gecreerd.
In hoofdstuk 2 wordt de opstelling geïntroduceerd die gebruikt is voor de metingen in hoofdstuk 3 en 4. In deze hoofdstukken kijken we naar materialen met behulp van elektronen, gebruikmakend van een *Laag Energetische Elektronen Microscoop* (LEEM). Een reguliere microscoop werkt door een substraat met licht te beschijnen. Daarin observeren we licht (reflectie van het licht), donker (absorptie van het licht) en kleuren (absorptie en reflectie van verschillende golflengten - of energieën - van het licht). Ook kunnen we objecten vergroten, gebruikmakend van lenzen. De LEEM werkt op een heel vergelijkbare manier, met als groot verschil dat we geen lichtbron, of:fotonen, gebruiken om het substraat te bekijken, maar een electronenbron. Er wordt een beeld gevormd door de electronen nadat er interactie met het substraat heeft plaatsgevonden. Dit beeld kan ook een vergroot beeld zijn en bevat donker en licht. Hieruit kan de interactie van het materiaal met de electronen worden vastgesteld. Daarnaast is het mogelijk de electronenenergie te veranderen in de opstelling, waardoor het mogelijk is de interactie op verschillende energieën te meten.
In het derde hoofdstuk wordt gebruik gemaakt van de mogelijkheid van de LEEM om de atomaire oriëntatie van dunne lagen kristal te onderzoeken. Hier wordt gekeken naar grafeen, een twee-dimensionaal rooster van koolstofatomen. Dit grafeen is gegroeid op een wafer. In tegenstelling tot het afpellen van een kristal tot atomaire laagjes is deze groeimethode wel compatibel met industriële processen, waar grote stukken voorspelbaar grafeen voor nodig zijn. In de ontwikkeling van dit soort groeimethodes blijkt het lastig te zijn om grote stukken, enkel-kristallijn materiaal te produceren. Met de LEEM kijken we naar de verschillen in hoekoriëntatie van zo'n laag grafeen, omdat grenzen tussen de verschillende oriëntaties negatieve gevolgen hebben voor de geleidingsprestaties van het materiaal.
In het vierde hoofdstuk wordt een meetmethode uitgebouwd om *bandstructuren* te

meten en te visualiseren van twee-dimensionale materialen. We kijken hier specifiek naar molybdeen disulfide (MoS_2) en hexagonal boornitride (hBN).De meetmethode (scanning ARRES) scant de elektronenbundel op een snelle manier over de volledige eerst Brioullinzone. Dit geeft een volledig beeld van de bandenstructuur van deze materialen op energieën boven het Ferminiveau plus de uittreearbeid.
Het vijfde en het zesde hoofstuk gaan over enkellaags superstructuren opgebouwd uit nanokristallen. De bouwstenen zijn eenkristallen van loodselinide (PbSe) in de vorm van een afgeknotte kubus en een diameter van ongeveer 5 nm. Door deze kristallen op een vloeistofoppervlak de kans te geven zichzelf te organiseren, ontstaat een enkele laag kristallen. Deze kristallen binden zich in de richting van het atomaire rooster covalent aan elkaar. Het materiaal dat ontstaat kan een superstructuur hebben in verschillende vormen, in dit proefschrift bestuderen we de vierkante structuur.
In vijfde hoofdstuk wordt een studie gepresenteerd naar de geleidingseigenschappen van deze structuur bij kamertemperatuur, onder invloed van een ionisch-vloeibare gate. Deze gate maakt het mogelijk om grote ladingsdichtheden te bewerkstelligen in de structuren. We meten hoge mobiliteiten voor dit soort systemen, in de orde van 1 cm^2/Vs.
In het zesde hoofdstuk worden deze substraten afgekoeld tot ongeveer 4 K. Ondanks de hoge mobiliteiten, gemeten in hoofdstuk 5, laat de afhankelijkheid van de geleiding van de temperatuur zien dat het transport wordt gedomineerd door een hoppingproces en dat er geen sprake is van bandtransport, op de schaal van deze samples.

1

Introduction

1

1.1. Dimensionality and electronic properties

The electronic systems that most people encounter in their daily lives are three-dimensional. The cables that transport electricity to our houses are three-dimensional conductors and our computers and phones operate making use of three-dimensional semi-conductor components. One might argue that the dimensions of these systems could put them in another category: the electricity cables on the power grid are much longer than they are wide: does this make them one-dimensional? The components in our phones are smaller and smaller: does this make them zero-dimensional?

The dimensionality of electronic systems does not rely on the intuitive notion of

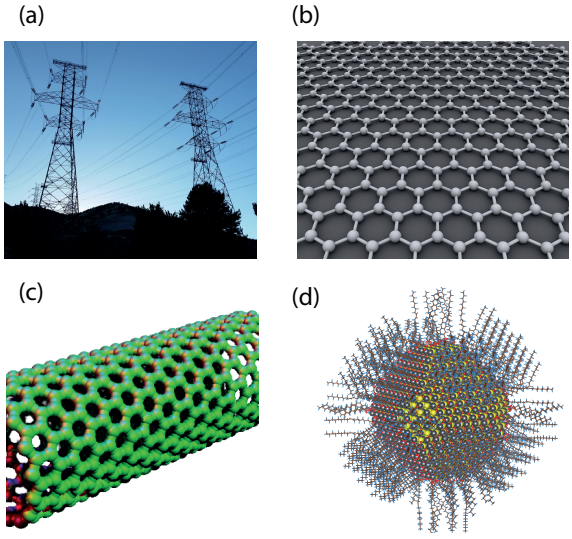

Figure 1.1: Examples of a three-dimensional conductor [1] (a),a two-dimensional conductor, i.e. graphene (b) [2], one dimensional conductor [3] (c), and a quantum dot, i.e. a zero-dimensional structure [4] (d).

dimensionality as defined by aspect ratios. In contrast, it is defined by the dimensionality that charge carriers encounter in their movement. For example, in a two-dimensional (semi-)conductor charge carriers are confined to a plane. An example of systems in which this confinement is reached are extreme -atomic- thinness of materials that show typical two-dimensional transport properties. [5, 6]. An example of such a system is graphene, as depicted in figure 1.1 (b).

In a one-dimensional electronic system the movement of the charge carriers is restricted to a line. Typically this one dimensional behaviour is found in nano-tube systems, like a carbon nanotube as shown in figure 1.1 (c). Here, the absolute dimensions of two out of three directions are of the order of the electron wavelength.

The physics of these systems at low temperature is strongly influenced by their one-dimensional nature, as seen, for example, in the temperature dependance of the conductivity. [7, 8]
Zero-dimensional electronic systems confine the charge carrier to a standing wave with nodes at the extremes only. These zero-dimensional objects are typically referred to as quantum dots - as their electronic properties are dominated by quantum mechanics. Quantum dots come in a large range of materials fabricated with different sythesis methods, like colloidal systems made in chemical labratories [9], as depicted in figure 1.1 (d) and semi-conductor *on-chip* systems fabricated in cleanrooms [10].
We will focus our attention to two-dimensional materials. The isolation of graphene [11], two decades ago, sparked an extensive range of ideas, proposals for applications and unexpected discoveries in the field of two dimensional materials. The motivation for the study of two-dimensional materials is twofold. The first aspect is the technological promise of extremely thin, flexible and transparent devices. The low dimensionality of these systems, combined with their high electron mobilities, strength and optical transmission make them exciting candidates for electronic niche applications where mechanical flexibility and transparency are important. One can specifically think about the market of wearable electronics. Examples of experimental devices include flexible and transparent field effect transistors [12–14], pressure sensors [15, 16] and photo detectors [17, 18].
Second, the past years have seen growing interest in the rich physics in van der Waals materials. The quality of van der Waals devices was boosted by the stacking of multiple layers, and specifically unsing hBN as a very flat and insulating substrate. Additionally there is a large variety of different materials availible with different properties. These different materials can also be combined and artificially stacked on top of each other. The simplicity of some of these atomic structures make these materials especially interesting for fundamental research. Here examples are two-dimensional magnetic systems [19], 2D charge density waves [20–22], and a superconducting state in twisted bilayer graphene [23, 24].
In order to cover different aspects of two-dimensional materials one needs a range of different techniques. The first natural candidates are electron transport techniques. The lab-based fabrication of exfoliated van der Waals devices has reached a high level. Multiple layers can be stacked on top of each other [25, 26], there is reasonable control over the twist angle [27, 28] and the electrical contact to these devices can typically be achieved using standard e-beam lithography techniques. Second, the two dimensional nature makes these materials very suitable for microscopy techniques. Because of the ultimate thinness the surface science catalogue of atomic force microscopy [29, 30] and scanning tunnelling microscopy [31, 32] is very suitable. Finally, the absence of a bulk enables transmission electron microscopy (TEM) as a popular technique to unravel structural features of these materials. [33, 34]
In this thesis, we will focus on two very different types of (effectively) two-dimensional materials. They differ in the size of their main unit. First, we will study van der Waals systems in which the unit size is that of an atom. We focus both

on chemically homogeneous (graphene, based on carbon, see figure 1.1 (b)) and heterogeneous materials (hexagonal BN, MoS_2). Second, we will investigate quasi-two-dimensional materials in which the basic units are quantum dots consisting of many atoms (see figure 1.1 (d)).
We will start this introduction with a discussion on two-dimensional electronic systems and we will cover some of the mentioned examples. Next, we will discuss some of the similarities and differences between these two systems. Finally the structure of this thesis will be outlined.

1.1.1. Two-dimensional materials

In two-dimensional electronic systems charge carriers are confined to move in a plane, in contrast to a volume as in bulk systems. The confinement of carriers to a plane can be realized in several different ways; examples include topological surface states [35, 36] and two-dimensional electron gasses that are formed between two insulating layers [37]. The focus here will be on materials in which electrons are confined to two dimensions due to spatial confinement. In this section we will discuss two examples of (quasi-) two-dimensional materials: van der Waals materials and monolayer nanocrystal superlattices.

Van der Waals materials

Van der Waals materials are a class of layered materials that share an absence of covalent bonds between layers. Within the crystalline layer the atoms are kept together by covalent atomic bonds, while the layers are kept together by van der Waals forces in the out-of-plane direction. This weak interaction in the perpendicular direction makes it possible to peel off layers, down to mono-layer thickness. The physical properties of Van der Waals materials will typically vary as a function of their layer count, down to one atomic layer. Systematic variations in conductance properties [38–40], optical properties [41] and mechanical properties [42] have been reported. Distinction can be found between single layers, several layers and bulk. Within the van der Waals materials there are two-dimensional insulators, semiconductors and a semi-metal.
Graphene is the best known member of the van der Waals materials, see figure 1.1 (b). Graphene consist of a single type of atom: carbon. The carbon atoms form a fully planar hexagonal lattice. Graphene is a semi-metal. In contrast, hexagonal boron nitride (hBN) is a wide-band gap insulator. This material has a very similar structure to graphene, but the unit cell consists of two distinct atoms: boron and nitrogen.
The next category is the family of transition metal dichalcogenites (TMDs). These materials share their composition: MX_2, where M is a transition metal and X the chalcogen. An example of a TMD is MoS_2. In contrast to hBN and graphene, the unit layer of TMDs consists of three atomic planes: in the middle we find the transition metal; this metal is sandwiched by two chalcogen layers. Additional to a

variation in combinations of transition metals and chalcogens, TMDs also show different crystal configurations. These different structures occur in some cases within the same material. This large variation in electronic structures also leads to a great variety in electronic properties. Among the TMDs we find semiconductors like MoS_2 and WSe_2, metals like 1T MoS_2, semi-metals like WTe_2 and superconductors like $NbSe_2$ and TaS_2.

Two-dimensional superlattices

The development of the field of two-dimensional materials also inspired the synthesis of larger, more complex - bottom-up - structures. These superstructures consist of building blocks that mimic the role of the atom, building up a larger crystalline structure. The idea is to obtain a high degree of control over the building blocks and structure created.

The system that will be of special interest is the PbSe nano-crystal supperlattice. The building blocks are single crystalline nano-crystals, with well-defined facets. [43] The shape of these crystals is schematically depicted in figure 1.2. The well-defined facets of the truncated cubes dictate the orientation of the inter-crystal attachment. This enables the synthesis of an atomically crystalline superstructure on a liquid-air interface.

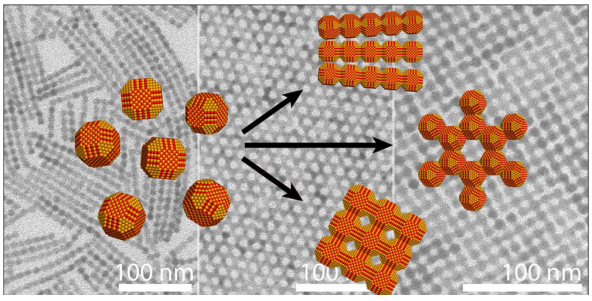

Figure 1.2: Orienented attachment of PbSe nanocrystals.The nanocrystal building blocks are depicted in orange at the left side of the figure. On the right side in orange, the different attachment shapes are shown. In the background the TEM images of such structures is shown. Figure taken from Ref [43].

The super-crystal symmetry can be tuned by precise synthesis parameters; by controlling temperature and nanocrystal density the preferred facets are tuned. Figure 1.2 depicts the different superlattice crystal structures that can be created. The left TEM image shows the linear lattice, the middle figure shows a honeycomb lattice and the right TEM image shows the square lattice. In these structures both the atomic composition of the NCs and the symmetry of the superlattice influence the electronic properties of the material. This degree of control allows the construction of lattices exhibiting exotic states of matter, by combining the hexagonal lattice - similar to graphene - with a large spin-orbit coupling in the case of nanocrystals containing heavy metals. In this thesis we will study the square PbSe lattice - as shown in figure 1.2.

We have discussed two different material categories that we will encounter in this thesis. They share a (quasi)-two-dimensional lattice structure. In the following part we will discuss some of the similarities and differences between them, which will also be leading for the different measurement techniques used.
The first notable difference, as mentioned is the size of the unit cells. The graphene unit cell is of the atomic size, while the superlattice building block is of the nanocrystal size, which is of the order of 5 nm (50 atoms in diameter). The building blocks are nanocrystals, which themselves have a 3D crystalline atomic structure: the PbSe lattice.
The second important difference is the synthesis of the two systems. Van der Waals materials are, in most cases, occurring naturally. Figure 1.3 shows an example of naturally occurring molybdenite (MoS_2, in gray) embedded in a quartz crystal (white). In bulk one could mine them and even in their monolayer form one could imagine them, by small chance, existing in nature. The natural occurrence of these materials enables a top-down approach to isolation of monolayers. This means that the naturally occurring symmetries can be maintained.
In contrast, the nanocrystal superlattices are a quite remarkable case of human engineering and control in material synthesis. First, the building blocks need to be made with very high precision. Second, the assembly of these systems requires high control over many parameters, like temperature and surrounding gasses. This bottom-up approach to material synthesis is highly complex and it is extremely hard to create the level of perfection some naturally occurring materials have. However, the level of control over both the building blocks and the final lattice gives great promise for material engineering. The main question for the bottom-up approach is whether disorder can be low enough.

1.2. Outline of this thesis

This thesis is divided in two parts. At the heart of the first part are low-energy electron microscopy (LEEM) experiments on two-dimensional van der Waals systems. The systems studied are graphene on a copper substrate (Chapter 3) and exfoliated hBN and MoS_2 (Chapter 4). The second part is centred around transport experiments. Here, we study the charge transport behavior of gated nanocrystal (NC) superlattices, both at room temperature and down to helium temperatures.
We will bring together different techniques and different angles to study (quasi-) two-dimensional materials. The outline of this thesis is summarized below.
The thesis will kick-off, in Chapter 2, with an introduction on the LEEM techniques used in chapters 3 and 4. In chapter 3 we use the LEEM-based scanning µLEED (*Low energy electron diffraction on the sub-micrometer scale*) technique to study the angular composition of state-of-the-art graphene grown on crystalline copper. We demonstrate that variations in crystalline orientations over large scales can be measured in an automated way. This enables an additional important quality study in these epitaxial layers. Chapter 4 deals with the unoccupied part of the band structure of two exfoliated van der Waals materials (hBN and MoS_2). We will present a

Figure 1.3: Natuaral MoS_2 (gray) in quartz crystal (white). [44]

very fast, high-**k**-resolution method to probe the unoccupied states.
In chapter 5 we will turn our attention to room-temperature electron transport in PbSe nanocrystal superlattices. These lattices are synthesized by self-assembly of nanocrystals on a liquid surface. We will incorporate these layers in four-probe micron-size, liquid gated devices. We will demonstrate ambi-polar transport in these devices and relatively high electron mobilities. Chapter 6 will take the devices from chapter 5 to low temperatures. The temperature dependence will give extended information on the mechanism of electron transport, and with that on the question on formation of bands in these materials.

1

References

[1] *Powerline* (2016 (accessed February 3, 2014)), https://commons.wikimedia.org/wiki/File:500kV_3-Phase_Transmission_Lines.png.

[2] *Graphene* (2010 (accessed February 3, 2014)), https://commons.wikimedia.org/wiki/File:Graphen.jpg.

[3] *Carbon nanotube* (2009 (accessed February 3, 2014)), https://commons.wikimedia.org/wiki/File:Carbon_nanotube_zigzag_povray_cropped.PNG.

[4] *Colloidal quantum dot* (2014 (accessed February 3, 2014)), https://commons.wikimedia.org/wiki/File:Colloidal_nanoparticle_of_lead_sulfide_(selenide)_with_complete_passivation.png.

[5] D. Bishop, D. Tsui, and R. Dynes, *Nonmetallic conduction in electron inversion layers at low temperatures,* Physical Review Letters **44**, 1153 (1980).

[6] R. Prange and R. Joynt, *Conduction in a strong field in two dimensions: The quantum hall effect,* Physical Review B **25**, 2943 (1982).

[7] M. Bockrath, D. H. Cobden, J. Lu, A. G. Rinzler, R. E. Smalley, L. Balents, and P. L. McEuen, *Luttinger-liquid behaviour in carbon nanotubes,* Nature **397**, 598 (1999).

[8] A. Aleshin, H. Lee, Y. Park, and K. Akagi, *One-dimensional transport in polymer nanofibers,* Physical review letters **93**, 196601 (2004).

[9] Y. Shirasaki, G. J. Supran, M. G. Bawendi, and V. Bulović, *Emergence of colloidal quantum-dot light-emitting technologies,* Nature photonics **7**, 13 (2013).

[10] H. Liu, T. Fujisawa, Y. Ono, H. Inokawa, A. Fujiwara, K. Takashina, and Y. Hirayama, *Pauli-spin-blockade transport through a silicon double quantum dot,* Physical Review B **77**, 073310 (2008).

[11] K. S. Novoselov, A. K. Geim, S. V. Morozov, D. Jiang, Y. Zhang, S. V. Dubonos, I. V. Grigorieva, and A. A. Firsov, *Electric field effect in atomically thin carbon films,* science **306**, 666 (2004).

[12] J. Yoon, W. Park, G.-Y. Bae, Y. Kim, H. S. Jang, Y. Hyun, S. K. Lim, Y. H. Kahng, W.-K. Hong, B. H. Lee, *et al.*, *Highly flexible and transparent multilayer mos2 transistors with graphene electrodes,* Small **9**, 3295 (2013).

[13] T. Georgiou, R. Jalil, B. D. Belle, L. Britnell, R. V. Gorbachev, S. V. Morozov, Y.-J. Kim, A. Gholinia, S. J. Haigh, O. Makarovsky, *et al.*, *Vertical field-effect transistor based on graphene–ws 2 heterostructures for flexible and transparent electronics,* Nature nanotechnology **8**, 100 (2013).

[14] D. Akinwande, N. Petrone, and J. Hone, *Two-dimensional flexible nanoelectronics,* Nature communications **5**, 5678 (2014).

[15] R. J. Dolleman, D. Davidovikj, S. J. Cartamil-Bueno, H. S. van der Zant, and P. G. Steeneken, *Graphene squeeze-film pressure sensors,* Nano letters **16**, 568 (2015).

[16] S.-E. Zhu, M. Krishna Ghatkesar, C. Zhang, and G. Janssen, *Graphene based piezoresistive pressure sensor,* Applied Physics Letters **102**, 161904 (2013).

[17] F. Xia, T. Mueller, Y.-m. Lin, A. Valdes-Garcia, and P. Avouris, *Ultrafast graphene photodetector,* Nature nanotechnology **4**, 839 (2009).

[18] R. B. Jacobs-Gedrim, M. Shanmugam, N. Jain, C. A. Durcan, M. T. Murphy, T. M. Murray, R. J. Matyi, R. L. Moore, and B. Yu, *Extraordinary photoresponse in two-dimensional in2se3 nanosheets,* ACS nano **8**, 514 (2013).

[19] C. Gong, L. Li, Z. Li, H. Ji, A. Stern, Y. Xia, T. Cao, W. Bao, C. Wang, Y. Wang, *et al.*, *Discovery of intrinsic ferromagnetism in two-dimensional van der waals crystals,* Nature **546**, 265 (2017).

[20] S. V. Borisenko, A. A. Kordyuk, A. N. Yaresko, V. B. Zabolotnyy, D. S. Inosov, R. Schuster, B. Büchner, R. Weber, R. Follath, L. Patthey, and H. Berger, *Pseudogap and charge density waves in two dimensions,* Phys. Rev. Lett. **100**, 196402 (2008).

[21] C.-S. Lian, C. Si, and W. Duan, *Unveiling charge-density wave, superconductivity, and their competitive nature in two-dimensional nbse2,* Nano letters **18**, 2924 (2018).

[22] Y. Yang, S. Fang, V. Fatemi, J. Ruhman, E. Navarro-Moratalla, K. Watanabe, T. Taniguchi, E. Kaxiras, and P. Jarillo-Herrero, *Enhanced superconductivity upon weakening of charge density wave transport in 2 h-tas 2 in the two-dimensional limit,* Physical Review B **98**, 035203 (2018).

[23] Y. Cao, V. Fatemi, S. Fang, K. Watanabe, T. Taniguchi, E. Kaxiras, and P. Jarillo-Herrero, *Unconventional superconductivity in magic-angle graphene superlattices,* Nature **556**, 43 (2018).

[24] Y. Cao, V. Fatemi, A. Demir, S. Fang, S. L. Tomarken, J. Y. Luo, J. D. Sanchez-Yamagishi, K. Watanabe, T. Taniguchi, E. Kaxiras, *et al.*, *Correlated insulator behaviour at half-filling in magic-angle graphene superlattices,* Nature **556**, 80 (2018).

[25] C. R. Dean, A. F. Young, I. Meric, C. Lee, L. Wang, S. Sorgenfrei, K. Watanabe, T. Taniguchi, P. Kim, K. L. Shepard, *et al.*, *Boron nitride substrates for high-quality graphene electronics,* Nature nanotechnology **5**, 722 (2010).

[26] A. K. Geim and I. V. Grigorieva, *Van der waals heterostructures,* Nature **499**, 419 (2013).

[27] P.-Y. Chen, X.-Q. Zhang, Y.-Y. Lai, E.-C. Lin, C.-A. Chen, S.-Y. Guan, J.-J. Chen, Z.-H. Yang, Y.-W. Tseng, S. Gwo, *et al.*, *Tunable moiré superlattice of artificially twisted monolayers,* Advanced Materials **31**, 1901077 (2019).

[28] K. Wang, B. Huang, M. Tian, F. Ceballos, M.-W. Lin, M. Mahjouri-Samani, A. Boulesbaa, A. A. Puretzky, C. M. Rouleau, M. Yoon, *et al.*, *Interlayer coupling in twisted wse2/ws2 bilayer heterostructures revealed by optical spectroscopy,* ACS nano **10**, 6612 (2016).

[29] C. H. Lui, L. Liu, K. F. Mak, G. W. Flynn, and T. F. Heinz, *Ultraflat graphene,* Nature **462**, 339 (2009).

[30] C. Martin-Olmos, H. I. Rasool, B. H. Weiller, and J. K. Gimzewski, *Graphene mems: Afm probe performance improvement,* ACS nano **7**, 4164 (2013).

[31] S. Hla, V. Marinković, A. Prodan, and I. Muševič, *Stm/afm investigations of β-mote2, α-mote2 and wte2,* Surface science **352**, 105 (1996).

[32] H. Coy Diaz, J. Avila, C. Chen, R. Addou, M. C. Asensio, and M. Batzill, *Direct observation of interlayer hybridization and dirac relativistic carriers in graphene/mos2 van der waals heterostructures,* Nano letters **15**, 1135 (2015).

[33] Z. Liu, K. Suenaga, P. J. Harris, and S. Iijima, *Open and closed edges of graphene layers,* Physical review letters **102**, 015501 (2009).

[34] P. Y. Huang, C. S. Ruiz-Vargas, A. M. Van Der Zande, W. S. Whitney, M. P. Levendorf, J. W. Kevek, S. Garg, J. S. Alden, C. J. Hustedt, Y. Zhu, *et al.*, *Grains and grain boundaries in single-layer graphene atomic patchwork quilts,* Nature **469**, 389 (2011).

[35] P. Roushan, J. Seo, C. V. Parker, Y. S. Hor, D. Hsieh, D. Qian, A. Richardella, M. Z. Hasan, R. J. Cava, and A. Yazdani, *Topological surface states protected from backscattering by chiral spin texture,* Nature **460**, 1106 (2009).

[36] Y. Xu, I. Miotkowski, C. Liu, J. Tian, H. Nam, N. Alidoust, J. Hu, C.-K. Shih, M. Z. Hasan, and Y. P. Chen, *Observation of topological surface state quantum hall effect in an intrinsic three-dimensional topological insulator,* Nature Physics **10**, 956 (2014).

[37] S. Thiel, G. Hammerl, A. Schmehl, C. W. Schneider, and J. Mannhart, *Tunable quasi-two-dimensional electron gases in oxide heterostructures,* Science **313**, 1942 (2006).

[38] E. S. Kadantsev and P. Hawrylak, *Electronic structure of a single mos2 monolayer,* Solid State Communications **152**, 909 (2012).

[39] W. Zhu, V. Perebeinos, M. Freitag, and P. Avouris, *Carrier scattering, mobilities, and electrostatic potential in monolayer, bilayer, and trilayer graphene,* Physical Review B **80**, 235402 (2009).

[40] W. Zhu, V. Perebeinos, D. Neumayer, M. Freitag, K. Jenkins, Y. Zhu, and P. Avouris, *Current transport, gate dielectrics and band gap engineering in graphene devices,* in *2010 10th IEEE International Conference on Solid-State and Integrated Circuit Technology* (IEEE, 2010) pp. 1214–1217.

[41] A. C. Ferrari, J. Meyer, V. Scardaci, C. Casiraghi, M. Lazzeri, F. Mauri, S. Piscanec, D. Jiang, K. Novoselov, S. Roth, *et al.*, *Raman spectrum of graphene and graphene layers,* Physical review letters **97**, 187401 (2006).

[42] A. Locatelli, K. R. Knox, D. Cvetko, T. O. Mentes, M. A. Nino, S. Wang, M. B. Yilmaz, P. Kim, R. M. Osgood Jr, and A. Morgante, *Corrugation in exfoliated graphene: an electron microscopy and diffraction study,* ACS nano **4**, 4879 (2010).

[43] M. P. Boneschanscher, W. H. Evers, J. J. Geuchies, T. Altantzis, B. Goris, F. T. Rabouw, S. Van Rossum, H. S. van der Zant, L. D. Siebbeles, G. Van Tendeloo, *et al.*, *Long-range orientation and atomic attachment of nanocrystals in 2d honeycomb superlattices,* Science **344**, 1377 (2014).

[44] (2010 (accessed 16.12.2019)), "https:/en.wikipedia.org/wiki/Molybdenite/media/File:Molybdenite_quebec2.jpg".

2

An introduction to Low Energy Electron Microscopy

2.1. Introduction

Low energy electron microscopy (LEEM) is a powerful surface probing technique, in which low energy electrons interact with a sample to form an image. In LEEM a sample is irradiated by an electron beam. The electron beam is first accelerated to 15 keV. Just before reaching the sample however the electrons are slowed down to energies in the range of 0-100 eV. After sample interaction the electron beam is deflected back into the imaging system. Finally, the image is projected onto a detector. Because of the low energies the technique is very surface sensitive. In the following section the basic operation and capabilities of the Leiden LEEM set-up (ESCHER) are explained.

Figure 2.1 shows a simplified illustration of the LEEM set-up. In this figure, the electron beam path is indicated in red, the lenses are indicated in blue, deflectors in black and apertures in green. Electrons are emitted at the top of the set-up, from the electron gun. They move through the system at an energy of 15 keV. The electron beam passes an array of electron-optical elements. The most relevant ones for the measurements done in this thesis will be explained in the following paragraphs, starting from the top.

Deflector 1 and deflector 3 are electron deflectors that steer the electron beam. The two deflectors are complementary in nature. Deflector 1 is placed in an image plane, this means that deflection of the beam translates to a change in incoming angle of the beam on the sample. In contrast, deflector 3 is placed in a back focal plane; a deflection in this plane translates to a change in location of the beam on the sample.

The square elements in figure 2.1 are referred to as ”prisms” (used as a circulator in optics). These prisms bend the electron beam to a 90° angle. This is done by applying a magnetic field, inducing a Lorentz force on the beam. In the first prism (prism 1 in figure 2.1) the electron beam is bent to a 90° angle towards the sample. Within this prism we find an illumination aperture. This aperture is situated in an image plane, which enables illumination of a specific section of the sample.

The lens closest to the sample is the objective lens. This lens is used, as the name suggests, to focus the image of the sample. Between the objective lens and the sample, the electrons are decelerated to an energy close to 0 eV. This deceleration is induced by an applied potential of -15 kV + V_0 relative to the gun potential. Hence, $V_0 \Delta\Phi$, where the latter is the work function difference between the gun filament and the sample, will be the landing energy of the electrons on the sample. The landing energy can be varied by the user, typically from -5 eV to +60 eV. This allows for LEEM spectroscopy, which we will discuss in section 2.4.

After reflection from the sample the beam, or image, returns to the objective lens. The beam is accelerated back to 15 keV by the voltage between the sample and the objective lens. The objective lens magnifies the image and the beam returns to the first prism. Now the electrons are deflected downward towards the second prism (prism 2 in figure 2.1). This prism steers the electron beam into the mirror arm of the system. This electron mirror corrects for the third order spherical and second rank chromatic aberrations induced by the uniform field between the sample and

the objective lens and by the objective lens itself. [1] and thus pushes the optimal resolution of the ESCHER set-up to 1.4 nm. [2] Below the second prism the electron beam is deflected into the projector column. The projector column allows for selection of the real-space image or a diffraction pattern. One of the lenses is used to focus the image plane onto the detector. An additional (optional) lens allows the diffraction pattern to be in focus on the detector. Additional lenses are used to change image and diffraction magnifications.
Within this projector we find the second aperture of the set up: the contrast aperture. This aperture is situated in a back focal plane of the system. This allows the selection of electrons scattered under a certain angle from the sample. As we will see in section 2.4 and in section 2.3.2, this aperture plays an important role in analyzing spectroscopic contrast and local crystalline structures of a sample.

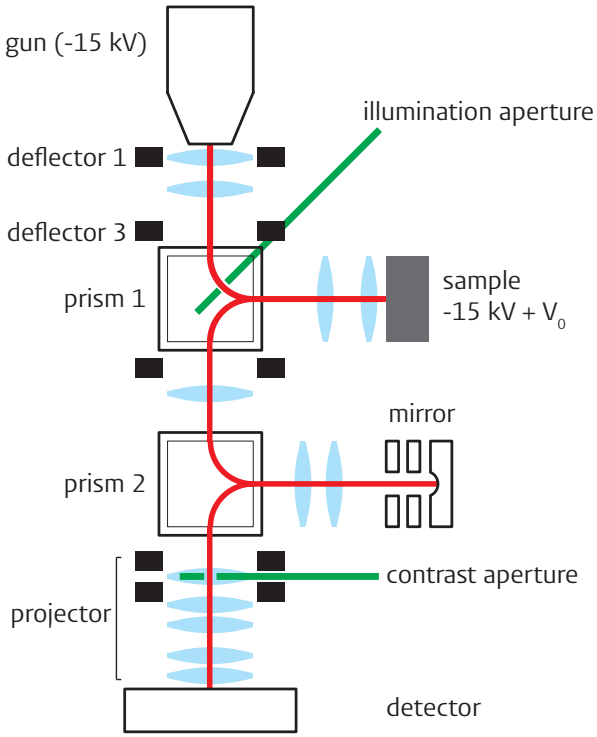

Figure 2.1: Schematic illustration of the LEEM set-up used in this thesis. The electron path is indicated in red, electron lenses in blue and the apertures in green. Adapted from [3]

.

In this chapter we will discus some of the various operation modes of LEEM. The

techniques discussed here are at the basis of chapter 3 and chapter 4. In section 2.2 we will cover photo emission electron microscopy, the technique used to measure the larger scale overviews in this thesis. Section 2.3 covers two LEEM imaging techniques (bright field imaging and dark field imaging), that we will use to translate diffraction information into real space. In this section the μLEED technique is also covered. In section 2.4 two modes of LEEM spectroscopy will be discussed.

2.2. Photo Emission Electron Microscopy

In Photo Emission Electron Microscopy (PEEM) the emission of the electrons is based on the photo-electric effect: the irradiation by photons promotes electrons in the material to higher lying bands. If the energy of the promoted electrons is larger than the work function of the material, the electrons are emitted from the surface. The amount of electrons available for photo-emission differs among materials and depends on the work function (Φ) and on the occupied states of the local band structure.
In the ESCHER set-up the image is formed by electrons emitted from the sample induced by irradiation of UV light from a Hg lamp. These electrons are then accelerated by the potential difference between the sample and objective lens. After ejection from the sample the electrons follow the same trajectory as in regular LEEM, see figure 2.1.
PEEM allows for a field of view significantly larger than the electron beam. Therefore we use the PEEM technique in this thesis mostly for overview images that characterize large-scale features of the samples studied. An example of such an overview is shown in figure 2.2.

2.3. Real-space imaging and reciprocal space information

A very powerful feature of LEEM is the capability to switch between real- and reciprocal space. Figure 2.3 shows a simplified ray representation of these two different planes. In figure 2.3 (a) the construction of a real space image plane is illustrated. Here the black arrow is the object (i.e., sample), the objective lens is indicated in gray and the image plane is indicated in yellow. The sample is irradiated by a collimated beam (not shown). Scattering at the surface of the sample induces the different angles at which the electrons leave the sample (indicated in green, blue and orange). In the image plane, the beams stemming from the same location on the sample are focussed, creating a (magnified) real-space image in the image plane (i.e., on the detector). Figure 2.3 (b) shows the construction of the reciprocal plane. In this plane the beams that leave the sample at the same angle (i.e., same colour in this figure) are now focused on the detector plane.
The flexibility of electron lenses allows us to focus on both the real-space plane and the diffraction plane. This is done by adapting one of the projector column lenses to

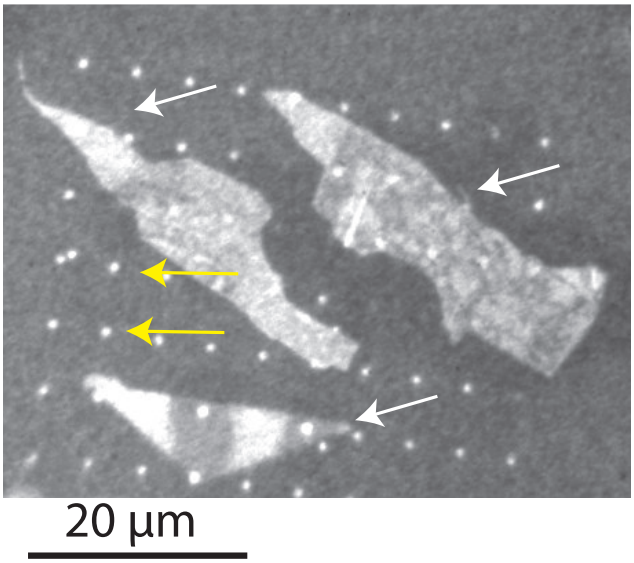

Figure 2.2: Example of a PEEM overview image of graphene flakes (white arrows), and small patterned gold circles (yellow arrows) on a silicon wafer (dark gray background).

focus on one or the other. The next sections will discuss the different applications of this capability.

2.3.1. Bright field imaging

Bright field (BF) imaging is the most common LEEM imaging technique. A BF image is composed of the specularly reflected electrons from the sample.
At the heart of BF imaging is the contrast aperture (indicated in green in figure 2.1). This aperture is located in a back focal plane and therefore gives the ability to select electrons emitted from a certain angle. For bright field imaging we select the specularly reflected electrons. This is illustrated in figure 2.4 (a), where the blue rays are the specularly reflected electrons; the aperture selects the part of the diffraction plane where they are focussed. The resulting BF image is a real-space image of the sample.
Figure 2.4 (b) shows a schematic representation of the diffraction pattern of a hexagonal surface lattice. This diffraction pattern can be recorded in the diffraction plane. The (0,0)-beam is the collection of specularly reflected electrons from the surface; it is indicated in blue. The gray overlay is the schematic representation of the contrast aperture. The aperture only transmits the electrons that form the (0,0)-beam.
Since in BF imaging, only the specularly reflected electrons are imaged on the detec-

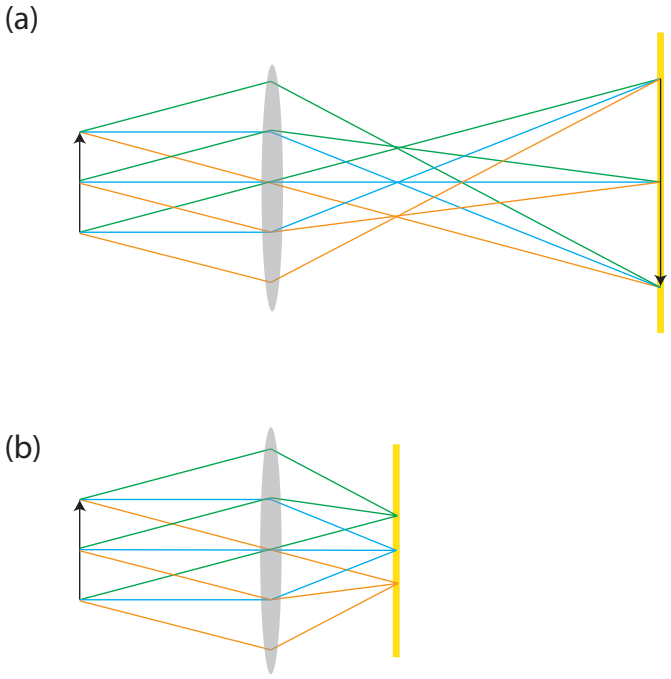

Figure 2.3: Illustration of the construction of the image plane (a) and diffraction plane (b). The object is indicated by the black arrow on the left, the objective lens is indicated in gray. Ray scattered at the same angle are indicated by the same colour.

tor, it has the advantage that it excludes the electrons that scatter inelasticly from the surface (often referred to as *secondary electrons*). The secondary electrons are emitted from the sample at all angles. These electrons generate significant intensity, especially at higher incident electron energies and blur the image. The energy dependence of these inelastic processes make the BF imaging mode indispensable when doing spectroscopy, as discussed in section 2.4

We distinguish two contrast mechanisms: first we have phase contrast (Fresnel contrast at step edges) and second amplitude or structure factor contrast (different materials, different layer thicknesses, quantum well contrast, etc.). Examples for the most important contrast mechanisms in this thesis are shown in figure 2.5. Panel (a) shows an example of a slightly sloped crystal (Au (111)). The slope (or, miscut in the crystal) of the material is accommodated by the formation of crystalline terraces. In BF LEEM the boundaries between the terraces are observed as darker lines running over the sample. Interference contrast is very sensitive to landing energy, as this changes the wave length of incoming electrons. Panel

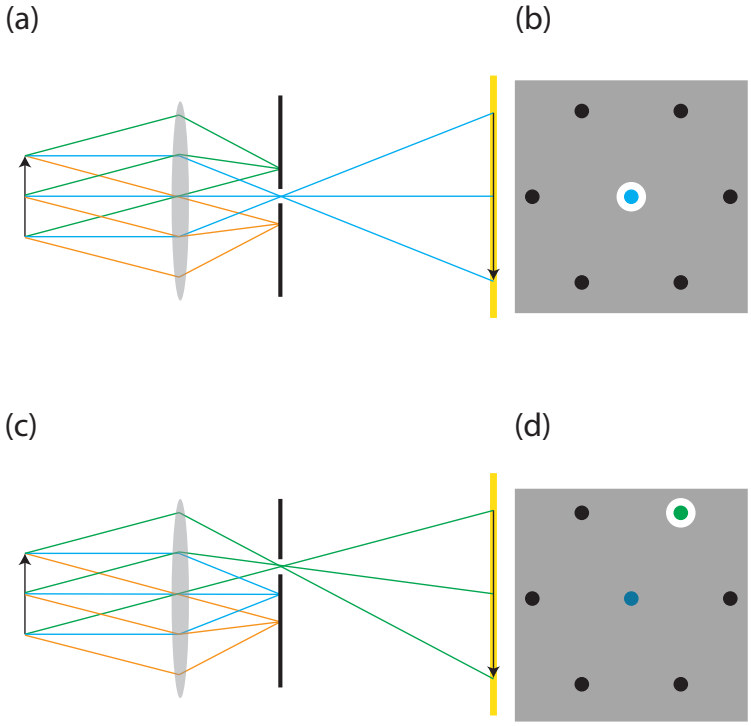

Figure 2.4: Illustration of bright field imaging (a, b) and dark field imaging (c, d). The object is indicated by the black arrow on the left; the image is projected on the yellow screen on the right, beams scattered at the same angle are indicated by the same colours. Note that this technique produces images in real space.

(b) shows an example of intensity contrast between different materials: the very dark regions are the gold (111) substrate, the gray areas are MoS_2 flakes. In the flakes additional contrast can be observed between mono-layer (blue dot), bi-layer (orange dot) and bulk (red dot). We will see more examples of this layer count contrast in section 2.4.

2.3.2. Dark field imaging

The next LEEM imaging technique we will discuss is dark field (DF) imaging. This is a powerful tool to image the spatial distribution of crystalline features.
The dark field technique is often used to study crystal growth processes that show several rotational directions. Examples can be found in the growth of gold on silicon [4], the growth of molecular thin films, like pentacene [5, 6], the surfaces of oxides [7] and the growth of graphene [8, 9].

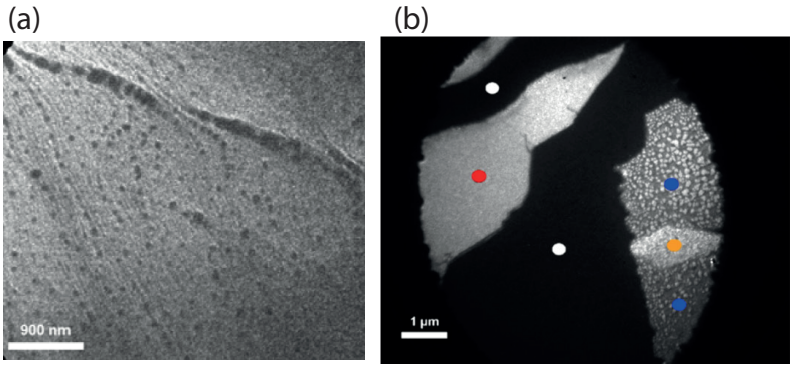

Figure 2.5: Examples of bright field images. (a) Sloped gold (111). Contrast is formed by interference of electrons at crystalline step edges on the surface. (b) MoS_2 flakes on gold (111), contrast is observed between MoS_2 flakes (gray) and gold (black, indicated by the white dots). Within the MoS_2 flakes additional contrast appears because of different layer counts (red dot: bulk, orange dot: bilayer, blue dot: monolayer).

Figure 2.4 (c) illustrates this technique. For DF imaging the same aperture in the back focal plane is used as for BF. However, instead of selecting the specularly reflected electrons, i.e. BF, we select the electrons reflected under a certain angle, typically we select a first-order diffracted beam. (in the example of figure 2.4 (c) the green angle). Figure 2.4 (d) shows an example of such an off-normal selection. Here, one of the first-order diffracted beams is selected. Hence, only the electrons diffracted at the part of the surface with the corresponding symmetry are selected. This results in a real-space DF image in the image plane, in which only the sample areas with the crystal symmetry corresponding to the selected diffraction spot light up.

Figure 2.6 (a) shows an example of the elegance of the dark field imaging method [7]. In this figure we see a dark field image of a $LaAlO_3$ (100) surface, that contains a mixture of the AlO_2 (dark) and the LaO (green and red) surface terminations. DF imaging can be used to distinguish the two surface terminations, in this case done by selecting one of the LaO diffraction spots. Moreover, two different rotational versions of the LaO reconstruction can be distinguished by selecting diffraction spots from these two rotations. The two rotations can be probed by changing the angle of the incoming electron beam with respect to the sample, while leaving the contrast aperture in place (typically, but not always, on the optical axis). In this figure two dark field images were combined in to the green and red colour coding. In contrast to changing the beam orientation, one can also change the location of the contrast aperture. The Leiden LEEM has access to a motorized contrast aperture drive in the diffraction plane. This gives the ability to scan the contrast aperture over multiple locations in the back focal plane. This technique, which will be referred to as scanning dark field is very useful when encountering multiple, similarly oriented crystal orientations. This gives multiple first-order diffracted beams within one field of view. By scanning the aperture and recording in real space one can get

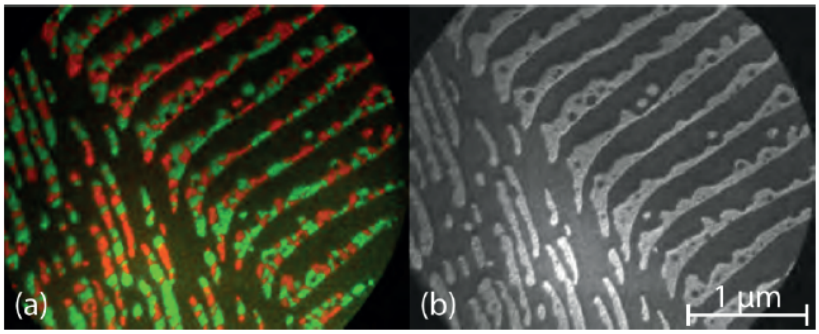

Figure 2.6: Color-coded composite DF (a) and BF (b) image of $LaAlO_3$. Panel (a) shows two superimposed DF images in which the two surface rotations are indicated in green and red. Figure taken from [7]

a stack of real-space images of different crystal orientations, by combining these images in a composite image the spatial extent of different crystal orientations can be visualized.

2.3.3. µLEED

Next we will discuss the use of the other aperture in the system: the illumination aperture, situated in the upper magnetic prism (green in figure 2.1). This aperture is located in an image plane, before the sample, of the system. The location enables spatial restriction of the illuminating beam on the sample.
By restricting the spatial size of the illuminating beam, one can study smaller areas of the sample in reciprocal space. The illumination apertures in the Leiden set-up range from 200 nm to 3 µm (this is the size, after demagnification by about 27x on the sample).
The µLEED technique is used to measure local variations of surface structure or Moiré lattices for example in van der Waals hetero structures [10] and graphene orientations [11, 12]. In Chapter 3 we extend µLEED techniques to unravel the large-scale variations in mono-layer graphene on copper, by scanning spatially over a sample by moving the sample stage over a grid.

2.4. Spectroscopy techniques

Variation of the landing energy at the sample gives spectroscopic information on electronic states at surfaces. This is observed in the experiment as a variation in the electron reflectivity (R) of a surface as a function of the landing energy (E). The R(E) curve is material specific and for several van der Waals materials also layer count specific [13]. LEEM operates above the vacuum energy of the surface (where

we define E = 0) and goes up to energies of about 100 eV.
In the next sections we will first discuss the cases of normal incidence of the incoming beam, which builds the R(E) curve at a surface; finally we will also discuss the case of off-normal incidence, which will give a R(E, $\mathbf{k}_{\parallel}$) diagram.

2.4.1. Normal incidence

Reflectivity variation as a function of the landing energy can be recorded both in real-space and in reciprocal-space. Both these techniques have advantages which we will discuss next.
First, we will discuss spectroscopic measurements in which the landing energy is varied and the real-space BF images are recorded. Real-space imaging has the important advantage of resolution. The R(E) curves can be recorded at pixel accuracy, by using sophisticated data analysis techniques. [14] This means that small-scale R(E) variations in materials can be measured.
The second technique is the recording of k-space images while varying the landing energy. In this case the spatial resolution is limited by the illumination aperture size (see *μLEED* in section 2.3.3). The advantage is that in addition to the spectroscopic information in the spectral spot (in BF imaging), the full diffraction pattern is available for analysis.
Figure 2.7 [15] shows an example of a BF reflectance versus energy curve. Panel (a) shows a BF image of graphene on SiC. At this energy, contrast is visible between different areas. Panel (b) shows the energy dependence of the reflectance of the indicated locations. The energy dependence shows a different number of intensity dips between 0 and 5 eV. The number of minima in these curves can be related to different graphene layer counts. For each graphene layer (excluding the buffer layer on SiC) an additional minimum appears in the spectrum. [13]

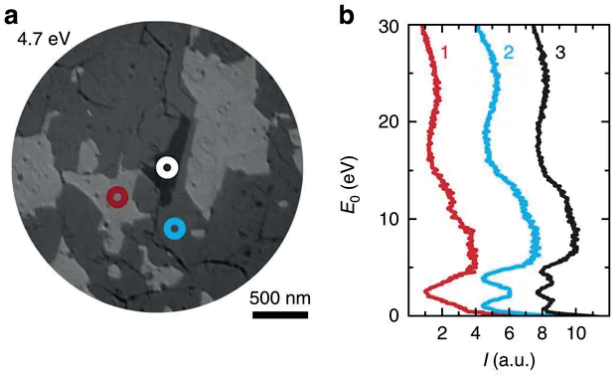

Figure 2.7: (a) BF LEEM image of graphene on SiC at a landing energy of E = 4.7 eV. Three different coloured areas are present. (b) Reflectance versus energy curves measured at the locations indicated in panel (a). The number of dips in these curves correspond to 1 (red), two (blue) and three (black) graphene layers (the curves are off-set for clarity). Figure taken from [15]

2.4.2. Off-normal incidence: ARRES

In normal BF LEEM operation, the system is aligned such that the incoming electron beam comes in perpendicular to the sample. This means that the full momentum of the electron is in the perpendicular component ($\mathbf{k}_\perp = \mathbf{k}_{\text{tot}}$) and the parallel component of the momentum is zero ($\mathbf{k}_\parallel = 0$).
In contrast, in off-normal incidence we introduce a parallel component to the momentum of the incoming electrons. This is done by tilting the incoming electron beam with respect to the sample's surface. The Leiden set-up enables this by varying the current in the deflector used for defining the beam tilt (deflector 1 in figure 2.1).
In the tilted electron beam the parallel component of the momentum of the electrons is non-zero: $\mathbf{k}_\parallel \neq 0$, and it can be varied during a measurement. The reflectance at the non-zero parallel momentum values is, amongst others, a function of the availability of unoccupied electronic states at the surface at those specific E and $\mathbf{k}_\parallel$.
The measurement technique in which both the energy and the parallel momentum are varied is called angle-resolved reflected-electron spectroscopy (ARRES). Figure 2.8 [15] shows examples of an ARRES measurement on the same graphene on SiC sample as cited in figure 2.7. Here, the vertical line at the Γ-point is equivalent to the spectra presented in figure 2.7 (a). Again, a different number of minima are present for the different layer counts, but now these extend over the different $\mathbf{k}_\parallel$ values and hence we can follow their dispersion. Between 0 and 15 eV there is a large high reflectance region (red), pointing to the absence of electronic states in this region.
As we will see in chapter 4 this technique enables measurement of unoccupied

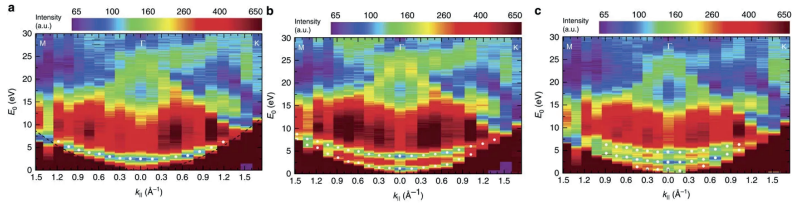

Figure 2.8: ARRES maps of graphene on SiC. (a) Monolayer, (b) bilayer and (c) trilayer are distingwished by the number of minima between 0 and 5 eV, most easily seen around the Γ-point. Figure taken from [15]

states and resolves the band diagram at the materials surface. this technique is complementary to existing band probing methods, as discussed in Chapter 4.

2

References

[1] R. M. Tromp, W. Wan, and S. M. Schramm, *Ultramicroscopy Aberrations of the cathode objective lens up to fifth order,* Ultramicroscopy **119**, 33 (2012).

[2] S. M. Schramm, *Imaging with Aberration-Corrected Low Energy Electron Microscopy* (2013).

[3] R. M. Tromp, J. B. Hannon, A. W. Ellis, W. Wan, A. Berghaus, and O. Schaff, *A new aberration-corrected, energy-filtered LEEM/PEEM instrument. I. Principles and design,* Ultramicroscopy **110**, 852 (2010).

[4] J. Kautz, M. W. Copel, and S. J. v. d. M. M. S. Gordon, R. M. Tromp, *Titration of submonolayer Au growth on Si (111),* **035416**, 1 (2014).

[5] A. Al-Mahboob, J. T. Sadowski, T. Nishihara, Y. Fujikawa, Q. K. Xue, K. Nakajima, and T. Sakurai, *Epitaxial structures of self-organized , standing-up pentacene thin films studied by LEEM and STM,* **601**, 1304 (2007).

[6] K. P. Weidkamp, R. M. Tromp, and R. J. Hamers, *Epitaxial Growth of Large Pentacene Crystals on Si (001) Surfaces Functionalized with Molecular Monolayers,* , 16489 (2007).

[7] A. J. H. V. D. Torren, S. J. V. D. Molen, and J. Aarts, *Formation of a mixed ordered termination on the surface of LaAlO 3 (001),* **245426**, 1 (2015).

[8] D. A. Siegel, S. Y. Zhou, F. E. Gabaly, A. K. Schmid, K. F. Mccarty, and A. Lanzara, *Three-fold diffraction symmetry in epitaxial graphene and the SiC substrate,* , 1 (2009).

[9] S. Grandthyll, S. Gsell, and E. Mete, *Extraordinary epitaxial alignment of graphene islands on Au(111),* (2012), 10.1088/1367-2630/14/5/053008.

[10] M. Petrovi, M. H.-v. Hoegen, and F.-j. Meyer, *Applied Surface Science Lateral heterostructures of hexagonal boron nitride and graphene : BCN alloy formation and microstructuring mechanism,* **455**, 1086 (2018).

[11] P. S. Arjun Dahal, Rafik Addou and M. Batzill, *Graphene monolayer rotation on Ni (111) facilitates bilayer graphene growth,* Applied Physics Letters **241602** (2014).

[12] K. L. W. Lau, K. M. Yu, D. Luo, R. S. Ruoff, and M. S. Altman, *Ultramicroscopy High throughput scanning μLEED imaging of surface structural heterogeneity : Defective graphene on Cu (111),* **200**, 67 (2019).

[13] H. Hibino, H. Kageshima, F. Maeda, M. Nagase, Y. Kobayashi, and H. Yamaguchi, *Microscopic thickness determination of thin graphite films formed on SiC from quantized oscillation in reflectivity of low-energy electrons* β β α, , 1 (2008).

[14] T. A. D. Jong, D. N. L. Kok, A. J. H. V. D. Torren, H. Schopmans, R. M. Tromp, S. J. V. D. Molen, and J. Jobst, *Quantitative analysis of spectroscopic Low Energy Electron Microscopy data: High-dynamic range imaging, drift correction and cluster analysis,* Ultramicroscopy , 112913 (2019).

[15] J. Jobst, J. Kautz, D. Geelen, R. M. Tromp, and S. J. Van Der Molen, *Nanoscale measurements of unoccupied band dispersion in few-layer graphene,* Nature Communications **6**, 1 (2015).

3

Scanning μLEED

3.1. Introduction: Graphene production

Starting with the first isolation of a single layer of graphene [1] both fundamental science and industry have shown significant interest in the use of this material. In fundamental science, graphene research has grown into a mature field over the last decade. However, industrial applications require a suitable, high-quality manufacturing method to access the exceptional properties of the two-dimensional carbon lattice. The growth of wafer-scale single-crystalline graphene has proven to be challenging and is currently one of the main bottlenecks hindering industrial applications of graphene.

In this introduction we will start by sketching an overview of the different ways to manufacture graphene. This starts with the first, remarkably simple, technique of scotch tape exfoliation, next we will discuss the growth of graphene on silicon carbide and we will finish the introduction with the growth technique used to produce the samples measured in this chapter.

Historically, the first isolation of monolayer graphene was performed by scotch-tape exfoliation. This technique has been developed and perfected ever since [2–4] and is still the gold standard for academic research [5, 6]

The basics of this exfoliation process are surprisingly simple. Using sticky tape a variaty of layers of graphite and graphene are peeled off a graphite crystal. The collection of graphene and graphite flakes stemming from the crystal are transferred from the tape to a silicon oxide substrate. This substrate enables layer-count contrast and is suitable for the selection of mono layer flakes. [7] After flake selection the graphene is ready for device fabrication steps.

Although the quality of tape-exfoliated graphene is currently still superior to any other technique, industrially this technique is not too appealing. The process is slow and labor intensive, the yield is low and the areas of monolayer pieces of graphene are small and irregular in shape. For these reasons, tape exfoliation is not seen as a competitive candidate for serious industrial manufacturing. For this a wafer-scale method in needed.

Typical wafer scale graphene production methods rely on the epitaxial growth of a graphene lattice on top of a substrate with a comparable surface structure. Epitaxial growth is a procedure that is used in thin film growth for decades and is therefore quite mature.

The first system for epitaxial growth of graphene we will discuss is graphene on silicon carbide (SiC). [8] The process starts with a silicon carbide wafer. The top layer silicon is sublimated at high temperatures, preferably in a argon or silane gas environment. [9] This leaves a carbon-based layer at the interface. The carbon layer closest to the SiC bulk bonds to the underlying SiC, but the second layer is only van-der-Waals-bonded to the substrate and forms the hexagonal graphene lattice. The main advantages of this growth method include the simplicity and scalability. However, the reported electron mobilities of graphene grown on SiC lag far behind exfoliated graphene. [10]

Next, we discuss chemical vapour deposition (CVD) techniques on metal surfaces. CVD is a technique in which a metal surface is exposed to a volatile gas (in the case

of graphene containing carbon atoms, like methane), this gas decomposes on the surface, the residual carbon forming the desired thin film.
For the CVD method a variety of different metals can be used. Typical substrates selected are closed packed face-centered (FCC) metals at the (111) surface. This surface has a hexagonal structure that allows semi-epitaxial growth of graphene, depending on the unit cell size. The crystalline quality of the substrate is important for the formation of single crystalline graphene. On top of a desired unit cell size, close to that of graphene, also the solubility of carbon in to the metal is an important parameter. [11]
In this work we will focus on graphene on crystalline copper. The unit cell size of the copper (111)-surface is very similar to that of graphene. Additionally, the solubility of carbon in copper is very poor, which prevents the formation of additional graphene or amorphous carbon layers in the cooling step after growth. [12]
The CVD growth of graphene on copper can yield a variety of different island shapes, which indicate different growth processes. [13] These growth processes determine the crystalline quality, grain size and angular orientation of the graphene film.
The most standard quality check on graphene is Raman spectroscopy. This is an optical spectroscopy technique, where the inelastic photon scattering is probed. The inelastic processes include the interaction of the photon with the vibrational modes of the material. These vibrational modes give direct information on, amongst others, the graphene uniformity [14], the layer count [15, 16], stacking symmetry[17, 18] and the presence of charge impurities [19]. Common Raman spectroscopy typically gives information on a larger scale (>100 μ m), and it does not give a measure of the rotational alignment of the crystal.
In this chapter we will develop a technique that utilizes LEEM-based measurements to analyze large-scale graphene layers for its angular spread. We study commercially CVD grown graphene on copper wafers supplied by *Applied Nanolayers BV*.

3.2. Scanning μLEED

3.2.1. LEED and rotational domains

Rotations of the graphene lattice manifest themselves in the rotation of the first order spots in the diffraction pattern as illustrated in figure 3.1 (a). The left panel shows a schematic side cut of a free standing graphene sheet. The two colours indicate two different rotations present. The blue represents an area at a zero degree rotation (compared to some arbitrary reference, for now). The green part is 30 degrees rotated in the in-plane direction. The right panel shows the schematic representation of the diffraction patterns of the two areas. The (0,0) beam is indicated in black, the blue and green dots illustrate the two sets of first order diffracted beams, stemming from the two rotational domains, indicated by the same colour.
The next step is to include the Cu(111) substrate in our considerations. As we will see the presence of a second lattice will give rise to an additional measure of the graphene rotation. Figure 3.1 (b) illustrates this situation. In the left panel the schematic side cut is shown. Below the two graphene rotational domains (blue and

green) a single crystalline copper (111) layer is illustrated in orange. The graphene now has a defined rotation with respect to the copper below. For this example we take the blue part to be aligned with the copper and the green part to have a 30 degree rotation.
The unit cell of the copper (111) lattice is slightly larger (2.56 Å) than the graphene unit cell (2.46 Å). This mismatch translates in the diffraction pattern to copper spots situated inward compared to the graphene spots. This is illustrated in the right panels in figure 3.1 (b), where the copper diffraction pattern is visualized by orange spots.
The mismatch between the two unit cell sizes creates a Moiré pattern. This Moiré pattern stems from the super cell created by the two mismatching lattices. In the diffraction pattern this is seen as a collection of satellite spots around the (0,0) beam and around the first order spots of the graphene. This is illustrated in the right panel of figure 3.1 (a) as red spots. The figure 3.1 (b) shows the same construction as above, but now for the 30 degree rotated graphene lattice. The radius of the Moiré pattern is directly related to the offset angle between the two lattices and the lattice size mismatch, as:

$$\theta = \arccos\left(\frac{r_{\mathrm{G}}^2 + r_{\mathrm{Cu}}^2 - r_{\mathrm{M}}^2}{2 r_{\mathrm{G}} r_{\mathrm{Cu}}}\right), \tag{3.1}$$

where θ is the angle between the copper lattice and the orientation of the graphene, r_{G} is the distance between the central spot and the first order graphene spot, r_{Cu} the distance between the central spot and the first order copper spot and r_{M} is the radius of the Moiré pattern measured from the centre spot.
The Moiré super cell, in real space, is largest when the two mismatching lattices align rotationally, and smallest when there is a 30 degree offset. By measurement of the Moiré spots radius from, for example, the central spot, we can directly calculate the rotational orientation of the graphene with respect to the copper lattice. From figure 3.1 we can conclude that we have access to two different ways to measure the rotational orientation of the graphene lattice: first the direct measurement of the location of the first order diffracted beams, secondly the measurement of the radius of the Moiré pattern formed by the combination of the graphene lattice and the copper lattice underneath.

3.2.2. Scanning μLEED technique

In this chapter we want to investigate graphene orientations over tens of microns, to get a complete overview of the crystalline grains of the material. The Escher set-up in Leiden has an electron beam size of approximately 10 μm, which can be expanded to 20 μm by adjusting the illumination optics. This size is of significance for this work because of two main reasons. First it limits the field of view (FoV) for a single image to that size, whereas here we would need a much larger field of view. Second it limits the resolution of diffraction measurements, because diffraction information from the full beam size will be mixed up in the back focal plane.

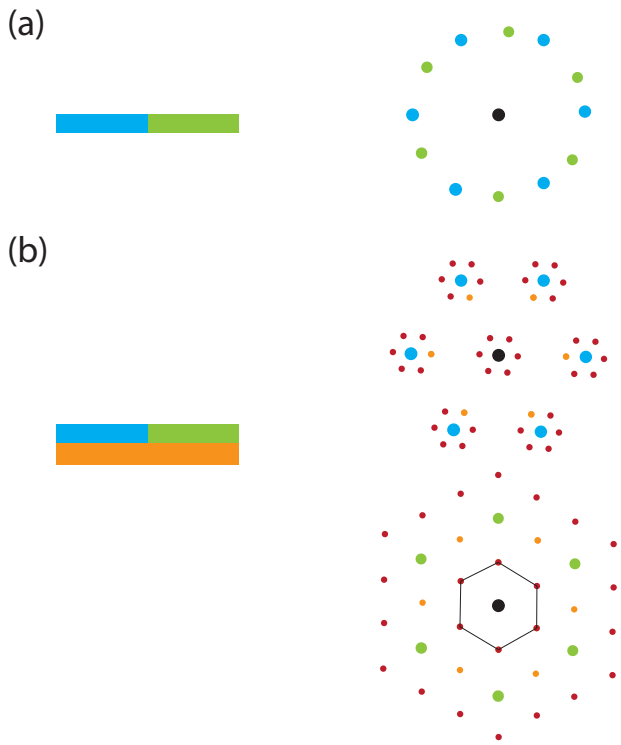

Figure 3.1: Schematic illustration of rotational domains in graphene and the translation to diffraction. (a) Left panel: free standing graphene in a zero degree rotation (blue) and 30 degree rotation (green). Right panel: The diffraction pattern of the combination of the two rotated lattices. Colours indicate the two regions. (b) Left panel: Two rotations of graphene (again, in blue and green), orange denotes a Cu(111) lattice underneath. Copper is chosen in the same orientation as the blue part of the graphene layer. Right panel: Two diffraction patterns from the blue (upper) and green (lower) graphene layer. In orange the copper (111) spots are added to the patterns, with a slightly smaller periodicity. In red the Moiré pattern is indicated.

Paradoxically, we need a larger FoV than the beam size can accommodate, and we need diffraction patterns from smaller area's than the full beam accommodates. The following section clarifies solutions chosen to enable this.
Figure 3.2 (a) shows the LEEM setup. Two parts are of special importance for the scanning µLEED techniques and these are highlighted in the figure. The first is the illumination aperture, that is situated in the higher half of the first magnetic prism (MPA1). The second part with special importance is the sample stage.
The illumination aperture in MPA1 is used to increase the spatial resolution of LEED measurements. The aperture is inserted in the image plane of the incoming beam, as schematically illustrated in figure 3.2 (b). This means that the size of the illuminating beam is restricted by the size of the aperture - as illustrated in the lower

panel of (b). This restriction enables the measurement of diffraction patterns of smaller area sizes than the beam size. This increases the spatial resolution of the scanning μLEED technique significantly.
The Leiden Escher set-up is equipped with an array of illumination apertures, ranging in diameters (on the sample) from 200 nm to 3 μm. In this chapter we consistently use the 500 nm aperture, as seen in figure 4.5 (c). This aperture is the smallest aperture that gives a high enough signal-to-noise ratio in the back focal plane to allow sufficient analysis of diffraction patterns, within reasonable measurement time.

The second part of the set-up that needs special attention for the experiments performed in this chapter is the sample stage. The location of this part is highlighted in figure 4.5 (a). The sample stage can be moved in the (x,y) plane and in all z tilt directions. For this movement it uses eight piezo motors, four for (x,y) movement and four for tilt and z movement. The z direction and tilt motors are of high importance for proper alignment of the instrument. The (x,y) movement is of prime importance for the scanning measurements and will be discussed in the following paragraph.
Figure 3.2 (d) shows a schematic illustration of the sample stage. The stage is equipped with four slip-stick piezo motors that allow (x,y) movement over multiple millimetres. Additionally the set-up allows manoeuvring of the sample stage to a 100 nm accuracy. [20]

3.3. Sample characterization

3.3.1. Optical characterization

Figure 3.3 introduces the two types of samples studied in this chapter. The upper panels show optical pictures, the lower panels illustrate the cross sectional cuts of the two samples. The samples consist of a sapphire wafer, and a thin crystalline copper film in the (111) orientation, topped by graphene. Both samples were taken from the middle of a 4" wafer. The difference between the samples is the stage at which the graphene growth was terminated. For the first sample (figure 3.3 (a)) the growth was terminated before completion of the first monolayer graphene. To enhance optical contrast, the copper was oxidized after the growth process, enabling optical characterization. In the second sample (figure 3.3 (b)) graphene growth was continued till it fully covered the sample.
These two different wafers give us the opportunity to analyse angular variations of the graphene present in two stages of the growth process.

3.3.2. PEEM

Figure 3.4 shows PEEM images of the partially grown (a) and the fully grown (b) graphene layer. Contrary to the samples used for the optical inspection, oxidation

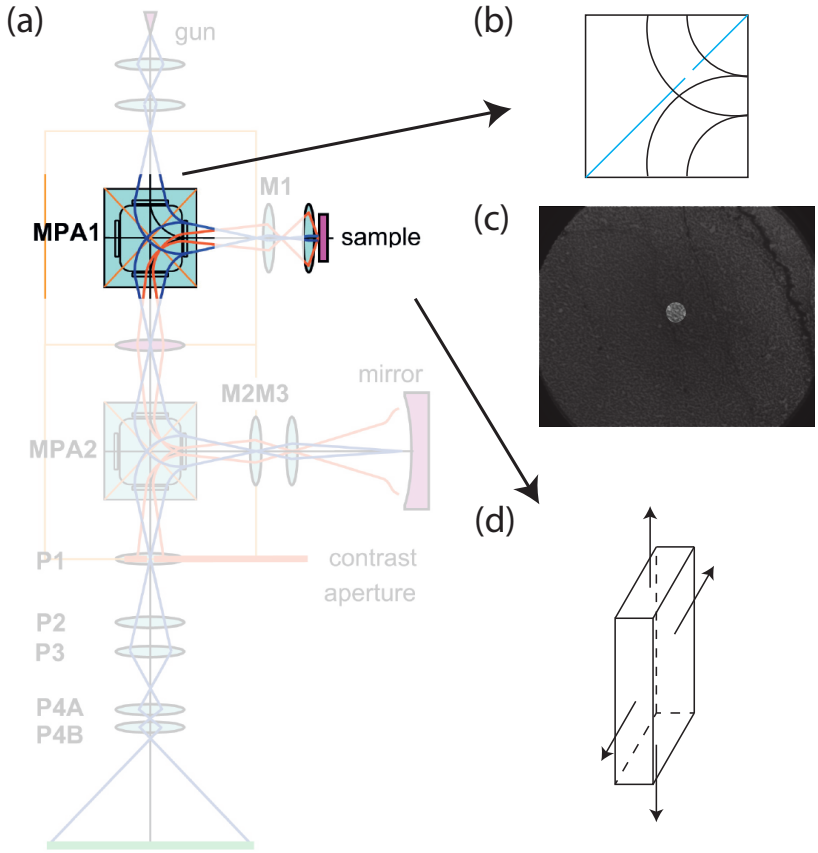

Figure 3.2: Schematic illustration of the LEEM and highlighted parts. (a) Schematic of the LEEM (adapted from [21]) with the upper magnetic prism (MPA1) and the sample location highlighted (b) Location of the illumination aperture in the image plane of the upper prism. The beam only passes this aperture in the incoming direction. (c) Illustration of the real-space image with this aperture in place. Only the highlighted area is illuminated. (d) Schematic illustration of the stage movement in the (x,y) direction.

was kept to a minimum in the samples used in PEEM and LEEM measurements. The shapes of the graphene islands (dark) on the partially grown structures are very similar to those in the optical pictures. The islands consist of main branches, typically spanning over tens of micrometers. The main branches intersect preferably, but not exclusively, in a four-fold symmetry. In most cases these branches are straight, but in some cases they show bending. From the main branches secondary branches form. These smaller branches have a preferred orientation of 90° or 60° relative to their main branch. These secondary branches grow with a 90° angle to the primary branch in most cases.
The irregular shape that we observe in these islands is not uncommon. The forma-

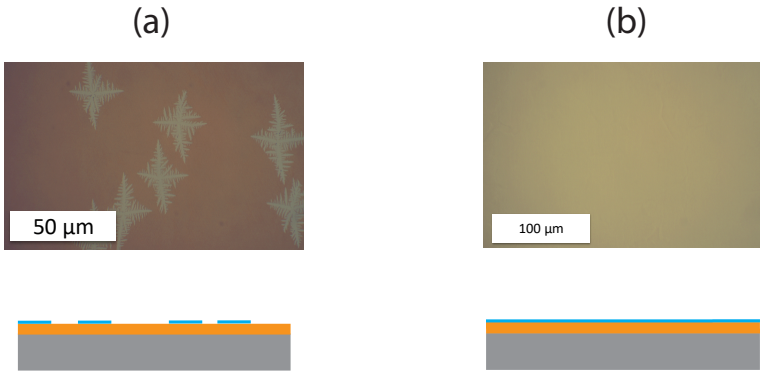

Figure 3.3: Optical image (above) and schematic cuts (below) of the partially grown (a) and fully grown (b) wafers. In the schematic the grey color depicts sapphire, the orange the thin copper layer, and the blue the graphene.

tion of such *dendric* structures has been observed in, amongst others, molecular thin films [22] and graphene on metal surfaces. [13, 23, 24] This typical shape can be related to diffusion-limited growth; a growth mechanism in which the atomic, or molecular building blocks are mobile on the surface, until they hit the edge of an island and attach firmly with neglectable further diffusion. [25]
The PEEM image of the fully grown layer (figure 3.4 (b)) looks a lot less uniform than in optical pictures (figure 3.3 (b)). Bright areas of the order of 10 μm alternate with smaller dark patches. The nature of the dark patches is unclear. A possible explanation is that they are due to unintentional oxidation of the underlying copper crystal. Two indications for this hypothesis are that, first, the darker patches follow lines on the substrate and, second, they have a clustered, diffusion-like structure. This is consistent with a picture of oxygen diffusing into the copper-graphene interface through crystal imperfections, thus forming a copper oxide interface around copper step edges.

The partially grown wafer (figure 3.3) (a) and figure 3.4 (a)) shows two indications of single crystalline growth of the graphene, over sizes up to an island size. First, the observation of relatively large islands during the growth process, of the order of 50 μm, suggests formation of a crystalline structure. Second, the islands show preferred grow directions, which are also maintained on the scale of multiple islands. This suggests preferred growing directions dictated by the underlying copper. However, the deviations from this preferred growth direction and the bending of the branches indicate that the growth is not exclusively determined by the atomic structure of the underlying copper lattice. This could lead to a possible angular spread in the graphene, which will be studied next.
The coming sections will be dedicated to a detailed study of the angular spread in the graphene. We will use two dedicated LEEM techniques to investigate the small and larger scale angular orientation of the graphene with respect to the underlying

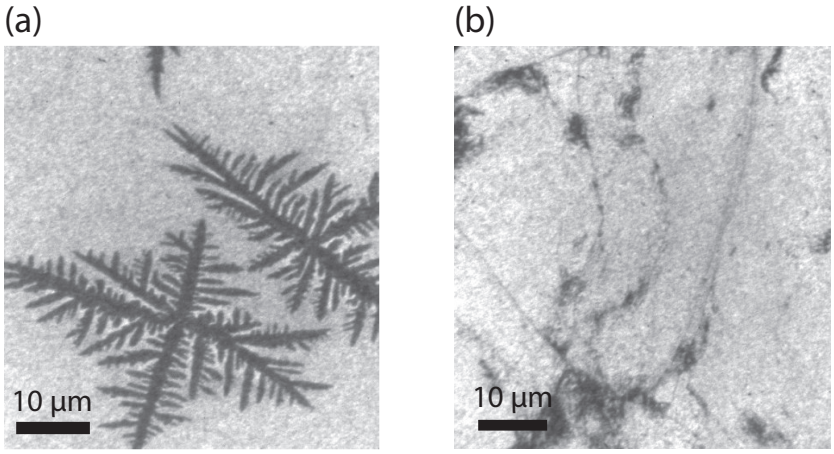

Figure 3.4: PEEM images of (a) partially grown graphene islands (dark) on copper (light) and (b) a fully grown graphene layer.

copper lattice of the (fully grown) graphene lattice. First we will direct our attention to the question on what the angular spread in a single dendritic island is like. Next the propagation of the island shape into to the fully grown monolayer is studied. And finally we will study the large scale angular spread of the graphene monolayer.

3.3.3. LEEM, LEED and spectroscopy of an island

To study the orientation of the graphene within a single island, we first turn our attention to the partially grown sample. In this sample, the outlines of the original growth islands are still very well determined and observable.
Figure 3.5 shows analysis of such an island, using PEEM (a), bright field LEEM (b), LEED pattern (c,d) and reflectance spectra (e) from LEEM bright field images. As seen in the PEEM overview in figure 3.5 (a) the island selected for this figure has two main intersections. At the middle right, two branches intersect at an angle of approximately 90°. At the left side of the image we observe a threefold symmetric intersection with a severely bent branch moving up. The different features of this island allow a study of the correlation between the island shape and the local angular composition of the graphene lattice.
Figure 3.5 (b) shows a stitched bright field LEEM image recorded at a landing energy of E = 1.2 eV. The image exhibits inverted contrast compared to the PEEM images. Additional features are visible within the light gray graphene island compared to the optical and PEEM images. The lines running through the centre of the main branches are the most prominent of these.
Figure 3.5 (c) and (d) show tilted LEED patterns of locations indicated by the black circles in figure 3.5 (b). The central spot is indicated by the (0,0) marking in the

right side of the pattern. On the left side we observe two first order spots for both locations, indicating that in both areas two graphene orientations are present.
Another interesting observation in the diffraction patterns is the absence of copper spots and following from that the absence of a Moiré pattern. The visibility of these spots would be expected in case of a single layer of graphene, especially on patches where the copper is not covered by graphene at all. The absence can be explained by oxidation of the copper, happening during handling and transfers. This oxidation is likely to take place at the bare copper areas, and also by oxygen diffusion from the sides of the graphene islands to the entire area underneath.

Figure 3.5 (e) shows the intensity spectra derived from a copper area (orange) and a graphene area (green). Exact areas are indicated by the dots in figure 3.5 (b). The spectrum of the graphene in this sample is characteristic for graphene, moreover absence of additional minima in the energy range between 0 and 10 eV confirms that there is uniformity in the layer-count. The intensity spectrum could be related to either bi-layer graphene, or monolayer graphene with an additional buffer layer [26]. The copper(oxide) lacks clear spectroscopic features and is darker than the graphene over the entire energy range.
From these first characterizations we can conclude the following. First, the island consist of mono layer graphene, as seen from the spectroscopic data in panel (e) and the absence of large-scale bright field contrast over the full energy range (b). Second, the crystallinity of the copper is not observable in these measurements. Finally, the island is not single crystalline, as observed by angular variation in the tilted diffraction patterns (c,d).
The next step is to investigate the spatial structure of the graphene orientations present within an island. The next section will cover this.

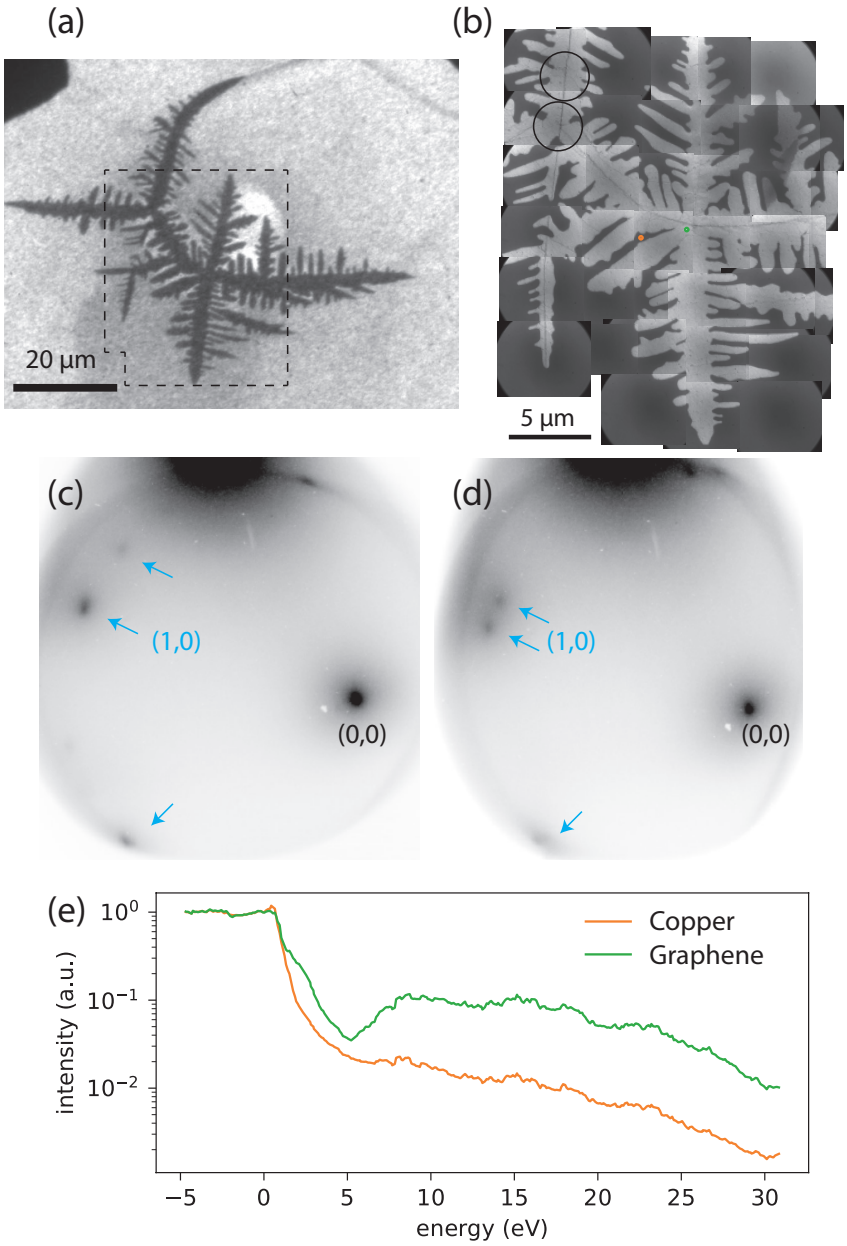

Figure 3.5: Characterization of a graphene island. (a) PEEM overview with the graphene island (dark) and copper background (light). (b) Stitched bright field LEEM image on the same location as (a), E = 1.2 eV. (c,d) Tilted diffraction patterns (inverted gray scale), at E = 28.8 eV. The (0,0) beam is indicated in the lower right. First order diffraction spots are pointed out by the blue arrows. Recording location indicated by lower black circle in panel(b) (for figure(c)), and upper circle (for figure (d)). (e) Spectra of the locations indicated by the spots with same the color in figure (b).

3.3.4. Scanning dark field: visualisation of graphene rotation

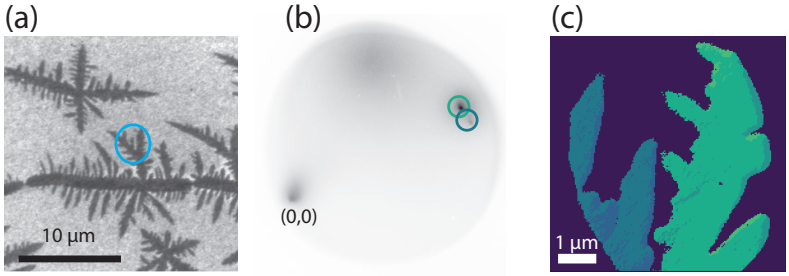

Figure 3.6: Angle spread within a graphene island. (a) PEEM overview. (b) Tilted diffraction pattern (inverted gray scale) of area indicated in (a) by the blue circle. The (0,0) spot is indicated in the lower left, first order diffraction spots (two orientations) are indicated in the upper right. (c) Composite LEEM dark field image of the two arms. Colours indicate on which contrast aperture position (as indicated in (b)) the highest brightness was found.

To visualize the spatial distribution of the different rotations present in an image, scanning dark field measurements are performed. Figure 3.6 (a) shows a PEEM overview of the area studied in this section, the part under investigation is pointed out by a blue circle. Figure 3.6 (b) shows the tilted diffraction pattern of this area. The (0,0) spot is indicated in the lower left. In the upper right two neighbouring first order spots are visible; they are indicated by blue circles. The two diffraction spots indicate that there are two crystalline orientations present in this area.
Because the first-order diffracted beams are relatively close together in this case, we will use a scanning dark field technique that assigns a rotational direction to an area. The protocol for this measurement is explained in the following paragraph.
Figure 3.6 (c) shows a scanning dark field measurement, which works as follows: we use tilted alignment as seen in figure 3.6 (b). The contrast aperture is inserted in the diffraction plane, in the same way as for a regular dark field measurement described in Chapter 2. Next, we scan the contrast aperture over a line following the circle arc of the first order spots. For every step of the aperture we record a real-space image. In this image an area will lighten up only if the atomic structure of the area contributes to the selected diffraction spot. By scanning the aperture over the different spots and recording real-space images, different areas will light up for different aperture locations.
The following analysis protocol is used to arrive at the compound image in figure 3.6 (c). We start with a series of real space images recorded for a set of aperture locations. We select for each pixel the frame in which it is brightest. In the resulting compound image (3.6 (c)) the colour of each pixel is given by the frame number in which it is brightest. The frame number is directly related to a contrast aperture location and therefore a lattice rotation. The colour coding in the circles of figure 3.6 (b) corresponds to the colours in figure 3.6 (c).
Inspecting figure 3.6 (c) we find that the rotational variation in the lattice can be related to the larger scale structure of the graphene island. In figure 3.6 (c) the

green and blue colour correspond to two different sub branches of the graphene island. This shows that the angular orientation of the graphene is, in this case preserved over a subbranch, but differs between the two subbranches.

3.4. Angle detection techniques on the fully grown graphene sample

In this section we turn our attention to the study of the fully grown samples. We find that in these samples both Moiré- and copper spots are present. This opens up additional possibilities to study the angular composition of this layer. Moreover, we are interested in large-scale characterization. The LEEM dark field measurements as performed in section 3.3.4 are less suitable for large area characterization. To obtain large-scale information on the angle spread of the fully grown graphene layer on copper we record a sequence of diffraction patterns (like the two examples in figure 3.7 (c) and (d)) on a grid of locations. This sequence of diffraction patterns will be translated into a local angle of the graphene with respect to the copper crystal beneath.
When we compare the diffraction patterns in 3.7 (c) and (d) to earlier diffraction patterns in this chapter (like the ones in figure 3.5 (c) and (d)), we observe that in the former copper- and Moiré spots have appeared. This is an important difference between the partially grown samples, studied in previous sections, and the fully grown samples, that will be studied in the coming sections. We assigned the absence of copper spots in the partially grown samples to oxidation of the copper surface and also interface between the copper and the graphene. In the fully grown samples the copper spots are visible. This is not too surprising because graphene is impermeable to oxygen [27, 28] and is hence expected to protect the copper from oxidation.
In the following section two image analysis techniques are developed as discussed in section 3.2.2. The first technique relies on detecting the location of one of the first order spots (purple circle in figure 3.7 (c) and (d)) with respect to copper first order spot (green circle in figure 3.7 (c)). The second analysis method determines the radius of the Moiré pattern, as formed by the red circled spots in figure 3.7 (c) and (d), around the (0,0) spot.

The two techniques are checked for consistency. If the copper lattice is single crystalline the two methods are equivalent. However, in the general case, i.e. if the copper orientation varies over the sample, the two techniques give different outcomes. The first order spot measures the absolute angle of graphene lattice, whereas the Moiré pattern is a consequence of the orientation of the graphene with respect to the copper.

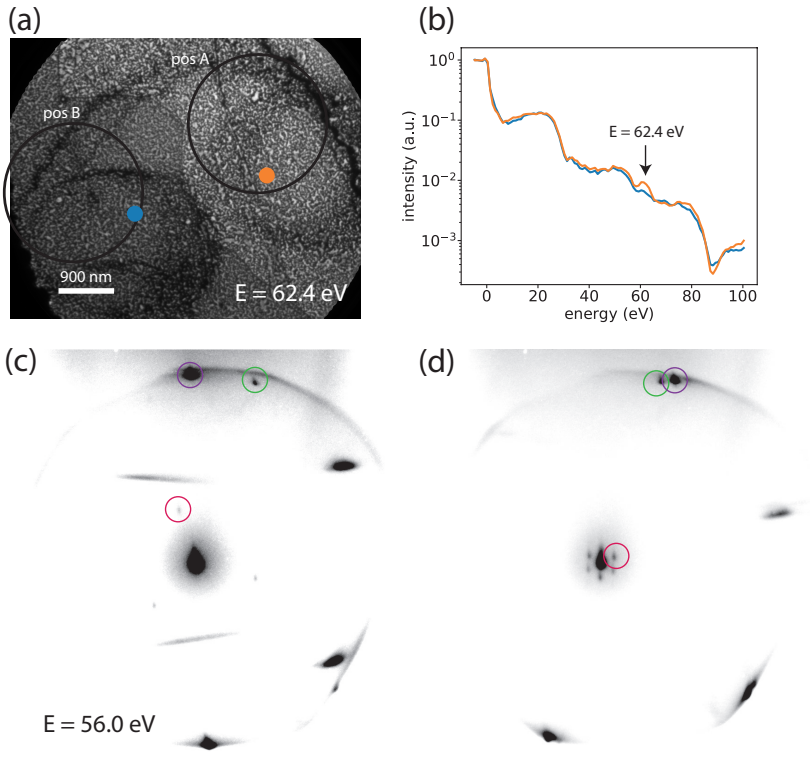

Figure 3.7: LEEM characterization of a grain boundary. (a) LEEM bright field image of a selected area at E = 62.4 eV. A line meanders over the FoV from the upper left to the lower right; subtle contrast is visible between the two sides. (b) Spectroscopic data on locations as indicated by corresponding colors in figure (a). (c,d) μLEED diffraction patterns at E = 56.0 eV recorded at position A (c) and position B (d) as indicated in figure (a). Colour coding: First order graphene diffraction spots (purple), Moiré spots (red) and first order copper spots (green).

3.4.1. First-order spot detection

The protocol for detection of the first order spots works as follows. First, the diffraction data is smoothened using a 4×4 pixel^2 Gaussian filter. Smoothening of the raw data serves two purposes. First, it avoids false positives from single high pixels sometimes present in the data. Second, the centre of the diffraction peak is found more accurately.

In the next step of the protocol we select the least deformed part of the Ewald sphere for spot finding. In figure 3.8 (a) the search region is indicated by the dashed line. The search region defines the spot selected for the analysis. Within this region, up to two local maxima are selected using the Python *skimage* package. The location of the (usually very dim) copper spot is manually determined for the full data set using a composite summation pattern of the full stack of diffraction

patterns.

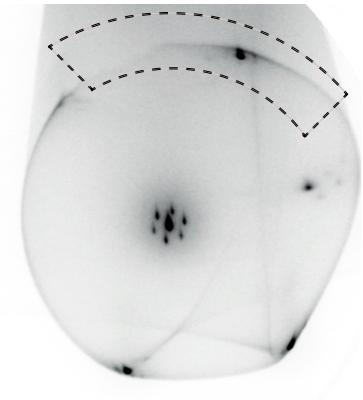

Figure 3.8: Gaussian smoothed diffraction pattern with Moiré spots (E = 69.0 eV). The search area for first order spots is indicated by the dashed lines.

3.4.2. Moiré radius detection

The Moiré pattern formed by the misalignment between the copper lattice and graphene can be observed as a hexagon around the central spot. The radius of the Moiré pattern is directly related to the angle between the copper and graphene lattices, by equation 3.1.
Next we explain the protocol used to automatically find the Moiré radius (r_{M}) from diffraction patterns. To measure the radius of the Moiré pattern, the diffraction pattern (figure 3.9 (a)) is first transformed to polar coordinates. The centre of the (0,0) spot is defined as r=0, as illustrated in figure 3.9 (a). Figure 3.9 (b) shows part of the diffraction pattern shown in (a) in polar coordinates. For this transformation a spline interpolation of order 1 was used, and the data were smoothened using a 5x5 pixel^2 Gaussian filter. For small radii (r<25 pixels) the central spot is the most prominent feature. For high radii (r>75 pixels) a high valued band around $\phi \approx \pi$ is observed. This band corresponds to the secondary electrons deflected to a preferred direction by the prisms. The sixfold symmetry can be seen around r=40 pixels.
The automated detection of the Moiré radius relies on Fourier analysis of each of the r(ϕ) columns of figure 3.9 (b). In figure 3.9 (c) the normalized sixfold symmetric (F[6]) Fourier component is plotted versus r. The six Moiré spots manifest themselves in a maximum in the sixth Fourier component (F[6], around r=40 pixels). To conclude, from the transformation to polar coordinates we can clearly deduce a sixfold symmetry around a well-defined r value, which is picked up by the Fourier transform.
The detected radii of the, as picked Moiré patterns are at the maxima of F[6]. Up to

two maxima per frame are saved, leading to one or two detected radii, or detected graphene rotations.

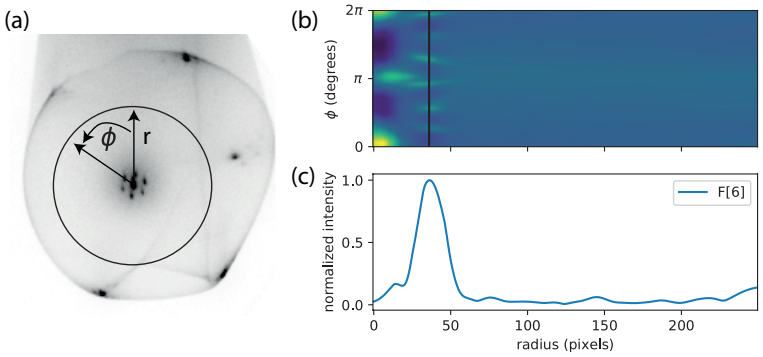

Figure 3.9: Fourier analysis of the Moiré pattern. (a) Raw data diffraction pattern with Moiré spots (E = 69.0 eV) on inverted gray scale. (b) Polar coordinate representation of figure (a) with the centre spots at r=0. (c) Radius versus F[6], the maximum around 40 pixels is the detected location of the Moiré pattern.

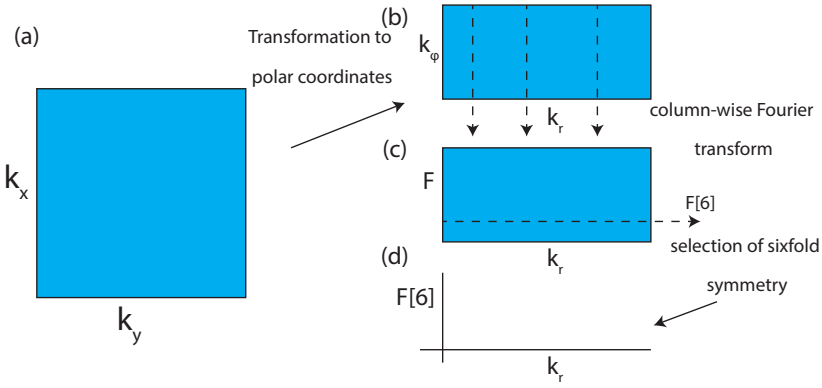

Figure 3.10: Schematic illustration of the data analysis protocol used to find the Moiré radius from diffraction patterns. (a) The input is a diffraction pattern. (b) This diffraction pattern is transformed to polar coordinates. (b) Every column is Fourier transformed, resulting in a 2D plot. (c) From this column-wise Fourier transform the sixfold component is selected for every k_r. (d) This results in a (k_r, F[6]) plot. The maxima, i.e. the points where the sixfold symmetry is present most strongly, give the k_r values for the Moiré radius.

3.5. Results

To benchmark the scanning μLEED technique for this type of sample two graphene on copper areas were measured. The first area is a small scale area (9× 9 μm). On a smaller area it is possible to take smaller steps and study smaller scale variations, if present. The second area is used to investigate large scale variations. The second area covers 67 × 67 μm^2.

3.5.1. Small scale variations

Figure 3.11 (a) depicts a LEEM bright field image at a landing energy of 61 eV. The area shows subtle contrast between a brighter area at the lower rim of the image and a darker part at the top, (cf. figure 3.7 (a)). Additional contrast is present, i.e. both small scale inhomogeneities and larger scale arcs. The latter contrast features will be discussed in the next paragraph.
The small scale features that we observe in the bright field images appear when the landing energy is ramped above 10 eV for the first time. After this first exposure the dark spots are visible over the full energy range, also below 10 eV. The same holds for the larger scale arcs on the sample. Additionally these arcs follow the beam shape around the first exposure spot. For these reasons we relate these features in the images to beam contamination. This type of beam contamination is typically observed for van der Waals materials at room temperature. A possible mechanism is the cross linking of free carbohydrates present on the surface, leading to amorphous carbon contamination on the surface.
Next, we will turn our attention to the scanning μLEED measurements as explained in Section 3.2.2. Diffraction data was recorded with a 500 nm (on the sample) aperture inserted in the image plane. The step size of the motors, or: the distance between subsequent data points, was set to 500 nm. In the data analysis we record up to two rotations per frame, both for the Moiré radius finding method and for the first-order peak detection. The orientation of the underlying copper lattice was used as the zero degree reference, and assumed to be constant over the scanning area for the angle calculation of the first-order spots. This assumption can be checked by a direct comparison between the two detection techniques.
After analyzing with both methods we first check for consistency between the two methods. Figure 3.11 (b) shows the correlation between the two techniques by plotting the angle of the first order spot versus the angle as calculated from the Moiré radius for all areas measured. The black line (x=y) serves as a guide to the eye. The area of the blue circles is proportional to the number of points in the cluster (area ∝ number of points in cluster). This figure shows that for the vast majority (96 percent) of data points both methods are consistent within 3 degrees accuracy. The consistency between the two different techniques shows that the orientation of the copper lattice is constant over this area.

In figure 3.11 (c) and (d) the detected angles (colour scale) are plotted versus measured sample location (the origin (0,0) being defined at the center of the plot) for the first-order spot detection (c) and the Moiré radius detection (d). In some

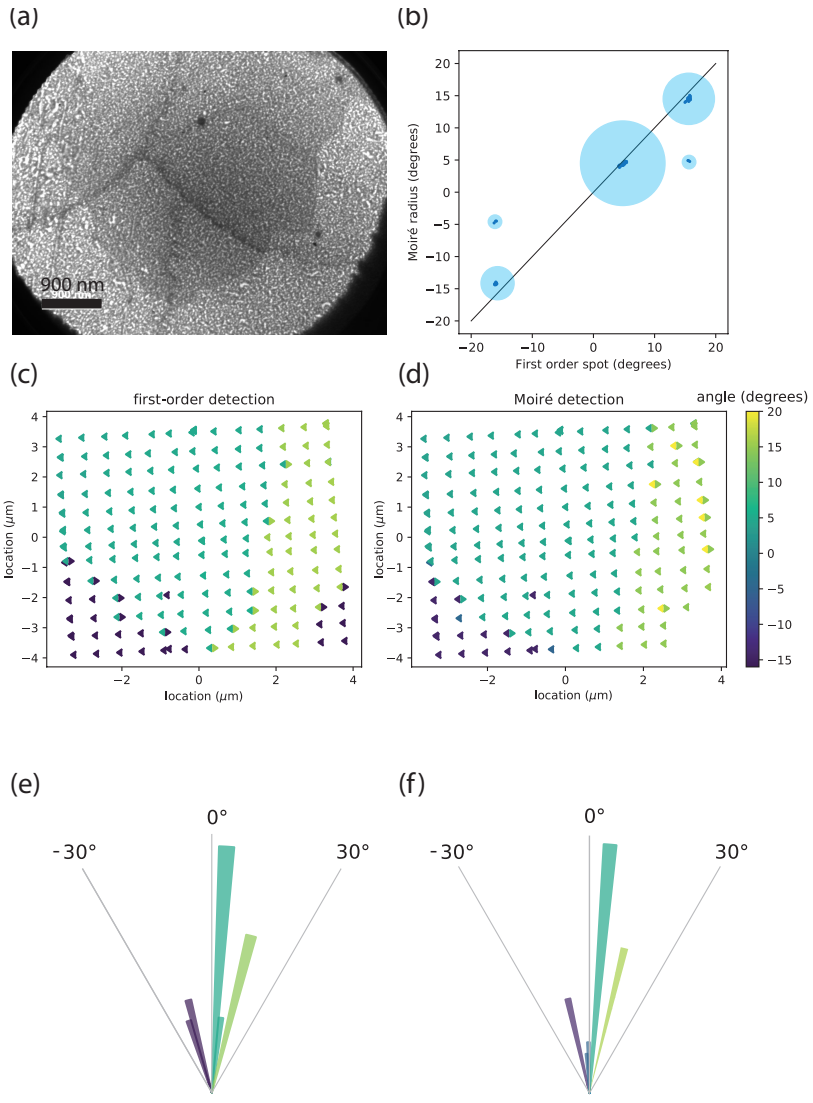

Figure 3.11: Scanning µLEED in a few-micron field of view (scanned area 9 x 9 µm^2). (a) Bright field image of the region of interest, E = 61.0 eV. The darkest arches are edges of earlier beam spots. Two contrast regions are visible. (b) Consistency check. Angle detected by the first order spot finding algorithm vs. angle as detected by the Moiré radius method. Black line (x=y) and blue circles (area ∝ number of points in cluster) are guides to the eye. (c, d) Scanning µLEED data of the area presented in figure (a). Angle is determined by the first-order spot finding method (b) and the Moiré-radius method (c). (e, f) Polar histograms of the distribution of angles in the first-order spot detection (e) and Moiré radius detection (f). The area of the slice is proportional to the amount of points in the bin.

cases one point shows a double triangle data point, this means two angles were measured by the first order spot method.
Comparing figures 3.11 (c) and (d) the consistency between the two analysis methods is quite good, as also seen in figure 3.11 (b). The points where this consistency breaks down are located at edges between two clusters, as seen in the purple cluster in the lower left and between the blue and the green cluster. In these instances the Moiré spot finding technique tends to not find the largest angle, and prefers the smaller angle that is also present in the measured area. Or, as in the lower right, not find an angle at all, leaving out those data points.
The spatial distribution of the angles on the sample clearly shows clusters of angles. The clusters have a typical size that is larger than this field of view. The double data points are mostly distributed at the boundaries between clusters, meaning that both clusters were observed in the same recorded diffraction pattern.
Moreover, the boundary between the large $\approx$ 5 degree cluster and the other clusters corresponds to the subtle contrast difference present in the real space image (figure 3.11 (a)). This shows that a rotation of the graphene with respect to the underlying copper lattice can also cause subtle contrast in a BF image. (and hence in the BF spectrum, at specific energies.
Figures 3.7 (e and f) show polar histograms of the same data as in panels (c and d). In these histograms the area of the bin slices are proportional to the counts in that bin. Again, the two methods look quite similar. The data points cluster in 5 bins (out of 11). This shows, again, that there are multiple, well-efined orientations present.

3.5.2. Large area characterization

Figure 3.12 (a) shows a stitched bright field LEEM image of a larger area on the same sample. The area covered by the measurement is 67x67 μm^2. In this figure, ellipsoidal shapes are present, originating from earlier beam exposures. Additionally we see lighter lines running over the whole area, two from left to right in the upper half and lower half of the stitched image, and another running up-down on the left side.
For every single image in figure 3.12 (a) a µLEED image was recorded and analysed. Figure 3.12 (b) shows the correspondence between the two spot finding methods used. Angles are defined with respect to the copper spot. The black x=y line is drawn in as a guide to the eye. In this data set the correspondence between the two methods is 88 percent within 3 degrees. This figure shows a spread of angles over almost the entire possible range of 60 degrees. The clustering of the angles is less clear then in figure 3.11 (b) for the small scale area, as may be expected for larger area.
Figure 3.12 (c) and (d) show the spatial distribution of the angles for both angle detection methods. The colour scale depicts the recorded angle with respect to the underlying copper. For some locations two angles are detected and plotted as a second triangle.

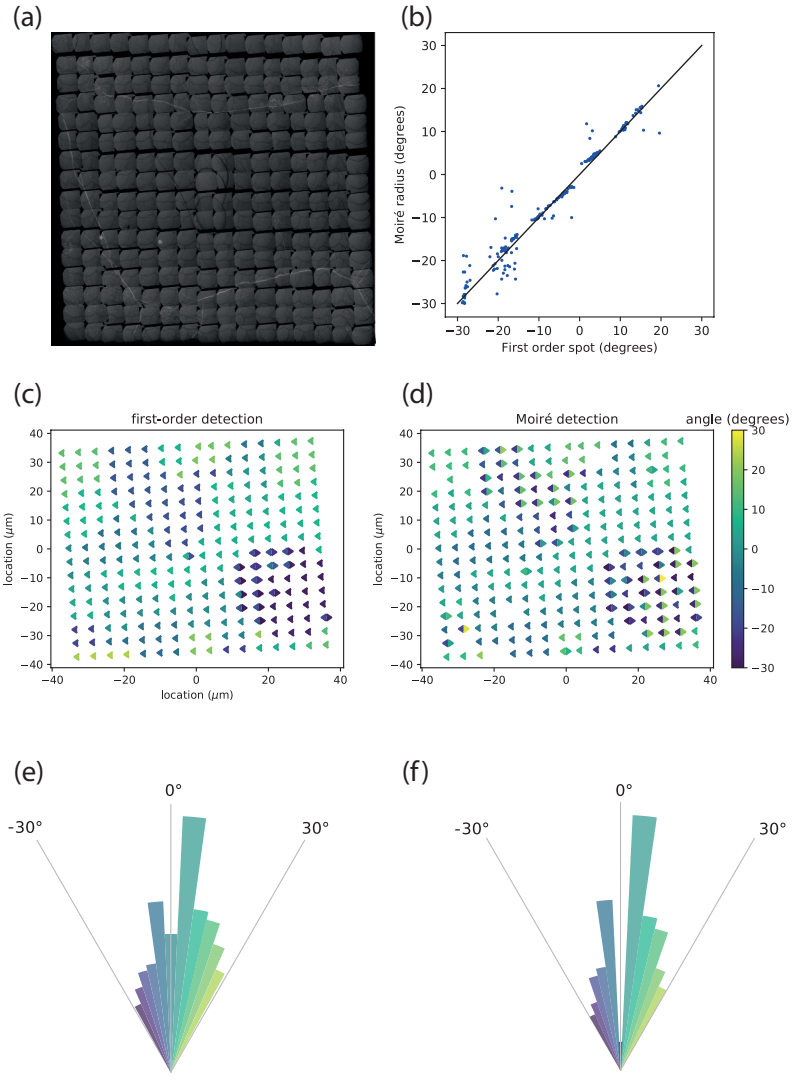

Figure 3.12: LEEM stitched bright-field image of the region of interest (scanned area 67 x 67 μm^2). At E = 61.0 eV. (b) Consistency check. Angle detected by the first order spot finding algorithm versus angle as detected by the Moiré radius method. Black line (x=y) is a guide to the eye. (c, d) Scanning μLEED data of the area presented in figure (a). Angle is determined by the first-order spot finding method (c) and the Moiré-radius method (d). (e, f) Polar histograms of the distribution of angles in the first-order spot detection (e) and Moiré radius detection (f). The area of the slice is proportional to the amount of points in the bin.

The spatial distribution of the graphene orientation shows large scale clustering of the measured angles. The size of the single crystalline patches is of the order of tens of microns. Most rotationally different patches are not directly related to clear features in the bright field image (figure 3.12 (a)). This demonstrates the added value of large scale μLEED techniques.
Figures 3.12 (e and f) show polar histograms of the same data as panels (c and d). Comparing to the earlier small scale measurement (figure 3.7 (e and f)), we observe more possible angles, i.e. all 11 bins show counts. An exception is around 0 ° in figure 3.12 (f). The gap in this figure is because very small Moiré radii are undetectable in this method.
From this large scale characterization we observe a spead in rotational directions in the graphene over these distances. This points to different graphene grains, that influence the electrical properties of the material. However, in the spatial distribution of angles we also observe large-scale pathways that are single crystalline over large areas.

3.6. Discussion of the results

In this chapter we have studied the angular composition of a mono layer of graphene on copper. Information on the growth dynamics was acquired by studying the angular composition of partially grown islands. From the different techniques used we acquired information on the growth process and quality of the graphene.
First we turn our attention to the growth process. The dendritic structures observed in the optical and PEEM images of the partially grown wafer give a very strong indication for diffusion limited growth. Moreover, the preferred growth orientations of the different dendrites and within a single dendrite (of 60° or 90° compared to the other dendrites) suggest preferred crystal orientations in the system. PEEM and bright field LEEM show homogeneous patches, however in dark field LEEM we observe rotational differences within a single island. The rotational variations are not present within a single straight branch. In contrast, branches that show an atypical inter-branch angle (non- 90° or 60°), or bending, there are rotational variations. It can be expected that these angular defects propagate in to the fully grown layer.
In the fully grown layer we observe large single crystalline patches of the order of tens of microns in size, i.e. with no rotational spread. But, indeed, over the larger scale there are orientation differences. The size of patches of one single orientation is similar to the typical island size, and sometimes exceeds this size. This gives some reason to believe that the different islands can merge into a single crystalline structure. The small patches of non-majority orientation could stem from the misaligned branches.
Next we will discuss the quality of the graphene for different electronic applications. For these applications an important, not discussed, step of transfer to a non-conducting substrate is needed. Note that this transfer is not trivial, but beyond the scope of this research.
Within the single crystalline graphene patches the electron mobility is expected to

be good and close that of exfoliated graphene. The electron mobility measured over two different patches, however, is expected to be dramatically lower, due to scattering at grain boundaries.
Due to the presence of rotational defects the graphene is not yet suitable for industrial wafer-scale applications in which perfect crystallinity is required.
However, the wafer measured in this chapter shows single crystalline patches that are large enough to accommodate (multiple) micron-sized devices consisting of pristine graphene. This opens the door to scientific experiments and industrial applications in which some degree of local variation is acceptable.

3.7. Conclusions

In this chapter we have presented two methods for automated detection of large-scale angular variation of graphene lattices on copper. The first technique relies on the detection of one of the first-order diffracted beams, the angle is defined with respect to the (0,0)-beam and the copper spot. The second technique detects the radius of the Moiré pattern formed due to the angular and lattice mismatch between the copper and graphene lattice. Moiré works very well for smaller angles, whereas for angles close to 30 degrees, first order spotetection is better. Overall the methods are consistent.
From partially grown samples we conclude that the growth is dendritic, which suggest a diffusion-limited growth mechanism. Single dendrites have a typical size of 50x50 μm^2 in the measured sample. From LEEM dark field measurements we conclude that single branches in the graphene dendrites are single crystalline. However, among different branches we observe some rotational misalignment.
In the fully grown wafer we observe very large single crystalline grains of about 50x50 μm^2. These sizes are large enough for typical transport experiments and show good promise in the direction of wafer-scale single crystalline graphene, needed for industrial applications.

References

[1] K. S. Novoselov, A. K. Geim, S. V. Morozov, D. Jiang, Y. Zhang, S. V. Dubonos, I. V. Grigorieva, and A. A. Firsov, *Electric Field Effect in Atomically Thin Carbon Films Supplementary,* Science **5**, 1 (2004), arXiv:arXiv:1402.6991v1 .

[2] A. S. Mayorov, R. V. Gorbachev, S. V. Morozov, L. Britnell, R. Jalil, L. A. Ponomarenko, P. Blake, K. S. Novoselov, K. Watanabe, T. Taniguchi, and A. K. Geim, *Micrometer-scale ballistic transport in encapsulated graphene at room temperature,* Nano Letters **11**, 2396 (2011), arXiv:1103.4510 .

[3] C. R. Dean, A. F. Young, I. Meric, C. Lee, L. Wang, S. Sorgenfrei, K. Watanabe, T. Taniguchi, P. Kim, K. L. Shepard, and J. Hone, *Boron nitride substrates for high-quality graphene electronics,* Nature Nanotechnology **5**, 722 (2010), arXiv:1005.4917 .

[4] L. A. Ponomarenko, A. K. Geim, A. A. Zhukov, R. Jalil, S. V. Morozov, K. S. Novoselov, I. V. Grigorieva, E. H. Hill, V. V. Cheianov, V. I. Fal'Ko, K. Watanabe, T. Taniguchi, and R. V. Gorbachev, *Tunable metalinsulator transition in double-layer graphene heterostructures,* Nature Physics **7**, 958 (2011), arXiv:1107.0115 .

[5] C. Dean, A. F. Young, L. Wang, I. Meric, G. H. Lee, K. Watanabe, T. Taniguchi, K. Shepard, P. Kim, and J. Hone, *Graphene based heterostructures,* Solid State Communications **152**, 1275 (2012).

[6] J. Xue, J. Sanchez-Yamagishi, D. Bulmash, P. Jacquod, A. Deshpande, K. Watanabe, T. Taniguchi, P. Jarillo-Herrero, and B. J. Leroy, *Scanning tunnelling microscopy and spectroscopy of ultra-flat graphene on hexagonal boron nitride,* Nature Materials **10**, 282 (2011), arXiv:1102.2642 .

[7] A. Castellanos-Gomez, M. Buscema, R. Molenaar, V. Singh, L. Janssen, H. S. Van Der Zant, and G. A. Steele, *Deterministic transfer of two-dimensional materials by all-dry viscoelastic stamping,* 2D Materials **1** (2014), 10.1088/2053-1583/1/1/011002, arXiv:1311.4829 .

[8] G. R. Yazdi, T. Iakimov, and R. Yakimova, *Epitaxial graphene on SiC: A review of growth and characterization,* Crystals **6** (2016), 10.3390/cryst6050053.

[9] Y. M. Tairov and V. F. Tsvetkov, *Investigation of growth processes of ingots of silicon carbide single crystals,* Journal of Crystal Growth **43**, 209 (1978).

[10] C. Berger, X. Wu, N. Brown, C. Naud, X. Li, Z. Song, D. Mayou, T. Li, J. Hass, A. Marchenkov, E. H. Conrad, P. N. First, and W. a. De Heer, *Electronic Confinement and Coherence in Patterned Epitaxial Graphene,* Science **312**, 1191 (2006).

[11] S. Nie, A. L. Walter, N. C. Bartelt, E. Starodub, A. Bostwick, E. Rotenberg, and K. F. McCarty, *Growth from below: graphene bilayers on ir (111),* ACS nano **5**, 2298 (2011).

[12] J. C. Shelton, H. R. Patil, and J. M. Blakely, *Equilibrium segregation of carbon to a nickel (111) surface: A surface phase transition,* Surface Science **43**, 493 (1974).

[13] N. C. Bartelt and K. F. McCarty, *Graphene growth on metal surfaces,* MRS Bulletin **37**, 1158 (2012).

[14] X. Li, W. Cai, J. An, S. Kim, J. Nah, D. Yang, R. Piner, A. Velamakanni, I. Jung, E. Tutuc, *et al.*, *Large-area synthesis of high-quality and uniform graphene films on copper foils,* science **324**, 1312 (2009).

[15] A. C. Ferrari, J. Meyer, V. Scardaci, C. Casiraghi, M. Lazzeri, F. Mauri, S. Piscanec, D. Jiang, K. Novoselov, S. Roth, *et al.*, *Raman spectrum of graphene and graphene layers,* Physical review letters **97**, 187401 (2006).

[16] D. Graf, F. Molitor, K. Ensslin, C. Stampfer, A. Jungen, C. Hierold, and L. Wirtz, *Spatially resolved raman spectroscopy of single-and few-layer graphene,* Nano letters **7**, 238 (2007).

[17] Y. Hao, Y. Wang, L. Wang, Z. Ni, Z. Wang, R. Wang, C. K. Koo, Z. Shen, and J. T. Thong, *Probing layer number and stacking order of few-layer graphene by raman spectroscopy,* small **6**, 195 (2010).

[18] C. Cong, T. Yu, K. Sato, J. Shang, R. Saito, G. F. Dresselhaus, and M. S. Dresselhaus, *Raman characterization of aba-and abc-stacked trilayer graphene,* ACS nano **5**, 8760 (2011).

[19] C. Casiraghi, S. Pisana, K. Novoselov, A. K. Geim, and A. Ferrari, *Raman fingerprint of charged impurities in graphene,* Applied physics letters **91**, 233108 (2007).

[20] A. Ellis and R. Tromp, *A versatile ultra high vacuum sample stage with six degrees of freedom,* Review of Scientific Instruments **84**, 075112 (2013).

[21] R. M. Tromp, J. B. Hannon, A. W. Ellis, W. Wan, A. Berghaus, and O. Schaff, *A new aberration-corrected, energy-filtered LEEM/PEEM instrument. I. Principles and design,* Ultramicroscopy **110**, 852 (2010).

[22] F. J. Meyer zu Heringdorf, M. C. Reuter, and R. M. Tromp, *Growth dynamics of pentacene thin films,* Nature **412**, 517 (2001).

[23] S. Nie, J. M. Wofford, N. C. Bartelt, O. D. Dubon, and K. F. McCarty, *Origin of the mosaicity in graphene grown on Cu(111),* Physical Review B - Condensed Matter and Materials Physics **84**, 1 (2011).

[24] O. D. D. Joseph M Wofford, Elena Starodub, Andrew L Walter, Shu Nie, Aaron Bostwick, Norman C Bartelt, Konrad Thurmer, Eli Rotenberg, Kevin F McCarty, *Extraordinary epitaxial alignment of graphene islands on Au(111),* New J. Phys. **14** (2012), 10.1088/1367-2630/14/5/053008.

[25] Z. Zhang and M. G. Lagally, *Atomistic Processes in the Early Stages of Thin-Film Growth,* **276** (1997).

[26] R. M. Feenstra, N. Srivastava, Q. Gao, M. Widom, B. Diaconescu, T. Ohta, G. L. Kellogg, J. T. Robinson, and I. V. Vlassiouk, *Low-energy electron reflectivity from graphene,* Physical Review B - Condensed Matter and Materials Physics **87**, 1 (2013).

[27] O. Leenaerts, B. Partoens, and F. Peeters, *Graphene: A perfect nanoballoon,* Applied Physics Letters **93**, 193107 (2008).

[28] J. S. Bunch, S. S. Verbridge, J. S. Alden, A. M. Van Der Zande, J. M. Parpia, H. G. Craighead, and P. L. McEuen, *Impermeable atomic membranes from graphene sheets,* Nano letters **8**, 2458 (2008).

4

Scanning ARRES

4.1. Introduction

A periodic lattice imposes boundary conditions on the quantum mechanical wave function of electrons: some states are allowed, and others are not. Together, the allowed states line up to form so-called bands, which are well-defined in reciprocal space (k-space): $\varepsilon(\mathbf{k})$. The collection of the allowed states (*bands*) and forbidden states (*gaps*) is referred to as the band diagram.
The electronic band structure of a material dictates virtually all of its properties, specifically its optical absorbance [1, 2] and its conduction properties [3]. This makes it a very relevant material property to probe, and this is widely done in different techniques. In the following paragraphs a short overview is provided.
Currently there exist many techniques to measure band structures. We will give

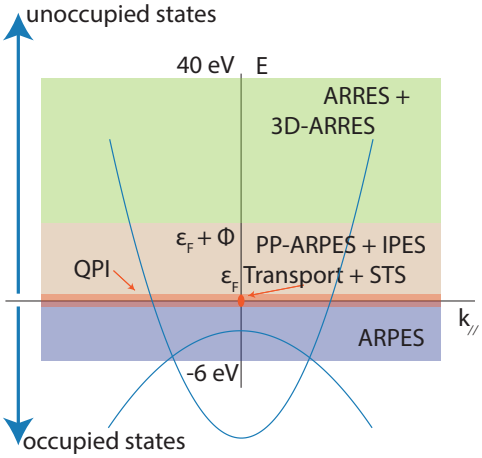

Figure 4.1: (E, $\mathbf{k}_{\parallel}$) diagram with several band structure measurement techniques schematically indicated. The energy on the y-axis is divided in occupied and unoccupied states. The different techniques are plotted within their operation energy range.

a short overview in this introduction and give an intuition for where the technique discussed in this chapter, i.e. scanning ARRES, fits in this landscape. These common techniques differ with regard to three parameters. First, the energy range in which a technique operates is a relevant parameter. Second, and connected to the energy range, is the division between occupied, and unoccupied states in the material. Finally, there is the question on whether a technique probes points, lines or surfaces in the Brillouin zone.
Figure 4.1 shows a very schematic overview of different techniques plotted against the energy they operate in. The blue parabolas are a schematic representation of a band diagram. The Fermi-level splits the surface of occupied states (below) and unoccupied states (above). In this chapter we will use the LEEM convention of defining the zero energy. This means that zero energy is at the electron vacuum level, i.e. at the Fermi energy plus work function, or affinity level for semi-conductors.

ARPES is based on the photoelectric effect: when a sample is irradiated with photons, an electron can absorb a photon and use this energy, if sufficient, to escape from the material. The electron will escape the material with a maximum energy with respect to the Fermi level of: $E_{kin} = h\nu - E_B$, where ν is the photon frequency, E_B is the the binding energy of the electron involved, i.e. the energy difference between the vacuum level and the energy of the initial electron state. [4].
By using an energy filter one can obtain energy-resolved information on the occupied states of a surface. Moreover, one can resolve the momentum distribution of the occupied states by measuring the angle at which the electrons leave the surface. This gives an (E, **k**) diagram that resolves the occupied band structure of a surface. ARPES typically operates in the measured energy range below the Fermi level to tens of eV below.

In a charge transport experiment, the current is formed by electrons (or holes) around the Fermi level only. Hence, a conductance measurement provides basic information on the availability of electrons, i.e. the presence of electron bands, around E_F. For semiconductors, the Fermi-level (ε_F) can be slightly modified by applying a back gate voltage. In semi-conductors this is widely used to move the Fermi-level in or out of the valence and conduction band. Using a typical back gate one can explore the availability of states in a material in an energy range of the order of 100 meV around the Fermi-level. [5] As we will see in chapter 5 this energy range can be pushed to the ±1 eV range by using an ionic-liquid gate.
Scanning tunnelling spectroscopy (STS) gives a more complete and very high resolution picture of the electronic states around the Fermi-level. STS is a modification of the scanning tunnelling microscopy (STM) technique, where the bias between sample and a sharp tip is varied, while keeping the height of the tip constant. The tunnelling current is measured and gives information on the local density of states (DoS) at the Γ-point. Typically the dln(I)/dln(V) curve is plotted, because this quantity is proportional to the local density of states (LDOS). [6] STS is a spectroscopy technique that can be used to measure the density of states, up to ±3 eV around the Fermi-level. [7–9]
Quasiparticle interference is a modification of STS. [10, 11] In this measurement the sample is decorated with elastic scattering centres, which induce standing electron waves on the surface. These can directly be probed. By Fourier transforming the real-space STM data the LDOS can be calculated as a function of (k_x, k_y). The STS techniques can be used to measure the energy dependence of this function, by varying the tip-sample bias.

Inverse photoemission spectroscopy (IPES) [12] is a technique to measure the unoccupied states between the Fermi level and the work function/ affinity level. In the basic experiment the sample is irradiated by a collimated low energy electron beam (0-20 eV). The electrons can be absorped in unoccupied states before decaying into lower lying electronic states, in this decay process a photon with a defined energy is emitted. The photons are measured and give information on the availability of

states. This technique can be seen as the inverse of ARPES: instead of by photons the surface is irradiated by electrons. And instead of measuring emitted electrons the technique measures emitted photons.
Pump-probe ARPES [13, 14] operates in a comparable energy range as IPES, i.e., above the Fermi level and below the work function. In this experiment the sample is exposed to two laser pulses: the pump (typically in the infra red) and the probe (typically in the ultra violet). The first pulse (pump) excites electrons from below the Fermi level to higher unoccupied bands. The second pulse (probe) has enough energy (> Φ) to photo-emit electrons. These electrons are measured.
Finally, for the highest energies, i.e. states above the vacuum level, plotted in figure 4.1 one can explore the LEEM-based angle-resolved reflected-electron spectroscopy (ARRES) technique (see Chapter 2). [15, 16] This technique is related to Very Low Energy Electron Diffraction (VLEED), which operates in k-space. [17, 18] In the ARRES technique a surface is irradiated with electrons of varying energy and angle. The reflectance for a certain (E, **k**) value is related to the availability of an unoccupied electronic state in the material. Figure 4.2 shows such an ARRES map of hBN over the high-symmetry lines of the first Brillouin zone, taken from reference [16]. In the figure the calculated band structure of hBN is plotted in black. We see that high reflectance (red) is correlated with a calculated band gap, i.e., the absence of electronic states.

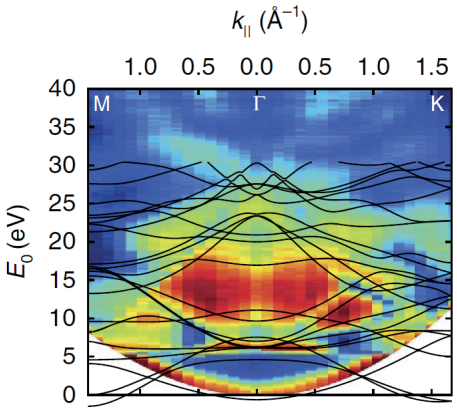

Figure 4.2: ARRES measurement of bulk hBN. Electron reflectivity as a function of E and $\mathbf{k}_{\|}$. Overlay of black curves is the calculated bandstructure of hBN. Figure taken from ref. [16].

4.2. The Brillouin zone of a hexagonal lattice

In this chapter we will investigate the unoccupied states of two hexagonal lattices: molybdenum disulphide (MoS_2) and hexagonal boron nitride (hBN). The hexagonal nature of these lattices leads to similarities in the measurements. For both materials the symmetries of the diffraction pattern will be the same. This shared basis will be explained in the following section.
In addition to the diffraction pattern and its spectroscopic features, the LEEM back focal plane also holds information on the unoccupied band structure of the materials studied. The band structure is the collection of states available to electrons in the material, for different **k**-vectors and energies. As a consequence of the periodic atomic structure of the lattices studied, the band structure also has a periodic structure in reciprocal space. The repetitive unit of this periodic structure is the Brillouin zone (BZ). In the following paragraphs the construction of the BZ for hexagonal lattices will be explained.

Figure 4.3 (a) shows a schematic diagram of the hexagonal diffraction pattern, the black dots indicate the diffracted beams for a collimated electron beam at normal incidence. The center dot indicates the (0,0) beam, around which the first order diffracted beams form a hexagon - characteristic for this crystal structure. The symmetry of the diffraction pattern is the same for both MoS_2 and hBN. However, the size of the real space unit cell is different, which means that the reciprocal distance between the center and first order diffracted beams, being related to the inverse of the real-space unit cell, differs.
In figure 4.3 (a) the first Brillouin zone (FBZ) is drawn in cyan. The construction of the FBZ is done as follows. The M-point is found on the middle point of the line drawn between the (0,0) beam (the Γ-point) and the first-order diffracted beam. If we now draw six lines through the M-points and perpendicular to the line running from Γ to M, we enclose the FBZ hexagon. The K- and K'-points are situated on the corner points of this hexagon.
Figure 4.3 (b) shows the FBZ of a hexagonal lattice, with the high symmetry points indicated. The cyan triangle in the upper right is indicated as the smallest unit of the periodic structure of the BZ. The remainder of the BZ can be constructed by mirroring and rotating this unit. For this reason we will use this unit for measurements in this work.
Figure 4.4 shows the atomic structure of MoS_2 (a) and hBN (b). For both structures the top view shows a hexagonal structure. However, the unit cell of this structure contains two different atoms: molybdenum and sulfur for MoS_2 and boron and nitrogen for hBN. The alternating pattern of atoms reduces the sixfold symmetry to a threefold symmetry. The K and K' points in figure 4.3 (b) translate this symmetry to reciprocal space in a threefold symmetry.
Figure 4.3 (c) shows the periodic filling of k-space with BZ units. The first BZ is indicated in blue and is situated around the Γ-point. Higher order BZ's are situated around higher order diffracted beams. Here, some of the second BZ's are indicated in green.
In the measurements it is desirable to spatially oversample the BZ, meaning that

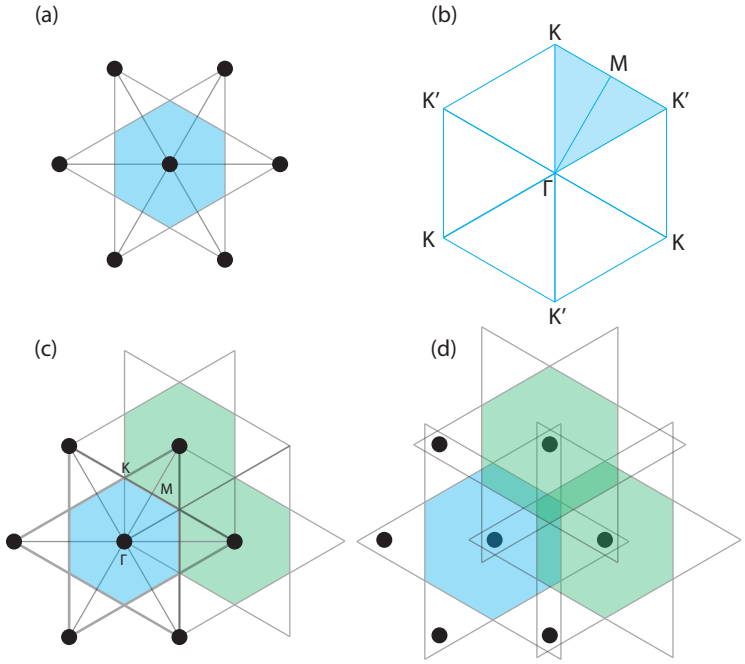

Figure 4.3: Construction of the FBZ of a hexagonal lattice in k-space. (a) Schematic representation of a diffraction pattern of an hexagonal lattice. Black dots are the diffraction spots, center spot is the (0,0) beam, first order spots are drawn in as black dots. The center blue hexagon is the FBZ. (b) FBZ of a hexagonal lattice with high symmetry points drawn in. Γ-point in the center of the hexagon, K and K'-points are found at the corner points, the M-point is constructed on the edge of the FBZ centered between the K and K'-points. (c,d) k-space filled in with the FBZ (cyan) and two second BZ's (green) formed by the first order diffracted beams. Illustration of perfectly sampled BZ's (c) and the over-sampled case in (d).

we scan over a larger reciprocal area than only the first BZ. The main reason for this is to have the possibility to crop off the edges, which can give some edge related errors. The situation in which the first BZ is oversampled is illustrated in figure 4.3 (d). In this figure the first BZ is indicated in blue. The contrast formed by the order diffracted beams, the second BZ, is drawn in green for two first order spots. In the oversampled BZ's, the different order BZ's start to mix and overlap at the edges. This would obscure the measurements if we were to measure the full FBZ, especially on the K-K' high-symmetry line.
In order to avoid this issue, we limit the imaging area to the triangle running from Γ to K, to K'. By measuring just this irreducible triangular part of the FBZ, we can reconstruct the full FBZ, using the known threefold and mirror symmetries.

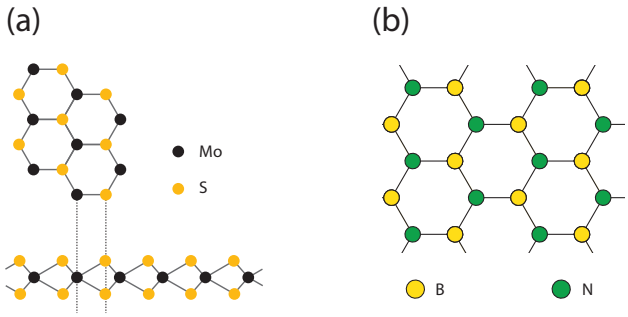

Figure 4.4: Atomic structures of single layer MoS_2 (a) and hBN (b). (a) Top view (upper panel) of MoS_2 with Mo atoms indicated in black and S atoms indicated in yellow. Side view (lower) of the sample single layer. (figure adapeted from [19].) (b) Schematic atomic structure of hBN with B indicated in yellow and N in green. (figure adapeted from [20].)

4.3. Methods: scanning ARRES

In the following section the methods used to take (E, **k**) measurements of the FBZ will be explained. As discussed in the introduction (Section 4.1) LEEM gives the possibility to measure the presence of unoccupied states of a material from the vacuum level up to 60 eV above the vacuum level. However, ARRES data are typically only acquired along high symmetry lines (K-Γ-M) in the first order BZ.
Instead of measuring reflectance over one-dimensional high-symmetry lines as done in regular ARRES [16], here we measure the full FBZ by scanning the incident electron angle over the full set of angles needed. This gives a two-dimensional (k_x, k_y) measurement of the reflectance (R) of the FBZ for a certain energy. This is done for varying landing energies, building up a three dimensional R(E, k_x, k_y) diagram.
In order to measure an ARRES-diagram both the electron energy and the in-plane momentum ($\mathbf{k}_\parallel$) need to be varied. The electron energy is set by varying the sample potential relative to the fixed electron gun potential. The variation of the in-plane momentum is achieved by tilting the electron beam with respect to the sample. This tilt is induced by deflection of the incoming electron beam in an imaging plane, giving rise to a shift in the diffraction plane. In figure 4.5 (a) the location of this deflector (DEFL1) is indicated in a schematic LEEM diagram. The deflector consists of two sets of electromagnetic steering coils, for the k_x and the k_y directions. (See Chapter 2.)
In past experiments, the measurement protocol for ARRES has been notoriously slow. For every (k_x, k_y) data point along a high symmetry axis, a frame (exposure time of 250 ms) is recorded. This process is repeated for every energy and k value. Depending on desired resolution in both in-plane momentum and energy and the desired exposure time, these full measurements take up to eight hours to com-

plete. Additionally it is not feasible to measure significantly more (k_x, k_y) values in a single measurement, as the -already long- measurement time would increase significantly, to the order of days.

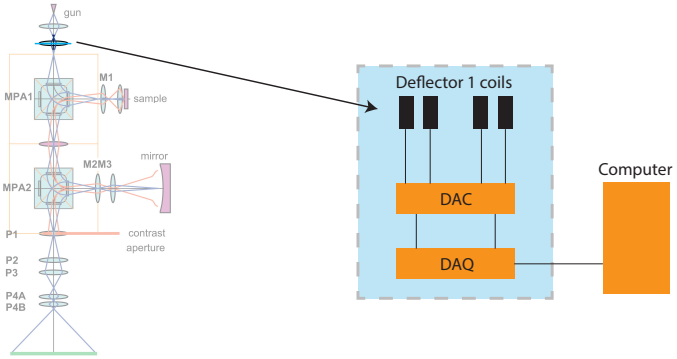

Figure 4.5: (Left) Layout of the LEEM setup, highlighting the location of the deflector used to tilt the beam for scanning ARRES measurements. Figure adapted from [21]. (Right) Schematic of the electronics used for fast scanning of the deflector. The computer calculates an array of (x,y) coordinates and sends this array to the data acquisition hardware (DAQ). This array is saved in the DAQ, enabling the remainder of the electronics to function without further communication with the computer (this independent part of the electronics is indicated by the dashed blue box). The DAQ sends a digital signal ((x,y) coordinates) to the digital-to-analogue converter (DAC). The DAC converts the digital voltages to currents suitable for the deflector coils (x and y).

4.3.1. Improved set-up

The lack of speed in ARRES measurements is caused by two main bottle necks: first, the exposure time of the camera needed to acquire high enough signal-to-noise ratio in the images; second, the communication between the measurement software and the instrument. To tackle the first bottle neck, the number of recorded frames needs to be reduced significantly. This can be done by recording multiple (k_x, k_y) within a single frame. This is allowed, because values at each $\mathbf{k}_\parallel$ are spatially separated in the back focal plane. This alone significantly reduces the acquisition time. To further speed up the protocol, we will also bypass the second main bottle neck: the computer-instrument communication for tilt scanning. In the standard protocol the computer communicates each (k_x, k_y) value separately to the current supply of the deflector. Figure 4.5 (b) shows the schematic of the improved set-up. In this scheme the computer calculates a full array of (k_x, k_y) values to measure the FBZ, from high symmetry points that are given as an input. This full array is sent to the data acquisition hardware (DAQ). The DAQ loops over this array without further computer communication.
The DAQ output voltage is converted to a current suitable for the deflector coil.

For this a voltage-to-current (VI) converter was designed and home-built. The two main design considerations have been: first, the speed at which the deflector can be scanned. This scanning speed will both influence the data acquisition speed, and the number of points within a scanned FBZ, i.e., the homogeneity of the scanned image. For the output speed a stable output frequency of 100 kHz was chosen. The second design consideration has been the maximum output current. To enable deflection large enough to scan the FBZ of materials like graphene and hBN a maximum bipolar deflector current up to $\pm$100 mA is needed. In order to protect the deflector coils from overheating the VI-converter is capped at a $\pm$100 mA value. The circuit used to meet the requirements is modeled after the so-called improved Howland circuit[22]. More details on the implementation and the circuit can be found in appendix C.
The data acquisition device used for the scanning is a *Multifunction Measurement and Control* USB-2637 DAQ by the brand Measurement Computing [1]. This DAQ was selected because of its high output frequency (1 mega sample/s). It has four analogue outputs, of which we need two for the experiments in this chapter.
The resulting set-up, as sketched in figure 4.5, will be used to record single-frame FBZ images. The aim is to record spectroscopic stacks of these images by changing the landing energy. For this we will first check the uniformity of the FBZ image using a Si(111) sample in mirror mode, in the following paragraphs.

4.3.2. Benchmark measurements

To benchmark the fast scanning hardware, the following test measurements are done. Figure 4.6 (a) illustrates the measurement protocol. The blue ellipses denote (0,0) beams, imaged in the back focal plane. The displacement of the beam is induced by fast scanning of deflector 1, as introduced in chapter 2.
The coordinates are a hexagonal (close packed) filling of a user defined triangle. The triangle is filled row by row, top to bottom, in a meandering fashion. When the triangle is filled up, the beam is moved in the opposite direction and we repeat the procedure back to the starting point. This scan is repeated a couple of times for each frame.
The chronology of the scan was chosen for several reasons. First, in the fast scanning mode the distance the beam can move in a short time frame is limited by the deflector coil impedance. When the steps are too large, the location of the beam becomes ill-defined, as it will lag behind. Therefore it is of importance to use a scanning scheme with only small steps of the same size. Second, the scanning is done at a speed close to the maximum speed at which the system is stable, see appendix C. This means that every beam move that is not part of the planned triangle will be visible in the measurement, leading to additional features in the image. Finally, it is desirable to repeat the scan over the same triangle multiple times per frame to average out electron gun instabilities.
Figure 4.6 (b) shows the scanning area in the diffraction plane in cyan, with the

[1] https://www.mccdaq.com/

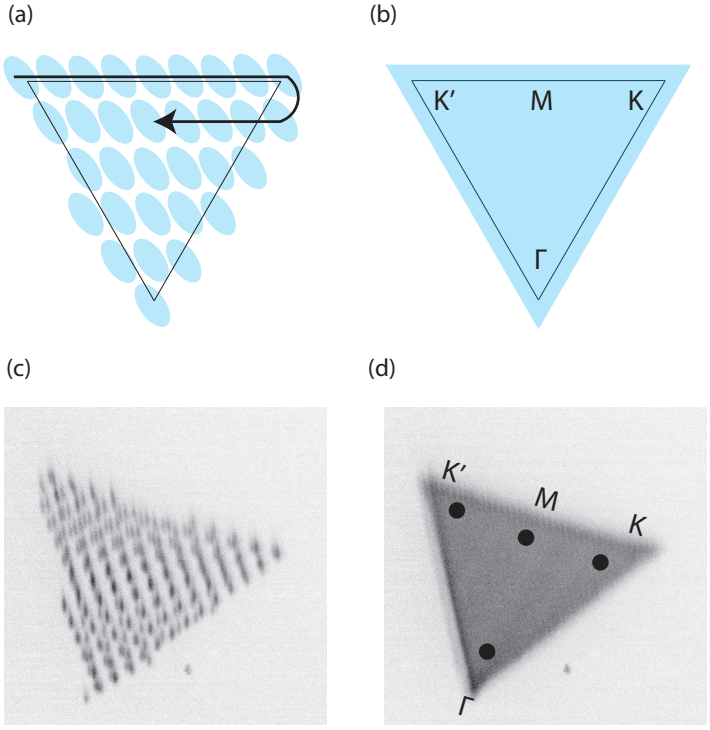

Figure 4.6: Scanning to pseudo-continuous imaging of the diffraction pattern. (a) Schematic illustration of scanning with a low point density. The black triangle depicts an slice from the FBZ, blue dots are the specular deflected beams at different tilt values, arrow shows scanning direction. In the scanning routine the beam is always scanned back and forth in both directions. (b) Schematic illustration of a pseudo continuous scan, with a higher point density. Sampling is also done outside the FBZ ('oversampling') for avoid edge effects. (c) Measurement of a scanning beam at low point density in mirror mode (E = -5 eV). Individual beam spots are clearly visible. Gray scale is inverted for image clarity. (d) Measurement of a pseudo-continuous scan in mirror mode (E = -5 eV), with indication of the location of high symmetry points. Gray scale is inverted for image clarity.

high symmetry points annotated. The region of interest (part of the FBZ) is indicated by the black triangle. The goal of the measurement is to increase the point density, i.e. decrease the single step size, such that the triangle is homogeneously illuminated. Additionally, we will spatially sample outside of the FBZ, as indicated by the cyan triangle reaching beyond the FBZ slice. This oversampling is used to avoid any scanning edge effects. The triangle scan is repeated around 50 times for each frame.

Figures 4.6 (c) and (d) show measurements of this scanning protocol, at low point density (c) and high point density (d). In the figures the gray scale of the original images is inverted for image clarity. The measurements are taken from a Si(111)

sample, at a landing energy of E = -5.0 eV, i.e. an energy at which no sample interaction is possible. In figure 4.6 (c) the individual beam spots are still easily identifiable. The spacing between the points is irregular, because the scan grid was defined in this way. In figure 4.6 (d) the overlap between the points is large enough to get a relatively homogeneous triangle in a single frame. The high symmetry points are indicated in this scan.
For the benchmark measurements we thus observe a homogeneous triangle and a well-performing measurement protocol. In the next section the technique will be applied to MoS_2 and hBN samples. The triangle, as shown in figure 4.6 (d) will be recorded for a series of landing energies, in order to obtain the spectroscopic information on the FBZ.

4.4. Results

In the following section the scanning ARRES measurements for two van der Waals materials will be discussed. Before diving into the MoS_2 and hBN data a general explanation of the typical figures is provided in the next paragraphs.
The raw data consist of a stack of images of scanned triangles recorded between and slightly beyond, the high symmetry points: Γ- K - K'.
These raw data are shown in figure 4.7 for two different energy values ((a) E = 8.8 eV and (b) E = 21.2 eV). The figure is annotated with several features of relevance. First, in white, the projected Ewald sphere is drawn in. As expected the radius of this sphere is larger at higher energy. More attention will be spent on this in a later part of this section. Second, the triangle over which the scan is performed is annotated in green. Thirdly, in panel (b) we observe a bright round feature in the upper part of the Ewald sphere, annotated by the yellow arrow. This is caused by the secondary electrons, i.e., electrons emitted via inelastic processes. Finally, indicated in blue, are the triangles formed by the first-order diffracted beams. These raw data undergo a number of analysis steps, which will be described in the following paragraphs.
The first step is to crop the triangle along the high symmetry axes, as indicated in figure 4.8 (a) by the dotted lines. During measurement the locations of the Γ, K and K' points in the backfocal plane are recorded. The coordinates resulting from these recordings are used to determine the high symmetry points in the stack of FBZ images.
In the second step, the FBZ is visualized by symmetrizing the cropped triangles in a threefold symmetry. For this, the measured triangle is alternately mirrored (to place K on K and K' on K') and additionally rotated, as illustrated in figure 4.8 (b). Due to experiment-related deformations in the diffraction plane, the triangles are not perfectly equilateral. An affine transformation is used to fit the triangles in a hexagonal symmetry. This completes the energy cuts that are presented in this thesis.
From this full data set, i.e. scanning ARRES, we also construct a regular ARRES plot along the high-symmetry axes. For this figure we determine the intensity of the sig-

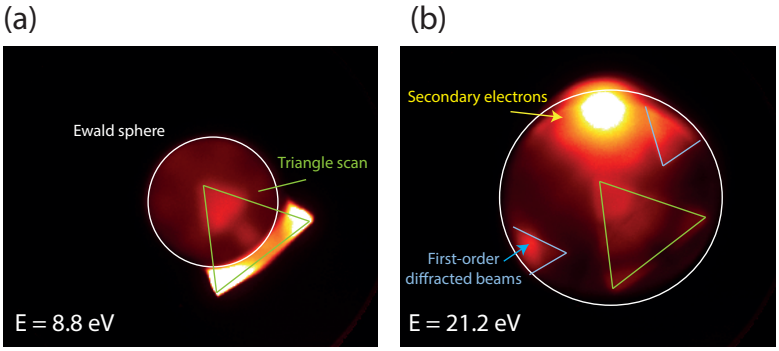

Figure 4.7: Raw backfocal plane data of scanned triangles. (a) Scan at E = 8.8 eV. (b) Scan at 21.2 eV. Features of interest are annotated.

nal along the axes □-K'-M-Gamma-K, respectively, as visualized in Figure 4.8 (c). This intensity profile is plotted for all landing energies. Because of gun current fluctuations over time, the figures shown in the main text are filtered; see appendix B.

For both the constant energy cuts and in the band diagram plots there is contrast between light and dark areas. This contrast is induced by the reflectivity of the material at that specific in-plane electron momentum, and energy. A bright colour means high electron intensity, i.e. high reflectance and a dark colour means low intensity and low reflectance from the sample.

The R(E, $\mathbf{k}_{\parallel}$) information is limited at low energy by the mirror mode transition. In the R(E, $\mathbf{k}_{\parallel}$) plot this is seen as a high intensity area that varies in $\mathbf{k}_{\parallel}$ value depending on E. This high-intensity area is also present outside the Ewald sphere in figure 4.7 (a). This is described by the mirror mode transition: the transition from total electron reflection to sample interaction while increasing the landing energy. This will be explained next.

First, let us focus on electrons at normal incidence. In this case the component of the momentum parallel to the surface is zero ($\mathbf{k}_{\parallel} = 0$) and all kinetic energy is in the perpendicular component of the momentum ($\mathbf{k}_{\perp}$). At negative landing energies, electrons at normal incidence do not have enough energy to reach the sample and are fully reflected without sample interaction: defined as the mirror mode. When increasing the landing energy to positive values, sample interaction is enabled. Sample interaction leads to a decrease in reflectance compared to the mirror mode intensity. Moreover, in the energy range above the mirror mode sample features can be measured.

Next, we consider electrons at off-normal incidence. For (scanning) ARRES measurements the off-axis condition is met for all momenta, besides the Γ-point. In this case the momentum of the electron is divided between a perpendicular component ($\mathbf{k}_{\perp}$) and a non-zero parallel component ($\mathbf{k}_{\parallel} \neq 0$). The kinetic energy contained in the parallel ($E_{\parallel}$) and normal ($E_{\perp}$) component of the momentum in vacuum are

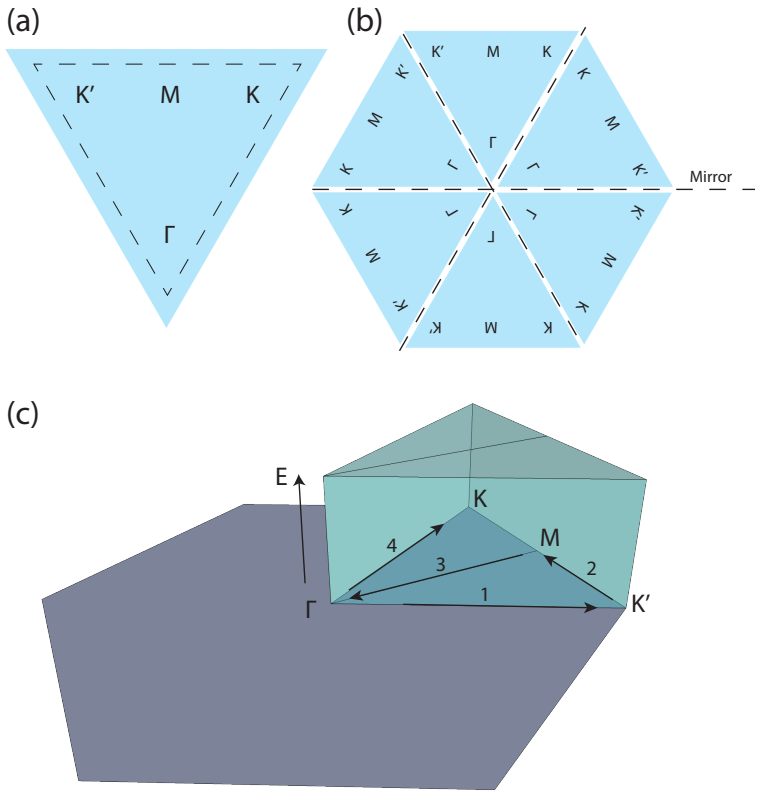

Figure 4.8: Illustration of the data visualisation and analysis steps. (a) oversampled scanned triangle in cyan, the dotted line indicates the crop along the high symmetry axes. (b) The triangle is copied, mirrored and rotated to fit in to the full-Brillouin zone symmetry. (c) 3D Illustration of the full data set consisting of the triangles as illustrated in panel (a) and (b) and the energy axis along the vertical. The high symmetry lines are indicated, with the order and direction used for the band diagram plots indicated by arrows.

given by the electron vacuum dispersion:

$$E_{\parallel} = \frac{\hbar^2}{2m_e}\mathbf{k}_{\parallel}^2, \quad E_{\perp} = \frac{\hbar^2}{2m_e}\mathbf{k}_{\perp}^2 \tag{4.1}$$

where m_e is the electron mass. The energy available for the perpendicular component is reduced by the parallel component and therefore the mirror mode transition energy (where $E_{\perp} \leq 0$) is increased compared to normal incidence. Instead of a transition at E=0 eV, a higher landing energy is needed for sample interaction.

In the R(E, $\mathbf{k}_{\parallel}$) diagram the dispersion as described in eq. 4.1 is directly measured. The mirror mode transition is seen as a parabola in E($k_{\parallel}$). At energies below this parabola full reflectance is measured ($E_{\parallel} < \frac{\hbar^2}{2m_e}\mathbf{k}_{\parallel}^2$, mirror mode), above this

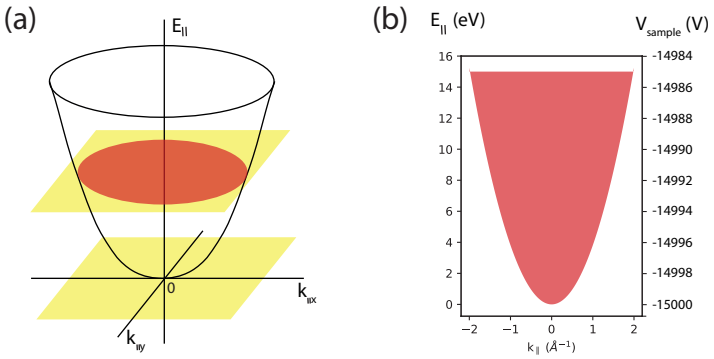

Figure 4.9: Illustration of the mirror mode transition for off-normal ($\mathbf{k}_\parallel \neq 0$) beam incidence. (a) 3D illustration of the paraboloid that defines the mirror mode transition in ARRES. At E = 0 eV (bottom yellow plane) the full diffraction plane is in mirror mode, at higher energy (upper yellow plane) the orange circle indicates the Ewald sphere; the yellow plane outside the circle is in mirror mode. (b) Vertical cut of the paraboloid in (a) through Γ. The region below the parabola is in mirror mode. Gun voltage is set at 15 kV.

parabola ($E_\parallel > \frac{\hbar^2}{2m_e}\mathbf{k}_\parallel^2$) the reflected intensity shows the result of sample interaction. The mirror mode parabola is plotted in figure 4.9. Panel (a) shows the 3D paraboloid. The inside of the paraboloid is the region where sample interaction is allowed. Panel (b) shows a vertical cut of this parabola. On the y-axis both the parallel component of the energy ($E_\parallel$) and the sample voltage (V_{sample}) are indicated.

In the constant energy cuts we plot (k_x, k_y) intensities at a certain energy. In figure 4.9 (a) this type of measurement is indicated by the horizontal cuts; one at $E_\parallel$ = 0 V and one at $E_\parallel$ > 0 V. Equation 4.1 restricts the length ($\mathbf{k}_\parallel^2$) of the in-plane momentum vector for a constant E value. For $\mathbf{k}_\parallel^2 > \frac{2m_e}{\hbar^2}E$ there is no sample interaction, and the (k_x, k_y) values outside this circle are in mirror mode. Within this sphere ($\mathbf{k}_\parallel^2 < \frac{2m_e}{\hbar^2}E_\parallel$); the yellow plane outside the circle is in mirror mode.

To summarize, for energies below E=0 eV the full FBZ is in mirror mode. When the landing energy is increased to positive values, a lower intensity circle opens up from the center of the FBZ (Γ-point, $\mathbf{k}_\parallel$ = (0,0)). This sphere is the collection of k-points that allow for electron-sample interaction, see figure 4.7 (a). (The opening of this circle is analogous to the opening of the projected Ewald sphere in regular LEED.) Within the circle, the reflected intensity is proportional to the coupling between the incoming plane wave and the outgoing reflected plane wave. This coupling depends on elastic and inelastic, reflective and absorbent processes induced by the material and its band structure.

Inelastic processes include a secondary electron background, which are the electrons emitted by inelastic processes. This causes a higher background intensity, see figure 4.7 (b). Additionally, inelastic interactions with surface defects cause a general decrease in measured intensity.

For the elastic processes, the availability of electronic unoccupied states is most

relevant. As we will see, the measured reflectance is related to the presence of an available state (or band) in which case the electrons are absorbed and the reflectivity is reduced. In contrast, in the absence of such a state, electrons are reflected. [23, 24] Additionally there are broadening effects induced by the angular spread stemming from corrugation of the sample (broadening in $\mathbf{k}_{\parallel}$) and chromatic spread of the incoming beam (broadening in E). [18]

4.4.1. Hexagonal boronnitride

Hexagonal boronnitride (hBN) is a van der Waals material. It can be exfoliated down to monolayer thickness. [25]. Because hBN is a wide-bandgap insulator [26] it is popular as a very flat substrate and as an insulating spacer in graphene devices, e.g. for gating. [27, 28]

Sample characterization

The hBN sample[2] used in this section consists of a silicon (100) wafer covered by hBN flakes. The hBN sample was fabricated by tape exfoliation followed pick-up from the SiO_2 using polypropylene carbonate (PPC) and transfer to the silicon substrate. This is a common procedure for 2D materials. [29, 30]
Figure 4.10 (a) shows a PEEM overview of a part of this flake. The light gray triangle is hBN, the darker gray around the flake is silicon. In yellow, the region of the scanning ARRES measurements is indicated. The darker patches in the flake are due to earlier beam exposures.
Figure 4.10 (b) shows the energy-dependent reflectivity at the Γ point of the flake shown in panel (a), taken at T=600 °C and imaged using a beam current reduced to 0.001 µA (compared to 2.0 µA in normal operation) to avoid charging effects as much as possible. The curve shows overall features that are typical for bulk hBN [31]. However, the mirror mode transition appears at higher energies. This change of the spectroscopy at lower energies is typically seen in insulating samples. This happens because electrons used to image also charge the sample and shift the mirror mode transition.

Scanning ARRES measurements

Figure 4.11 presents the scanning ARRES data taken on the hBN sample. Panel (a-h) show selected constant energy cuts of the reflectivity, with per-frame optimized contrast. For the lowest energy presented here (panel (a)) the far edges have not transitioned from mirror mode yet and most of the contrast is due to this mirror mode transition, forming a circle in $\mathbf{k}_{\parallel}$-space (see figure 4.9).
The band diagram plot along the high symmetry axes, deduced from the full data

[2]The fabrication of this hBN sample was performed by J. Jobst.

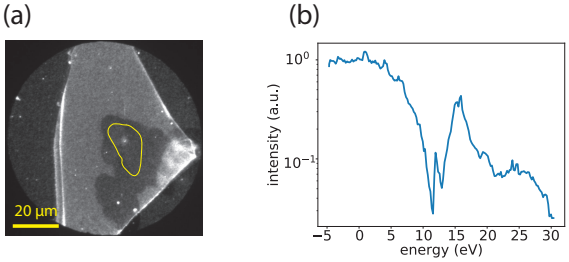

Figure 4.10: Characterization of the hBN flake. (a) PEEM image of the flake. The region of the scanning ARRES measurement is drawn in in yellow. (b) Energy-dependent reflectivity of the same area at the Γ-point, i.e. normal incidence.

set, is shown in figure 4.11 (i) on a logarithmic color scale. The ARRES measurements all share the shape of the mirror mode transition, as seen by the high intensity region at lower energies. The parabolic dispersion of the mirror mode transition around the Γ-point is indicated by the blue line in panel (i).
In the region above the mirror mode to LEEM transition (MTL) the scanning ARRES measurement shows a good degree of similarity over the high symmetry lines (panel (i)) to both the ARRES measurement as referenced in figure 4.2 and the band diagram calculations that are superimposed on that figure. First, the narrow high-reflectance region just above the MTL is present in both plots. Second, the band of states around the Γ-point and 5 eV is present but slightly wider in figure 4.11 (compared to figure 4.2), this corresponds to the calculated band diagram. The pronounced pocket of high reflectance between 10 and 17 eV, finally, is present in both measurements and in the band diagram calculations. Finally, we note that the data in Fig. 4.11 show much more fine structure compared to Fig. 4.2, due to the smaller step size in both E and $\mathbf{k}_{\parallel}$.
Next, we will compare the constant energy cuts to calculations[3]. The constant energy cuts of the reflectance were calculated using an ab initio theory of electron diffraction on a crystal potential computed with the local density approximation (LDA). [32] Further details can be found in ref. [33]. In figure 4.12 we plot a selection of scanning ARRES constant energy cuts (panels (a-e) - not shown in figure 4.11) accompanied by calculated reflectance maps (panels (f-j)). In this comparison the color map was matched, and the plots are individually optimised for contrast. The absolute reflectance values are not matched, i.e. no quantitative conclusions can be drawn from this.
We observe qualitative similarity between theory and experiment. This means that the 3D band diagram information is present in these measurements. There are, however, also some differences. At lower energy the theory and experiment show the best qualitative match (panels(a,b,c) to panels (f,g,h)). The most important difference is the apparent asymmetry between the K and K'-points in the experiment, that is not present in the calculations.

[3]The calculations were performed by E. Krasovskii

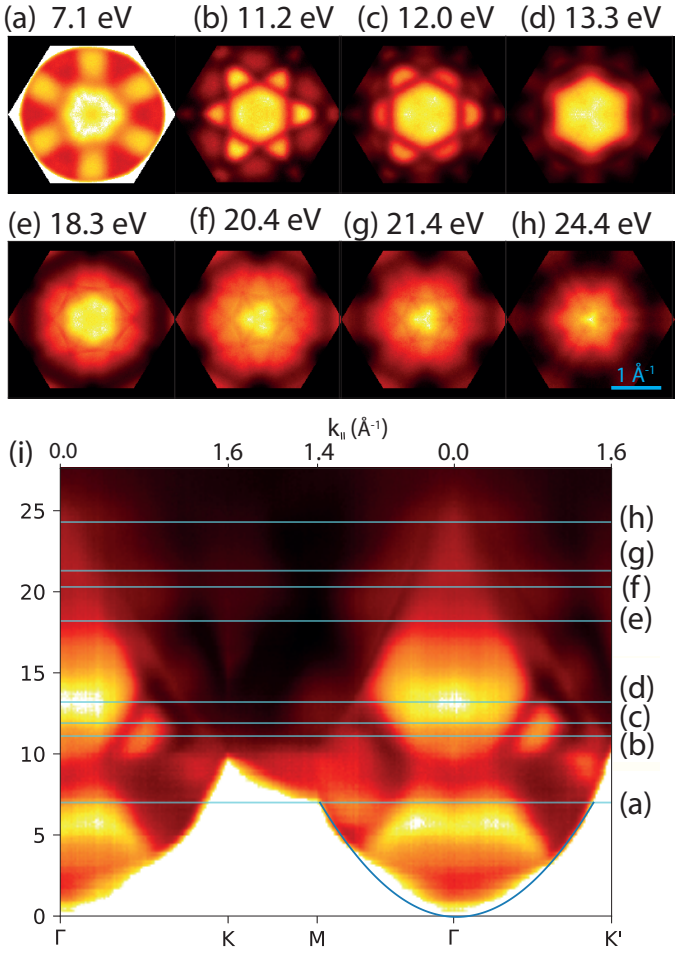

Figure 4.11: scanning ARRES h-BN. (a-h) Selected energy cuts of the reflectance Vs **k** on a linear color scale, landing energy is annotated at the top of the figure. One triangle is measured and copied to the hexagonal symmetry, see figure 4.8). Contrast is optimized for each figure on a linear colour scale. (i) R(E, **k**), over the high symmetry lines on a logarithmic colour scale. Energies for figure (a-h) are indicated by the blue lines.

The asymmetry between the K and K'-points in the measurement could be ascribed to measurement imperfections. At the basis of these measurement issues is a deformation the Leiden LEEM has in the back focal plane, due to alignment imperfections. This deformation causes the Ewald sphere to be less circular at higher energies, and it therefore also deforms the scanned triangle. In order to fit the triangle into the threefold symmetry of the FBZ an affine transformation is used in the post processing. The combination of Ewald sphere deformations and the affine

transformation to solve this can cause the apparent asymmetry. The Ewald sphere deformations will be discussed in the Outlook (Section 4.6).
In conclusion, we have seen a good correspondence between the scanning ARRES

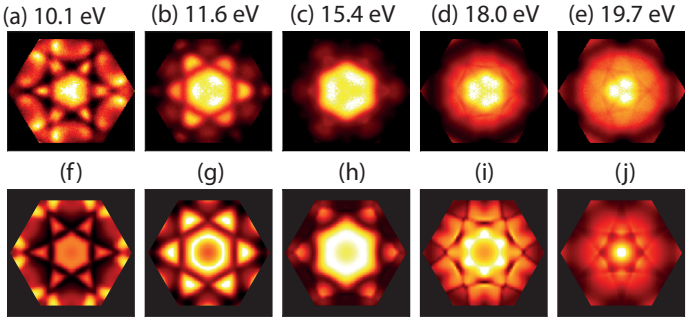

Figure 4.12: Constant energy cuts of hBN. (a-e) scanning ARRES measurements. (f-j) Calculations.

reflectance over the high-symmetry lines and the existing ARRES data. This shows that the significantly faster and higher **k**-resolution scanning ARRES technique can give similar results to ARRES. Moreover, the constant energy cuts give additional band diagram information on the whole (k_x, k_y)-plane.

4.4.2. MoS_2

MoS_2 can have different crystalline phases. In this work we will study the most commonly studied 2H phase. This phase has a hexagonal structure and a lattice constant of 3.2 Å in the in-plane direction.
MoS_2 is widely studied in the 2D-material community for its stability down to the monolayer thickness. It is an indirect bandgap semi-conductor in bulk, and a direct bandgap semiconductor in monolayer form. [34]

Sample characterization

The sample used in this section consists of a doped silicon (100) wafer, topped by many bulk MoS_2 flakes. The MoS_2 flakes were freshly cleaved by tape exfoliation. After exfoliation they were transferred to the silicon wafer, directly from the tape.
Figure 4.13 (a) shows a PEEM overview of the studied flake. In this image the size of the area probed in scanning ARRES is drawn in in yellow. Again the size of this region is larger than the electron beam size, because the change in beam tilt ($\mathbf{k}_\parallel$) induces a displacement of the beam as well. The shape of the region probed was measured by running the scanning ARRES protocol and recording the illuminated area in PEEM.
In figure 4.13 (b) we show the energy-dependent reflectivity of the sample at the Γ-point ($\mathbf{k}_\parallel$ = (0,0) $Å^{-1}$). By comparison with [20] we conclude that the flake consists

of bulk MoS_2. In the next section this first measurement will be expanded to full FBZ spectroscopy.

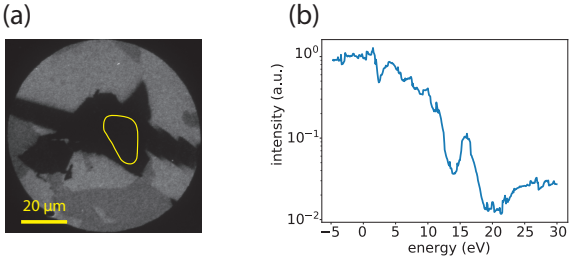

Figure 4.13: Characterization of the MoS_2 flake. (a) PEEM image of the flake. The region of the scanning ARRES measurement is drawn in in yellow. Scale bar is 20 µm. (b) Energy-dependent reflectivity of the same area at the Γ-point on a logarithmic colour scale.

Scanning ARRES

Figure 4.14 presents the scanning ARRES data taken from the MoS_2 flake in figure 4.13. Panels (a-h) present constant energy cuts in which yellow indicates high reflectivity and black represents low reflectivity. The energies for these cuts are indicated by the blue lines in figure 4.14 (i) which shows the ARRES diagram along the high-symmetry axes deduced from the full series of constant energy cut, the minimum and maximum intensity are set separately to optimize contrast.
In figure 4.14 (a) there is a clear reflective halo present on the outer edges of the hexagon. This high reflectivity shows the mirror mode transition at the outer edges of the hexagon. This is described in the previous section.
In some of the constant energy cuts we observe asymmetry between the K and K'-points. Figure 4.15 (a) shows the calculated DoS[4] of MoS_2 over the high-symmetry axes, running from M to Γ to K. In this figure unoccupied states are indicated in yellow and red, absence of states is indicated in white. The reflectance spectra were calculated using an ab initio theory of electron diffraction. [32] Further details can be found in ref. [33]
In figure 4.15 (b) the theory, plotted in panel (a), is super imposed on the reflectance scanning ARRES data from figure 4.14 (i). In the comparison of the theoretical DoS to the scanning ARRES data the following considerations are taken into account.
First, the energy scales need to be matched. The zero-energy of the calculations is defined at the Fermi energy (ε_F), while the zero-energy in LEEM data is defined as the MTL transition at the Γ-point. The difference between these energies is the work function (Φ) of the material ($E_{MTL} = \epsilon_F + \Phi$, with Φ_{MoS_2} =4.6 eV). In panel (a) the calculated MTL transition is indicated by the black dotted parabola. In panel (b)

[4]The calculations were performed by E. Krasovskii

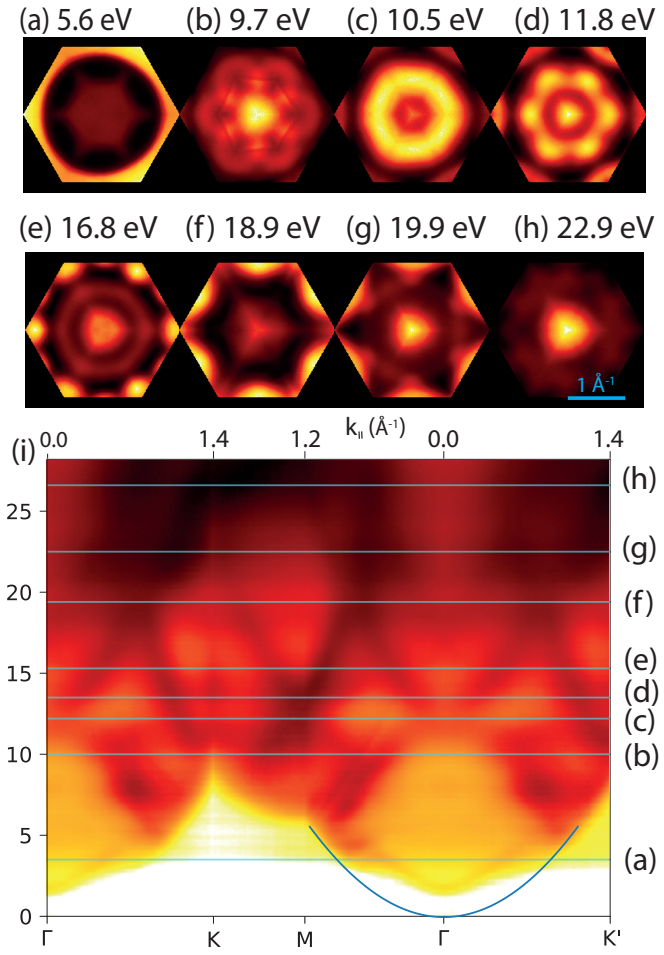

Figure 4.14: scanning ARRES MoS_2. (a-h) Selected energy cuts of the reflectance versus **k** on a linear color scale, landing energy is annotated at the top of the figure. One triangle is measured and copied to the hexagonal symmetry, see figure 4.8. Contrast is optimized for each figure. (i) R(E, **k**) diagram, over the high symmetry lines, reflectivity on a logarithmic scale to emphasize high-energy contrast. Energies for figure (a-h) are indicated by the blue lines. The blue parabola is the predicted mirror mode transition.

the theory is vertically shifted by the appropriate amount.
Second, we will relate the scanning ARRES data to the calculated band diagram. As discussed before, the availability of an unoccupied state for a certain (E, **k**) value is expected to increase the absorptance of the electron into the material. In contrast, in the absence of such a state the electron will be more likely to be reflected.
In figure 4.15 we observe that many of the features in the scanning ARRES plot can be related to features in the band diagram. First, at very low energy, we observe a

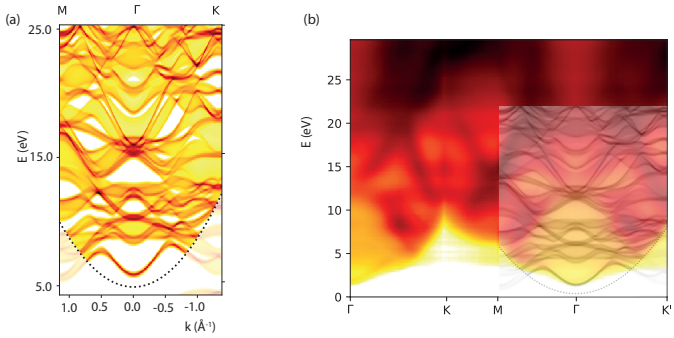

Figure 4.15: MoS_2 scanning ARRES data compared to the calculated band diagram. (a) Calculated density of states (DoS) for MoS_2 over high symmetry axes, running from M to Γ to K. The color scale is inverted for comparison to the experiment: in red/yellow the available unoccupied states are plotted, white is corresponds to the absence of such states. (b) Data as presented in figure 4.14 (i), overlaid with the theoretical DoS as shown in panel (a).

high reflectance region around the Γ-point. This high-reflectance region is related to a bandgap, i.e. an absence of unoccupied states. In the band diagram this region shows a pronounced gap (white in figure 4.15 (a)) in the DoS. Second, just above the white region in the data we observe a dark curved line running between K and M at energies between 0 and 5 eV. This line corresponds to the lowest lying states in the band diagram (red in Figure 4.15 (a)). Third, in the energy range between 3 and 10 eV we observe a large high-reflectance region around the Γ-point with variation of intensity. This region corresponds to a set of gaps and narrow states in the calculation. Finally, the two pockets in the 10-15 eV energy range between the M and Γ-points and the Γ and K-points can be ascribed to corresponding gaps in the band diagram.
To conclude, many features in the MoS_2 scanning ARRES plot over the high symmetry lines can be ascribed to features in the calculated band diagram. Some collections of states are not well resolved, like the ones in the reflective pocket between 3 and 10 eV.

4.5. Conclusions

In conclusion, we have presented a new extension of the ARRES technique: scanning ARRES. This technique is a significantly faster, more complete alternative to ARRES, with a higher resolution in **k** .
The comparison to published ARRES data shows that scanning ARRES gives very similar outcomes compared to regular ARRES, on the high-symmetry axes of the Brillouin zone. As anticipated, the comparison to theoretical band diagrams shows that scanning ARRES probes the unoccupied electronic band structure of the material.
The constant energy cuts show good qualitative similarity to the simulated constant energy cuts. Cuts in electron reflectivity show that scanning ARRES allows one to

measure the three dimensional band diagram of two-dimensional materials, such as MoS_2 and hBN, for energies above the vacuum energy, i.e. for the unstable states of a material.

4.6. Outlook

In this outlook, we will first present recommendations to improve the spatial resolution of the scanning ARRES technique. This has a high priority as it will enable this technique for a wider variety of samples. Second, we will discuss the deformations in the back focal plane at higher energies. Finally we will discuss the applicability of these measurements to ARPES data interpretation.

In this chapter we have presented a technique that outperforms conventional ARRES on two major fronts: acquisition speed and **k**-resolution. However, in real-space resolution conventional real-space ARRES is, and will be, superior. This means that the two techniques will both be complementary parts of the standard measurement catalogue in the future.

The spatial resolution of scanning ARRES is a major point of concern, as it puts a strong requirement on the size of the sample and the homogeneity of the sample over at least 20 μm^2.

As seen in figures 4.10 (a) and 4.13 (a) the area scanned is larger, i.e. worse, than the beam size. The reason for this is that a change in incident angle of the beam, also induces a (small) change in the location of the beam. Because this change in location is predictable it is possible to correct for this unwanted movement in the real-space plane by compensating for it with the real-space deflector. This compensation is routinely done in the measurement software. However, for the fast-scanning set-up as presented in this chapter, the compensation needs to be driven at the same high frequencies as the k-plane deflector. The compensation can be realized by adding an additional VI-converted to operate the real-space deflector. This step would reduce the scanned area to the beam size diameter.

For an even smaller area probed, a real-space aperture could be used in the coupled set-up. This could reduce the resolution to the size of the smallest aperture available in the system (200 nm, after magnification at the image, in the Leiden set-up).

The deformations in the back focal plane of the Leiden LEEM setup give rise to apparent K-K' asymmetries in the constant energy cuts, as seen in figure 4.11 and 4.14. For hBN the theoretical constant energy cuts give no reason to expect these asymmetries. For MoS_2 we also observe a certain degree of asymmetry, for some energies. The nature of the unit cell can give rise to such an asymmetry. However, due to the experimental uncertainty at the edges of the Ewald sphere, it is currently not possible to conclude either way.

The relevance of (scanning)ARRES should not be found in direct predictions for

transport experiments, as the probed energy range lies far too high. However, the part of the band diagram probed is useful to improve ARPES analysis.
In ARPES analysis one needs to assume a final, excited state [4]. This is the (unstable) state to which the electron is promoted after photon absorption, before it is finally emitted into vacuum. This state, higher in energy, is in the energy range scanning ARRES probes and the states that are measured by the ARRES technique. As we have shown in this chapter the three-dimensional band diagram above the vacuum energy is efficiently measured with scanning ARRES. These measurements could thus be used to refine ARPES data interpretation in the future.

References

[1] G. S. Painter and D. E. Ellis, *Electronic band structure and optical properties of graphite from a variational approach,* Physical Review B **1**, 4747 (1970).

[2] Y. F. Tsay, D. K. Paul, and S. S. Mitra, *Electronic structure and optical properties of amorphous Ge and Si,* Physical Review B **8**, 2827 (1973).

[3] L. Zhang, P. Bampoulis, A. N. Rudenko, Q. Yao, A. Van Houselt, B. Poelsema, M. I. Katsnelson, and H. J. Zandvliet, *Structural and Electronic Properties of Germanene on MoS2,* Physical Review Letters **116**, 1 (2016), arXiv:1706.00680 .

[4] A. Damascelli, *Probing the Electronic Structure of Complex Systems by ARPES,* Physica Scripta **T109**, 61 (2004), arXiv:0307085 [cond-mat] .

[5] H. E. Romero, N. Shen, P. Joshi, H. R. Gutierrez, S. A. Tadigadapa, J. O. Sofo, and P. C. Eklund, *n-type behavior of graphene supported on Si/SiO2 substrates,* ACS Nano **2**, 2037 (2008).

[6] H. J. Zandvliet and A. van Houselt, *Scanning Tunneling Spectroscopy,* Annual Review of Analytical Chemistry **2**, 37 (2009).

[7] H. M. Hill, A. F. Rigosi, K. T. Rim, G. W. Flynn, and T. F. Heinz, *Band Alignment in MoS2/WS2 Transition Metal Dichalcogenide Heterostructures Probed by Scanning Tunneling Microscopy and Spectroscopy,* Nano Letters **16**, 4831 (2016).

[8] L. Petersen, P. Sprunger, P. Hofmann, E. Lægsgaard, B. Briner, M. Doering, H.-P. Rust, A. Bradshaw, F. Besenbacher, and E. Plummer, *Direct imaging of the two-dimensional fermi contour: Fourier-transform stm,* Physical Review B **57**, R6858 (1998).

[9] H. Murata and A. Koma, *Modulated stm images of ultrathin (formula presented) films grown on (formula presented)(0001) studied by stm/sts,* Physical Review B - Condensed Matter and Materials Physics **59**, 10327 (1999).

[10] M. Crommie, C. Lutz, and D. Eigler, *Imaging standing waves in a two-dimensional electron gas,* Nature **363**, 524 (1993).

[11] J. E. Hoffman, *A Search for Alternative Electronic Order in the High Temperature Superconductor $Bi_2Sr_2CaCu_2O_{8+\delta}$ by Scanning Tunnelling Microscopy,* (2001).

[12] G. Binnig, K. Frank, H. Fuchs, N. Garcia, B. Reihl, H. Rohrer, F. Salvan, and A. Williams, *Tunneling spectroscopy and inverse photoemission: image and field states,* Scanning Tunneling Microscopy , 93 (1985).

[13] M. Sentef, M. Claassen, A. Kemper, B. Moritz, T. Oka, J. Freericks, and T. Devereaux, *Theory of floquet band formation and local pseudospin textures in pump-probe photoemission of graphene,* Nature communications **6**, 7047 (2015).

[14] C. L. Smallwood, C. Jozwiak, W. Zhang, and A. Lanzara, *An ultrafast angle-resolved photoemission apparatus for measuring complex materials,* Review of Scientific Instruments **83**, 123904 (2012).

[15] J. Kautz, *Low-Energy Electron Microscopy on Two-Dimensional Systems: Growth , Potentiometry and band structure mapping* (2015).

[16] J. Jobst, A. J. Van Der Torren, E. E. Krasovskii, J. Balgley, C. R. Dean, R. M. Tromp, and S. J. Van Der Molen, *Quantifying electronic band interactions in van der Waals materials using angle-resolved reflected-electron spectroscopy,* Nature Communications **7**, 1 (2016).

[17] I. Bartos, *ELECTRONIC STRUCTURE OF CRYSTALS,* **0**, 197 (1998).

[18] E. E. Krasovskii, W. Schattke, V. N. Strocov, and R. Claessen, *Unoccupied band structure of (formula presented) by very low-energy electron diffraction: Experiment and theory,* Physical Review B - Condensed Matter and Materials Physics **66**, 1 (2002), arXiv:0207607 [cond-mat] .

[19] T. A. De Jong, E. E. Krasovskii, C. Ott, R. M. Tromp, S. J. Van Der Molen, and J. Jobst, *Intrinsic stacking domains in graphene on silicon carbide: A pathway for intercalation,* Physical Review Materials **2**, 1 (2018), arXiv:1807.04185 .

[20] T. A. de Jong, J. Jobst, H. Yoo, E. E. Krasovskii, P. Kim, and S. J. van der Molen, *Measuring the Local Twist Angle and Layer Arrangement in Van der Waals Heterostructures,* Physica Status Solidi (B) Basic Research **255**, 1 (2018), arXiv:1806.05155 .

[21] R. M. Tromp, J. B. Hannon, A. W. Ellis, W. Wan, A. Berghaus, and O. Schaff, *A new aberration-corrected, energy-filtered LEEM/PEEM instrument. I. Principles and design,* Ultramicroscopy **110**, 852 (2010).

[22] W. Wang, M. Brien, D. Gu, and J. Yang, *A comprehensive study on current source circuits,* in *13th International Conference on Electrical Bioimpedance and the 8th Conference on Electrical Impedance Tomography* (Springer, 2007) pp. 213–216.

[23] J. F. McClain, J. Sun, K. Pohl, and J.-M. Tang, *First-principles theory of low-energy electron diffraction and quantum interference in few-layer graphene,* arXiv preprint arXiv:1311.2917 (2013).

[24] R. M. Feenstra, N. Srivastava, Q. Gao, M. Widom, B. Diaconescu, T. Ohta, G. L. Kellogg, J. T. Robinson, and I. V. Vlassiouk, *Low-energy electron reflectivity from graphene,* Physical Review B - Condensed Matter and Materials Physics **87**, 1 (2013).

[25] D. Pacíl, J. C. Meyer, Ç. Girit, and A. Zettl, *The two-dimensional phase of boron nitride: Few-atomic-layer sheets and suspended membranes,* Applied Physics Letters **92**, 1 (2008).

[26] K. Watanabe, T. Taniguchi, and H. Kanda, *Direct-bandgap properties and evidence for ultraviolet lasing of hexagonal boron nitride single crystal,* Nature Materials **3**, 404 (2004).

[27] C. R. Dean, A. F. Young, I. Meric, C. Lee, L. Wang, S. Sorgenfrei, K. Watanabe, T. Taniguchi, P. Kim, K. L. Shepard, and J. Hone, *Boron nitride substrates for high-quality graphene electronics,* Nature Nanotechnology **5**, 722 (2010), arXiv:1005.4917 .

[28] S. K. Jang, J. Youn, Y. J. Song, and S. Lee, *Synthesis and Characterization of Hexagonal Boron Nitride as a Gate Dielectric,* Scientific Reports **6**, 1 (2016).

[29] A. Castellanos-Gomez, M. Buscema, R. Molenaar, V. Singh, L. Janssen, H. S. Van Der Zant, and G. A. Steele, *Deterministic transfer of two-dimensional materials by all-dry viscoelastic stamping,* 2D Materials **1**, 011002 (2014).

[30] F. Pizzocchero, L. Gammelgaard, B. S. Jessen, J. M. Caridad, L. Wang, J. Hone, P. Bøggild, and T. J. Booth, *The hot pick-up technique for batch assembly of van der waals heterostructures,* Nature communications **7**, 11894 (2016).

[31] J. Jobst, J. Kautz, D. Geelen, R. M. Tromp, and S. J. Van Der Molen, *Nanoscale measurements of unoccupied band dispersion in few-layer graphene,* Nature Communications **6**, 1 (2015).

[32] J. I. Flege and E. E. Krasovskii, *Intensity–voltage low-energy electron microscopy for functional materials characterization,* physica status solidi (RRL)–Rapid Research Letters **8**, 463 (2014).

[33] T. A. de Jong, J. Jobst, H. Yoo, E. E. Krasovskii, P. Kim, and S. J. van der Molen, *Measuring the local twist angle and layer arrangement in van der waals heterostructures,* physica status solidi (b) **255**, 1800191 (2018).

[34] K. F. Mak, C. Lee, J. Hone, J. Shan, and T. F. Heinz, *Atomically thin MoS2: A new direct-gap semiconductor,* Physical Review Letters **105**, 2 (2010), arXiv:1004.0546 .

5

High-electron mobilities in ionic-liquid gated PbSe perculative superlattices

Parts of this chapter have been published in V.A.E.C. Janssen, *et al.* "Transport properties of a two-dimensional PbSe square superstructure in an electrolyte-gated transistor." Nano letters 17.9 (2017): 5238-5243.

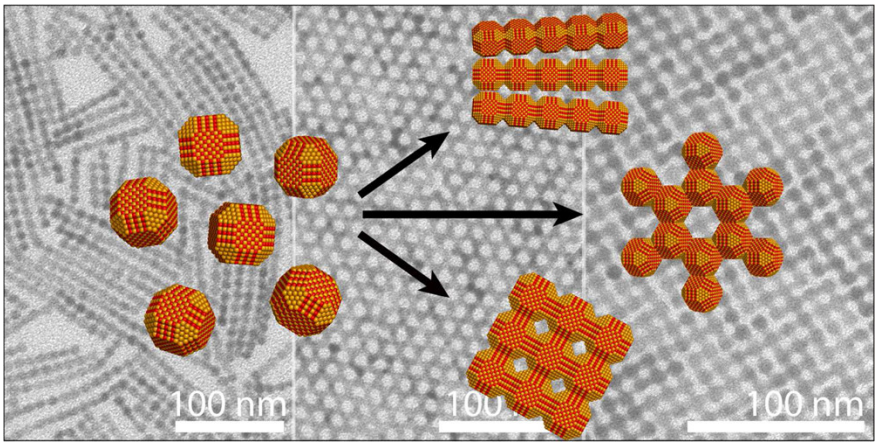

Figure 5.1: Transmission Electron Microscope images of different nano-crystal superstructures. From left to right: linear shaped superlattice, honeycomb lattice and a percolative lattice. Overlay shows a model of the trucated cube shaped nanocrystals in red (Se) and yellow (Pb). The attachment facet dictates the shape of the lattice. Figure taken from reference [6].

5.1. Introduction

The isolation of graphene [1] caused an extraordinary stream of ideas on exotic new effects and new states of matter. Many of these theoretical ideas were followed up by experimental realization. [2, 3] However, some of these proposals were blocked from realization by fundamental properties of the two-dimensional carbon lattice. Two missing features of graphene are of special importance. First, there is the absence of a bandgap, hindering the use of graphene in semiconductor applications. Second, graphene has a small spin-orbit coupling (SOC). The combination of the honeycomb structure with a strong spin-orbit coupling could enable the observation of new topological states of matter, like the quantum spin Hall effect. [4]
Inspired by graphene, novel materials are being developed, incorporating the two-dimensional honeycomb lattice but also adding the missing ingredients described above. One class of novel materials is superlattices consisting of PbS(e), CdS(e) or HgTe nano-crystals (NCs). These materials as artificially synthesized in a bottom-up way, in which the nano-crystals are the building blocks of a two-dimensional lattice. [5, 6]
The building blocks are crystalline nano-objects with a truncated cube shape and a size of 5 nm. The crystalinity and high degree of control over shape and size results in objects with very well-defined facets. The truncated cubes can be forced to attach covalently on certain facets, forming an atomic single crystaline material with a coherent superlattice structure over tens of microns as depicted in Fig. 5.1. [6]
The nano-crystal composition defines the electronic properties of the resulting solid, because it induces an additional degree of electronic confinement. The single layer of crystals obviously confines electrons in the z-direction, similar to, but over a large scale than in graphene. Additionally, the interconnected nanocrystal lat-

tice confines electrons in the in-plane directions. This confinement creates a large band gap dictated by the nano crystal size, similar to confinement seen in colloidal quantum dots. Both the shape of the lattice and the materials used to form them influence the rich band structure of these materials. Inspired by graphene, CdSe honeycomb lattices are predicted to host Dirac carriers. Combining the structure of graphene with the strong spin-orbit coupling of heavy metals could host the quantum spin Hall effect. [4]

In this chapter we present some first steps in the electrical characterization of PbSe square superlattices. This material was chosen because of its availibility and because of the ambipolar behaviour of PbSe on the doping scale we could reach. Moreover, the PbSe lattice can be transformed to a CdSe lattice, keeping the structural integrity of the superlattice, by performing a cation-exchange. [7] First we contact the sheets in a micron-sized four-terminal device structure. In this architecture the material mobility (μ) and square conductance ($\sigma_{\square}$) can be obtained. These figures of merit are first rough indications for the transport mechanism involved in the material. The small size of the devices enable measurements over homogenous pieces of superlattice. It is of vital importance to overcome the large bandgap created by the large confinement energies present in the quantum dots. In order to reach this objective we have tuned the Fermi-level in the samples by means of an ionic-liquid gate.

5.2. Ionic-liquid gate

The need for an ionic-liquid gate Conventional semi-conductor research and industry is based on using solid state back- or top gates for control over the carrier density. Solid-state field-effect transistors consist of a semiconductor channel insulated from the conducting gate with a dielectric layer. Usually the gate consist of a doped sillicon gate, combined with a thermally grown SiO_2 dielectric layer. [8] This has the advantage of easy thermal growth and clean homogenous layers. The gate architecture can be can be thought of as a parallel plate capacitor, where the accumulated charge (Q) is given by:

$$Q = CV, \tag{5.1}$$

where C is the capacitance and V the operating voltage. The capacitance is equal to:

$$C = \frac{\epsilon_0 \epsilon_r A}{d}, \tag{5.2}$$

where ϵ_0 is the vacuum permittivity, ϵ_r the dielectric constant of the gate dielectric (3.9 for SiO_2), A the area of the channel and d the thickness of the gate dielectric. If one wants to maximize the accumulated charge in the sample for a given operating gate voltage, one should optimize the capacitance in the architecture. Two mayor routes have been taken to do this.

The first way to achieve a higher capacitance is by minimizing d i.e., by using thinner dielectric layers. This has the disadvantage that thinner layers have a lower break down voltage. Moreover, in very thin insulators one can expect a leakage current due to electron tunnelling through the insulating layer. So this route leads mostly to devices with lower operating voltages, which is beneficial for industrial purposes, but the maximum carrier density cannot be increased much.
The second route in device fabrication has been more fruitful: using dielectrics with a high dielectric constant (ϵ_r). [9] These *high k dielectrics* have advangtages in decreasing operating voltages of MOSFETs and can induce large amounts of carriers in the channel. [10] For example: using hafnium dioxide (HfO_2) with an $\epsilon_r = 25$ the maximum carrier density obtained is of the order of $n = 10^{13}\mathrm{cm}^{-2}$. [11]
To go even higher in carrier density something new is needed. Recently there has been a lot of progress in the use of ionic liquids in an ionic-liquid gate geometry. [12–15] This architecture brings ions in a liquid state in direct contact with the semi-conducting channel. This will dramatically decrease d leading to a significant increase in carrier density, as we will see in the next part.

5

5.2.1. Working principle

An ionic liquid gate is a method to reach and modulate very high carrier densities in solid-state samples. The geometry can be decribed as follows: the channel is covered in an ionic liquid or ion-containing liquid. This liquid is also in contact with a gating electrode, as shown in Fig. 5.2. By applying a potential difference between the substrate and the gate electrode, ions will migrate acccording to their polarity. This will result in the accumulation of a majority of ions of one polarity at the gate electrode, and an accumulation of ions of the other polarity on the sample. [16]
The effectiveness of this method lies in the very close proximity of ions to the channel and with this, a very small value of d can be achieved. The ions are in direct contact with the sample and will attract charge carriers; forming an electric double layer (EDL). This principle is shown in Fig. 5.3 (b). The two opposing polarities of ions form layers on the surfaces. The bulk of the electrolyte is uncharged and has a very large electrical resistance, this resistance avoids a current from running through the electrolyte. The potential drop in this system is drawn in Fig. 5.3 (a). The electric double layer can be seen as a nano scale capacitor. The distance between the capacitor plates is now of the order of a nanometer. This very significantly improves the capacitance, leading to considerably larger carrier densities.
Recently, this novel gating method has opened the very high carrier density part of parameter space for two-dimensional Van der Waals materials. This has resulted in a wave of new observations in these materials, ranging from ambi-polar transistor behaviour to superconductivity. [17, 18]

Numbers and limits It has been shown that with an ionic-liquid gate one can induce a carrier density of about $10^{14}\mathrm{cm}^{-2}$. [12] This number exceeds the charge

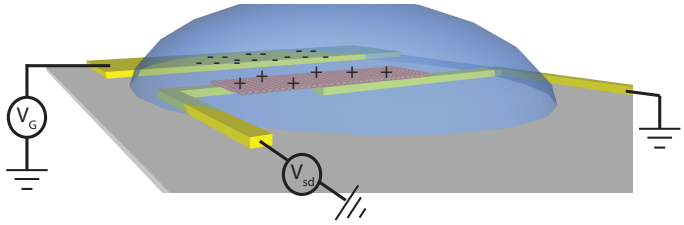

Figure 5.2: Cartoon of the operation principle of a ionic-liquid gate. The sample (orange) is contacted by source and drain electrodes (yellow). The gate pad (yellow) is not in direct contact with the sample. Both the sample and the gate pad are in contact with an ionic liquid. In this case a positive voltage is applied to the gate pad ($V_G > 0$). This induces the negatively charged ions (-) to migrate to the gate pad and the positively charge ions (+) migrate to the sample.

density of a conventional Si-SiO_2 MOSFET by two orders of magnitude. The typical operating voltages used are of the order of one volt. The operating voltage is limited by electro-chemical reactions which start to take place at higher voltages.

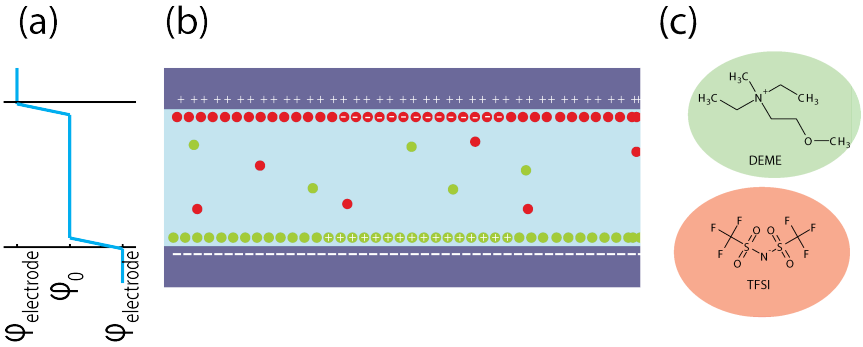

Figure 5.3: (a) Cartoon of the potential drops in an EDL. The two potential drops span only over a few nanometers, the bulk of the ionic liquid is neutral. (b) Cartoon of the formation of an electric double layer. On the upper electrode (purple) a positive gate voltage is applied. This positive charge organizes the negatively charged ions (red spheres) to migrate to the electrode surface. On the bottom the purple rectangle depicts the substrate. The positively charged ions (green spheres) form a layer, attracting electrons in the substrate. (c) Chemical structure of the two ions in DEME-TFSI.

5.2.2. Choise of electrolyte

There is a large variety of ionic liquids and ion containing gels on the market. For an ionic liquid gate one needs good ion mobility (for fast operation of the transistor) and a high electrical resistance (to avoid leakage currents through the electrolyte). For operation in a vacuum setup also a low vapour pressure is needed.
For the transport measurements we used (N,N-diethyl-N-(2-methoxyethyl)- N -methylammonium bis(trifluoromethylsulphonylimide) (DEME(+)-TFSI(-)), an organic molten salt with a structure as depicted in figure 5.3 (c). This liquid has a very low

vapor pressure and is therefore compatible with low pressure and low temperature measurements. The melting point of this compound is around T = 220 K, which means that at room-temperature we can sweep the gate, but at low temperature the ions are frozen. This keeps the electric field on the sample constant below the melting point.

5.3. Fabrication and sample preparation

Superlattice synthesis [1] The superlattices are synthesized by self-assembly of a monolayer on the toluene/air interface. After the self-assembly process, the nanocrystals attach to each other via their four vertical $\{100\}$ facets. The mechanisms involved in these processes have been reported recently [19]. After the oriented attachment the superlattice was annealed at 80°C for 20 minutes. A part of such a monolayer sheet is shown in Fig. 5.4 (a). The absorption spectrum of such a single layer is presented in Fig. 5.4 (b). It can be seen that the absorption peak shows a red shift and a broadening compared to PbSe NCs in suspension. The red shift is due to polarization effects. The peak broadening is caused by the quantum mechanical coupling between the NCs in the superlattice. [20]
Figure 5.4 (c) shows the band structure obtained from a tight binding (TB) calculation. The calculated absorption spectrum, depicted in Fig. 5.4 (d) shows a first peak related to the coupling of the S-type envelope functions and a second peak corresponding to the coupling of the P-type envelope functions. The experimental absorption spectrum shows a similar peak at 0.7 eV. This peak can thus be related to the valence-to-conduction band transitions involving the band resulting from coupling of the S-type envelope functions. It is important to note that the S-bands in Fig. 5.4 (b) are 8-fold degenerate.
The 2D PbSe NC monolayer superstructure (see Fig. 5.4 (a)) is scooped from the ethylene glycol substrate and is put on top of pre-patterned electrodes by gentle horizontal contact approaching with the device from above. The quality and uniformity of the superlattice sheet is checked by visual inspection. In order to enable a relation between the electrical transport properties and the atomic structure of the superlattice, a part of the sample under investigation was put on a transmission electron microscope (TEM) grid for structural characterization.

Chip fabrication Figure 5.5 (a) shows the geometry of the chips used. The substrate is a silicon wafer with a 285 nm thermally grown SiO_2 layer on top (gray). In the first e-beam step the leads, contacts and the gate pad (6000 μm x 500 μm) are patterned (all depicted in red). The window in the middle of Fig. 5.5 (a) of the chip is where the Hall-bar devices are situated, Fig. 5.5 (c) shows a picture of such a device.
To avoid contacting issues caused by large steps between the wafer and the elec-

[1] The synthesis of all material described in this chapter and the next was performed by W.H. Evers.

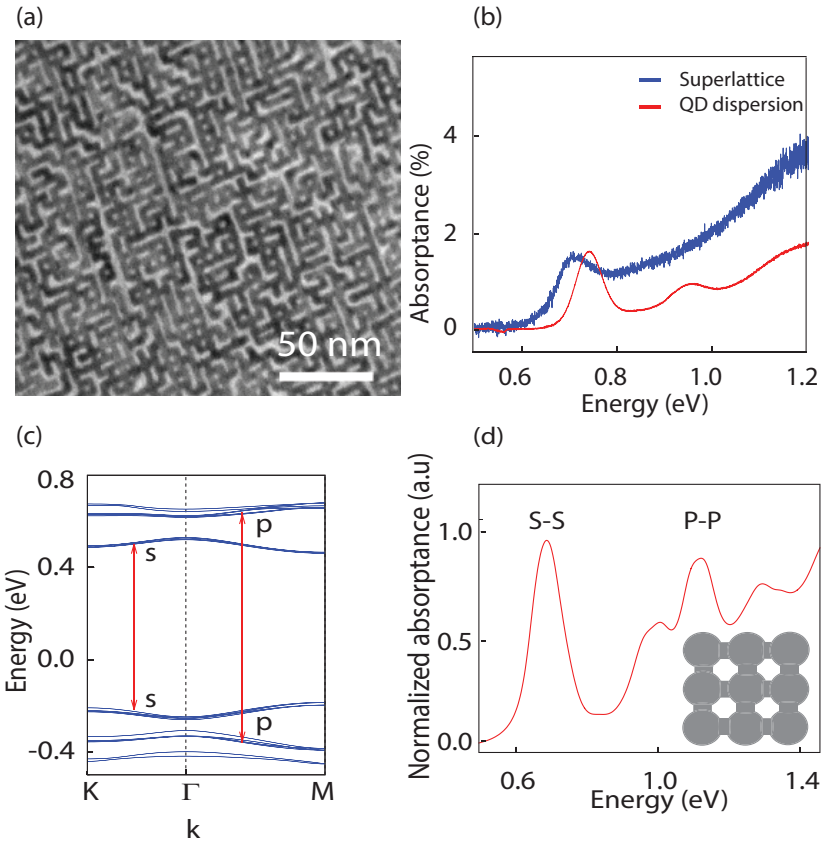

Figure 5.4: (a) Transmission electron microscope image of a part of a PbSe square lattice (monolayer) prepared by self assembly and oriented attachment at 80° C; the scale bar measures 50 nm. (b) Absorption spectrum of a monolayer of a square PbSe superlattice annealed at 80°C. The red curve shows the absorption of a suspension of nanocrystals as a reference. (c) Tight-binding band structure for a square superlattice, from [21]. The S-S and P-P valence-to-conduction band optical transitions are indicated with arrows and these lead to the first two absorption features in Fig (d). (d) Calculated tight-binding absorption spectrum for a square PbSe superlattice. Inset: geometry used for the calculation. The nanocrystals are modeled as spheres with a diameter of 5.5 nm. The spheres are connected by cylinders of 2.2 nm in length. Calculation performed by E. Kalesaki.

trodes we keep the height of the devices to a minimum. First 5 nm Ti and 20 nm Au is deposited by e-beam evaporation. Subsequently, the area on the chip where the devices are situated (window in the middle of the chip in Fig 5.5 (a)) is masked to avoid further gold deposition. The rest of the chip (leads, gate and contacting pads) undergoes an additional e-beam evaporation step, in which an additional 60 nm of Au is deposited. This results in a 5 nm Ti topped by a 80 nm Au layer in total. The devices are shaped in a Hall-bar geometry with a source-drain distance of 5 μm and length of 25 μm, the probes are spaced 2 μm apart and have an overlap with the source-drain electrodes of 8 μm.

To avoid parallel currents through the superlattice, we shield the leads by a thin (50 nm) insulating layer. For this a second e-beam step is performed. The insulating layer consist of Al_2O_3 grown by atomic layer deposition (ALD). This Al_2O_3 layer caps the Au leads from the superlattice, which is deposited later, where contact is undesired.

After completing the electrode fabrication, the chips are transferred to a nitrogen glove box. The superlattice is deposited by first scooping the film from the glycol ethylene liquid surface and concurrently bringing it gentle verticle contact with the chip. The chip is annealed at T = 80°C to form a percolative lattice with well developed necking between the crystals.

Finally the devices are covered in the ionic liquid (DEME-TFSI) electrolyte and capped with a thin glass slide. The glass slide serves to avoid oxygen and water contamination during the samples brief stay in air between transportation from the glove box to the vacuum set up.

Figure 5.6 shows a tilted scanning electron microscope (SEM) image of a nanocrystal superlattice sheet draped over a two-terminal device. The two gold contacts run horizontally across the image. The dark gray areas are the superlattice monolayer. The light gray area's are micron-scaled defects in the film. The picture of a different sample in Fig. 5.5 (c) shows qualitatively similar cracks. These types of micron sized defects are observed in all samples. To avoid influence on the measurements, all used devices were subject to an optical inspection. Only devices with a homogenous film in the active area were selected for measurements. SEM inspection was not compatible with transport measurements, as direct exposure to air would be unavoidable during transfer to the SEM.

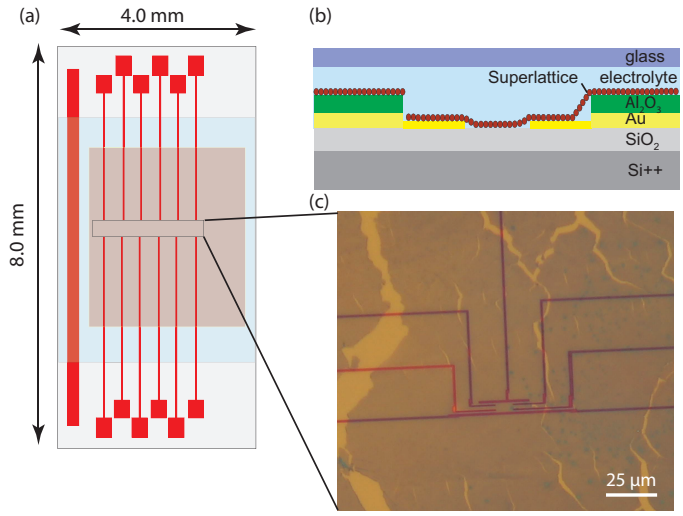

Figure 5.5: (a) Schematic of the chip designed for four-probe measurements on the superstructures. On a standard Si-SiO_2 wafer, Au leads and a gating pad (red) are defined by e-beam lithography, superstructure (opaque red) is deposited on the leads and the electrolyte (blue) is deposited and capped with a glass slid. (b) Cross section of the final sample. (c) Optical picture of a typical device.

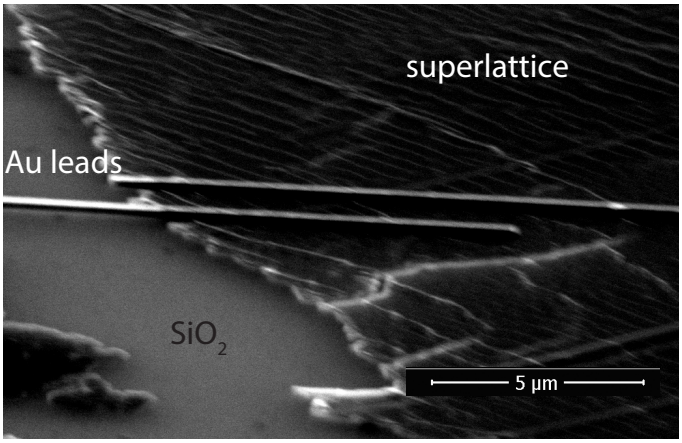

Figure 5.6: Tilted SEM image of a two-terminal device capped by a monolayer NC sheet. The two gold leads run horizontally over the middle over the image. The NC assembly shows in dark, with additional lighter structure. Absense of the NC sheet shows in gray. Sample not used for transport measurements.

5.4. Determination of the electron density [2]

The shift in Fermi-level on changing the gate voltage is not known a priori. Therefore, we first determine the carrier density of the system when applying a voltage to the liquid gate by means of an optical bleaching experiment. For liquid gated systems, the gate response is reported to be of the order of 1eV/V for flat two-dimensional materials. [15, 22]
A change in the Fermi-level of the nanocrystal-assembly changes the optical absorbence and the conductance properties; we will use this feature to estimate the carrier density as a function of applied gate voltage. Fig. 5.7 shows a cartoon of this experiment. For simplicity only single quantum dots are depicted, the general argument holds for the assembly when we translate the energy levels to the envelope bands in the assembly. In Fig 5.7 (a) we start with the Fermi-level in the bandgap between the valence and conduction bands. This is where the optical absorptance spectrum is defined as zero. When the dots are irradiated with light containing the wavelengths matching the energy transitions between the highest valence level and the first two conductance levels (S- and P-levels) these wavelengths are absorbed, resulting in the promotion of carriers to these levels. When shifting the Fermi-level, i.e. setting a potential to the liquid gate, the S- and P-levels progressively fill up (see Fig. 5.7 (b) and (c)). This will change the absorbance spectrum, as the wavelengths previously absorbed will be reflected.

Figure 5.8 (a) shows the absorption difference at different values of the applied

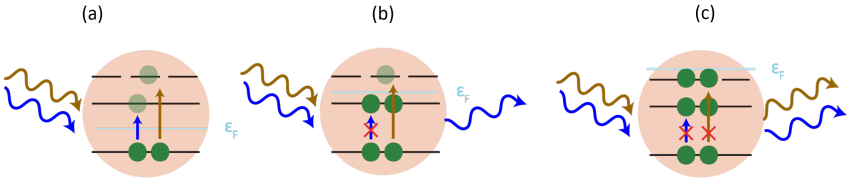

Figure 5.7: Cartoon of the optical bleaching experiment. The red circles depict the nanocrystals, the black lines are the energy levels present in the nanocrystals, the blue line shows the shifting Fermi level and the blue and brown undulating arrows depict light of different wavelengths matching the energy differences between the energy levels of the NCs (arrows of same colours). (a) The Fermi level is in the band gap between the valence and conduction levels. Light of wavelengths matching the energy difference between the levels is absorbed and electrons are promoted from the valence level to the higher S- and P-levels. (b) Fermi-level is inbetween the S- and P-levels. The S-level is filled, disallowing the light induced promotion of carriers to this level. (c) Fermi-level is shifted to above the P-levels. Now both absorbance transitions are forbidden.

potential (indicated in the right panel of Fig 5.8 (a)), for two cyclic potential scans. Zero absorption is defined at potential point zero. The second cycle almost reproduces the absorption features of the first cycle. This demonstrates that the electrons can be reversibly injected into and extracted from the superlattice. Figure 5.8 (b) shows the absorption spectrum for different gate values at energies corresponding

[2]The optical bleaching measurements in this section were performed by W.H. Evers, the TB bleaching spectrum in this section was calculated by E. Kalesaki.

to the low-energy bleach feature in Fig 5.8 (a). At potentials more negative than V_G = -1.22 V (here vs. a Ag reference electrode), absorption quenching sets in, first at a low photon energy between 0.55 eV and 0.8 eV related to the $1S_h1S_e$ transition. With more negative potentials (V_G = -1.46 V to -1.69 V), the quenching obtains more weight and also extends to higher photon energies. At even more negative potentials, absorption quenching saturates in the energy region between 0.55 eV - 0.8 eV. This is illustrated by the inset graph in Figure 5.4 (b) where we plot the relative absorptance against applied potential for both S-S and P-P transitions. We observe that this relative absorpance becomes equal to 1 at a potential of V_G = -1.53 V for the S-S transition. Concomitantly, the absorption quenching in the range 0.8 eV to 1.2 eV becomes gradually more important with more negative gate potentials. This feature can be related to the $1P_h1P_e$ transition.

The gradual increase and saturation of the bleach feature can be understood by a progressive filling of the 8-fold degenerate S-type conduction band and partial occupation of the P-band, due to thermal activation at T = 300 K. The band structure for a 2-D PbSe square superlattice has been calculated by Kalesaki et al. [4]. The resulting quenching spectrum upon electron occupation of the S-bands with 1 to 8 electrons is presented in Figure 5.4 (c). It can be seen that the main features of the absorption quenching i.e., the gradual shift of the quenching peak to higher energies, the saturation at the low-energy side, and the upcoming quenching of the P-P transition at more negative potentials are all well captured by the calculations. From these optical bleaching experiments we can conclude that by means of a liquid gating method we can populate both the S- and P-bands in the assemblies. The shift in Fermi-level when applying a voltage to the gate (gate response) can now be estimated by comparing the optical population of the S- and P-levels to the band diagram in Fig. 5.4. This results in a gate coupling of around 0.9 eV/V .

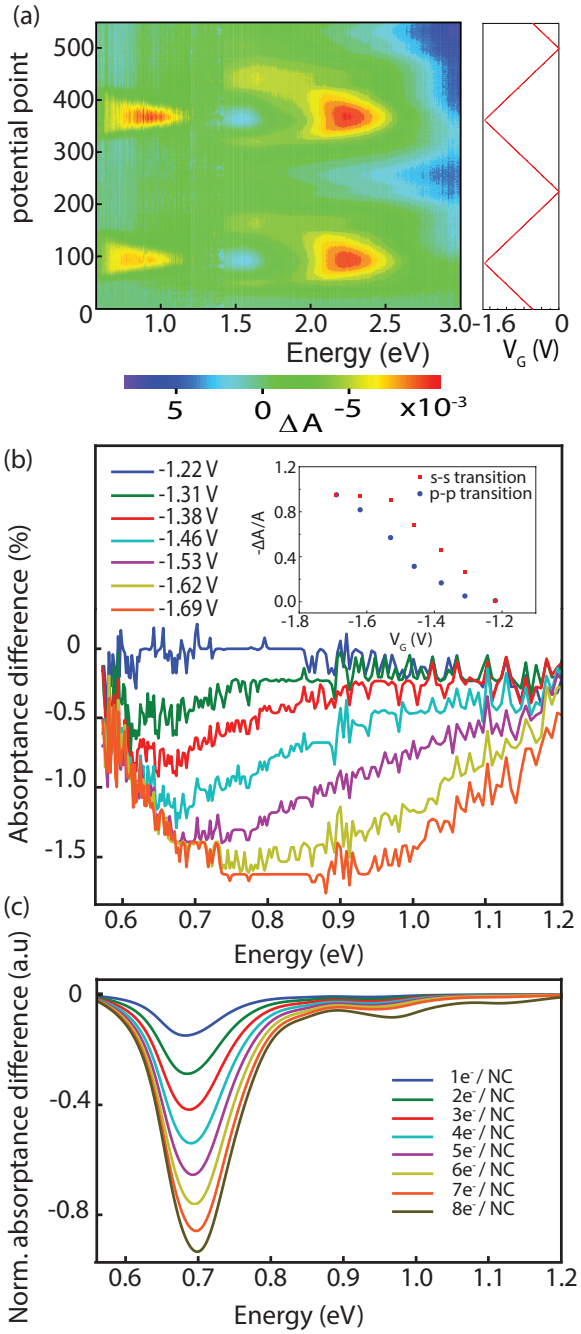

Figure 5.8: (a) Changes in the absorbtance on sweeping the gate twice between V_G = 0 V and V_G = -1.6 V. (b) The absorption quenching measured at increasingly negative potentials; electron injection starts at V_G = -1.22 V (dark blue curve) which can be taken as a reference. With more negative potentials, the quenching initially becomes more dominant at low-photon energy and extends to the high-energy range for the most negative potentials applied. Inset: relative absorbtance for S-S and P-P transitions at different applied potential. (c) Tight-binding calculation of the absorption quenching on the basis of the band structure presented in figure 1(b).

5.5. Room-temperature transport measurements

In this section we present the transport measurements performed on 13 different Hall-bar devices (as descibed in section 5.3) spread over five samples from different synthesis batches. For the interpretation of the data we utilize the information on the carrier density as deduced from the optical bleaching experiments (Section 5.4). It is important to note that the sign of the gate voltage (V_G) has flipped as compared to Section 5.4. The reason for this is an inconsistency in convention between the two fields over which this chapter spans. The convention in the bleaching experiments is to define the potential of the sample by means of a potentiostat. In the following sections we define V_G as the voltage set to the gate pad.

5.5.1. Two probe transfer characteristics

First we measure the conductance properties over the inner contacts of the Hall-bar geometry. The two-probe IV curves are measured by setting the voltage (-10 mV to 10 mV) between the two inner probes of a device and measuring the current. Fig. 5.9 (a) presents the ambi-polar transfer characteristics of a representative sample. The figure shows a gate sweep of the current for positive- (green) zero- (blue) and negative (red) bias of 10 mV. Both the forward- and backward sweep of the gate voltage are recorded. The reversibility of the operation of the electric double layer transistor, as seen from only a small hysteresis, ensures that the signal is due to transistor behaviour of the semiconductor and not due to electrochemical reactions on the surface. Moreover, the zero-bias sweep indicates that the leakage through the gate is neglectable for these measurements.
At V_G = 1.2 V, the conduction of the sample increases, for both negative- and positive bias, so here we can identify an electron conduction channel. At gate values lower than V_G = 0.3 V the conductance increases as well, as can be seen in the inset of Fig. 5.9 (a) which presents a zoom-in of the negative gate voltage regime. The linear IV's of the same sample in both conduction channels are shown in Fig. 5.9 (c) and (d) indicate ohmic contact to the nanocrystal arrays. Here, again, the forward- and backward sweeps are recorded. The absense of hysteresis in the IV-curves indicates that the liquid gate is in a fully relaxed state i.e., there is no contribution of ion migration in the measured current, during the full IV. The conductance reaches 25 MΩ in the hole channel at V_G = -0.4 V and a value of 250 kΩ at V_G = 2.0 V in the electron channel. The conductance in the electron channel is two orders of magnitude higher and we will focus on this regieme.
The ambipolar behaviour is seen in most devices. The strong increase in conductance in the electron channel is used as a selection criterion for the presented samples. Table 5.1 shows the two-probe resistances, as calculated from the slope of the IV at V_G = 2.0 V. As can be seen, the two-probe resistance varies over a large range among the different samples.
Figure 5.9 (b) shows the same data as in Fig. 5.9 (a) on a logarithmic scale. The ambipolar operation of the electrolyte gated transistor enables us to relate the insulating gap between V_G = 1.2 V and 0.3 V to the band gap of the PbSe superlattice.

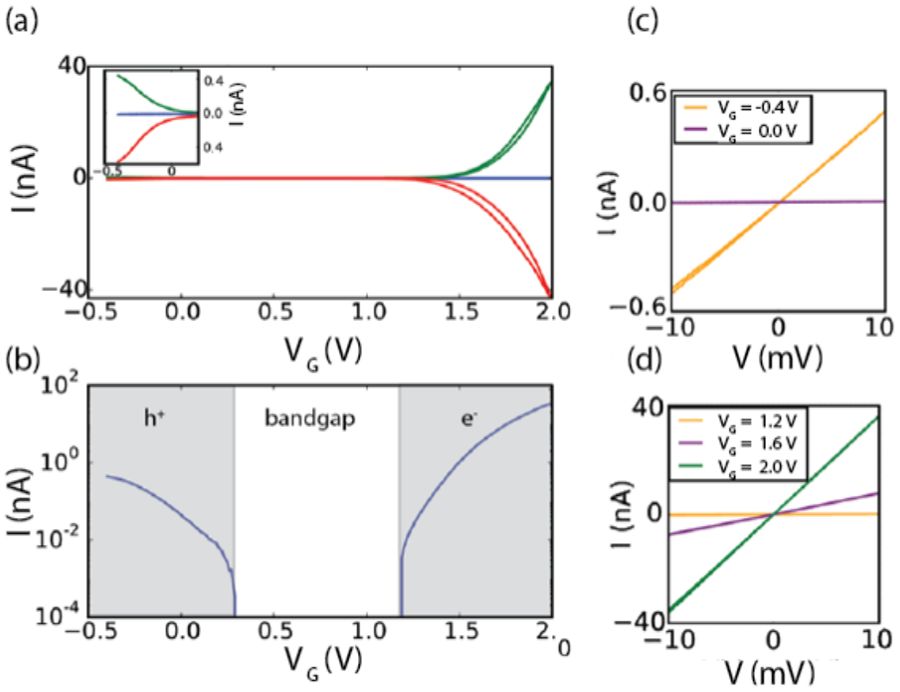

Figure 5.9: (a) Two-probe transfer curves for negative (red), zero (blue) and positive (green) bias. The inset shows a zoom-in of the negative gate region where the hole channel is visible. (b) The same data as in figure (a) but plotted on a log scale. The insulating region is due to the band-gap of the PbSe superlattice. (c) IV-curves for negative gate voltages (hole conduction). (d) IV curves at positive gate values (electron conduction).

However, to obtain the single-particle gap, it has to be corrected for the gate efficiency. The gate voltage needed to overcome the bandgap of 0.7 eV, as deduced from the optical measurements, is about 0.9 V. Assuming a linear response of the carrier density to the gate voltage, i.e. efficient screening and small charging energies, a gate coupling of 0.7 eV/0.9 V = 0.8 eV/V is calculated. This is consistent with the results for the gate coupling from the optical measurements as discussed in the section above (of 0.9 eV/V).

5.5.2. Four-probe measurements and contact resistance

To investigate the effect of the contact resistance four-probe conductance measurements have been performed. A current was applied to the outer contacts of the Hallbar geometry and the voltage on the inner contacts (2 µm by 8 µm) was measured. A typical gate sweep over the electron conduction channel is shown in

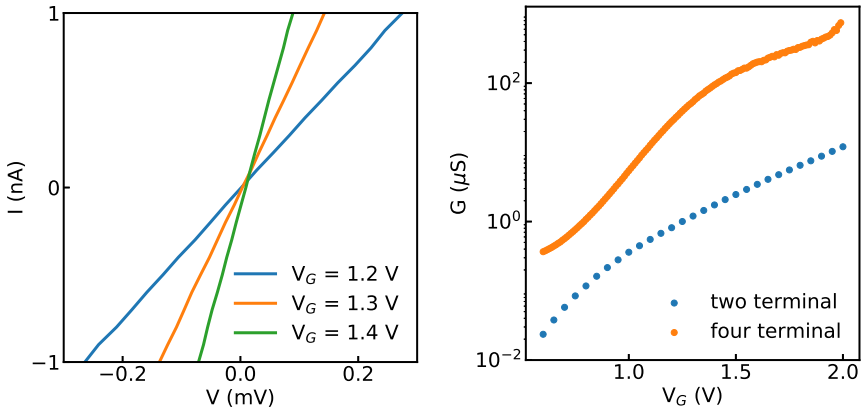

Figure 5.10: Four-teminal transfer characteristics. (a) Four-terminal IV-curves. (b) Four-terminal transfer characteristics (orange) in the electron channel. For comparison the two-terminal transfer characteristic (blue) is plotted as well.

figure 5.10 (b). Just as in the two-probe measurements the opening of the electron channel can be observed as a as a strong increase of conductance. Fig. 5.10 (b) shows the linear IV curves of the same sample in the electron channel.
Now we can estimate the contact resistance (R_c) from the difference between the two-teminal and four-terminal measurements:

$$R_c = \frac{1}{2}(R_{2p} - R_{4p}). \tag{5.3}$$

We found that the contact resistance at varies from device to device, and dominates in all devices with values ranging between 300 kΩ to 30 MΩ, as presented in Table 5.1.
From the four-probe measurements the resistivity ($\rho_\square$) is calculated. To calculate the resistivity per square we normalize to the device dimensions (L x W = 2 x 8 μm^2). Here we assume the devices to be entirely covered by the nanocrystal assembly, which is validated by the optical inspection as described in the fabrication section. The resistivity ($\rho_\square$) is given by:

$$\rho_\square = \frac{L}{W}R, \tag{5.4}$$

where W is the width of the channel i.e., the length of the electrodes (8 μm), L is the length of the channel i.e., the spacing between the electrodes (2 μm) and R is the measured resistance.
Table 5.1 summarizes the resistivity calculated for 13 devices on five different substrates. The resistivity values are calculated from the linear IV curves at $\mathrm{V_G} = 2.0\mathrm{V}$.

5.5.3. Carrier mobility

For both, the two-probe and four-probe measurements we can estimate the mobility (μ) of our samples using:

$$\mu = \frac{ne}{\rho}, \tag{5.5}$$

where e is the electron charge, ρ is the conductance per square and n the carrier density. For the estimation of the carrier density (n) we use the optical experiments performed in the section above. In these experiments we observed a bleach in the s-bands (two e^- / dot) and in the triply degenerate p-bands (addition of maximum of 3x2 e^-/dot). This gives an upper bound of 8 electrons per nanocrystal at a gate value of $V_G = 2.0V$. We estimate the nanocrystal density from TEM images to be 2.86×10^{12} nanocrystals per cm^2. Therefore, we can estimate the carrier density at $V_G = 2.0V$ to be $n_e = 2.29 \times 10^{13}$ cm^{-2}. As described in Section 5.2 an ionic-liquid gate can be used to reach reported carrier densities of $n = 10^{14} cm^{-2}$ in two-dimensional van der Waals materials, typically ate higher gate voltages. So the carrier densiy we reach in these experiments is reasonable.
The mobility is calculated for all samples and is presented in Table 1. The two-probe mobility varies between 0.02 and 1 cm^2/Vs. The four probe mobility gives a range of values between 1 and 18 cm^2/Vs .

	$R_{2p}(k\Omega)$	$\rho_{4p}(k\Omega/\square)$	$\mu_{2p}(cm^2/Vs)$ $8e^-$ at $V_G = 2.0V$	$\mu_{4p}(cm^2/Vs)$ $8e^-$ at $V_G = 2.0V$
sample A				
device 1	1342	104.8	0.20	2.6
sample B				
device 1	120.3	197	0.57	1.37
device 2	66.7	248	1.0	1.1
device 3	374.2	71.2	0.18	4.01
device 4	333.3	140.0	0.82	2.13
sample C				
device 1	3300	200.0	0.02	1.4
device 2	2500	112.0	0.03	2.4
device 3	-	40	-	6.8
sample D				
device 1	40.0	15.2	1.7	18
sample E				
device 1	217.6	121.9	0.3	2.2
device 2	358.7	105.0	0.2	2.6
device 3	228.8	187.9	0.3	1.4
device 4	474.0	287.0	0.1	0.9

Table 5.1: Two- and four probe resistances and the corresponding mobilities for 13 Hall-bar devices spread over five different samples. Resistances measured at a gate voltage of 2.0 V.

From the combined results from all samples we can conclude that the contact resistance limits the two-probe mobility i.e., the actual mobility of the material is higher than deduced from typical two-probe measurements.

References

[1] A. C. Neto, F. Guinea, N. M. Peres, K. S. Novoselov, and A. K. Geim, *The electronic properties of graphene,* Reviews of modern physics **81**, 109 (2009).

[2] Y. Zhang, Y.-W. Tan, H. L. Stormer, and P. Kim, *Experimental observation of the quantum Hall effect and Berry's phase in graphene,* Nature **438**, 201 (2005).

[3] K. S. Novoselov, Z. Jiang, Y. Zhang, S. Morozov, H. L. Stormer, U. Zeitler, J. Maan, G. Boebinger, P. Kim, and A. K. Geim, *Room-temperature quantum Hall effect in graphene,* Science **315**, 1379 (2007).

[4] E. Kalesaki, C. Delerue, C. M. Smith, W. Beugeling, G. Allan, and D. Vanmaekelbergh, *Dirac cones, topological edge states, and nontrivial flat bands in two-dimensional semiconductors with a honeycomb nanogeometry,* Physical review X **4**, 011010 (2014).

[5] C. Schliehe, B. H. Juarez, M. Pelletier, S. Jander, D. Greshnykh, M. Nagel, A. Meyer, S. Foerster, A. Kornowski, C. Klinke, *et al.*, *Ultrathin PbS sheets by two-dimensional oriented attachment,* Science **329**, 550 (2010).

[6] W. H. Evers, B. Goris, S. Bals, M. Casavola, J. de Graaf, R. van Roij, M. Dijkstra, and D. Vanmaekelbergh, *Low-dimensional semiconductor superlattices formed by geometric control over nanocrystal attachment,* Nano letters **13**, 2317 (2012).

[7] M. P. Boneschanscher, W. H. Evers, J. J. Geuchies, T. Altantzis, B. Goris, F. T. Rabouw, S. Van Rossum, H. S. van der Zant, L. D. Siebbeles, G. Van Tendeloo, *et al.*, *Long-range orientation and atomic attachment of nanocrystals in 2D honeycomb superlattices,* Science **344**, 1377 (2014).

[8] B. E. Deal and A. Grove, *General relationship for the thermal oxidation of silicon,* Journal of Applied Physics **36**, 3770 (1965).

[9] A. I. Kingon, J.-P. Maria, and S. Streiffer, *Alternative dielectrics to silicon dioxide for memory and logic devices,* Nature **406**, 1032 (2000).

[10] G. He and Z. Sun, *High-k Gate Dielectrics for CMOS Technology*, Engineering-Pro collection (Wiley, 2012).

[11] B. Radisavljevic and A. Kis, *Mobility engineering and a metal-insulator transition in monolayer MoS_2.* Nature Materials **12** (2013).

[12] J. Ye, S. Inoue, K. Kobayashi, Y. Kasahara, H. Yuan, H. Shimotani, and Y. Iwasa, *Liquid-gated interface superconductivity on an atomically flat film,* Nature materials **9**, 125 (2010).

[13] J. Ye, Y. Zhang, R. Akashi, M. Bahramy, R. Arita, and Y. Iwasa, *Superconducting dome in a gate-tuned band insulator,* Science **338**, 1193 (2012).

[14] J. Pu, Y. Yomogida, K.-K. Liu, L.-J. Li, Y. Iwasa, and T. Takenobu, *Highly flexible MoS_2 thin-film transistors with ion gel dielectrics,* Nano letters **12**, 4013 (2012).

[15] D. Braga, I. Gutierrez Lezama, H. Berger, and A. F. Morpurgo, *Quantitative determination of the band gap of WS_2 with ambipolar ionic liquid-gated transistors,* Nano letters **12**, 5218 (2012).

[16] H. Du, X. Lin, Z. Xu, and D. Chu, *Electric double-layer transistors: a review of recent progress,* Journal of materials science **50**, 5641 (2015).

[17] Y. Zhang, J. Ye, Y. Matsuhashi, and Y. Iwasa, *Ambipolar MoS_2 thin flake transistors,* Nano letters **12**, 1136 (2012).

[18] Y. Saito, Y. Nakamura, M. S. Bahramy, Y. Kohama, J. Ye, Y. Kasahara, Y. Nakagawa, M. Onga, M. Tokunaga, T. Nojima, *et al.*, *Superconductivity protected by spin-valley locking in ion-gated MoS_2,* Nature Physics **12**, 144 (2016).

[19] J. J. Geuchies, C. Van Overbeek, W. H. Evers, B. Goris, A. De Backer, A. P. Gantapara, F. T. Rabouw, J. Hilhorst, J. L. Peters, O. Konovalov, *et al.*, *In situ study of the formation mechanism of two-dimensional superlattices from PbSe nanocrystals,* Nature materials **15**, 1248 (2016).

[20] C. S. S. Sandeep, J. M. Azpiroz, W. H. Evers, S. C. Boehme, I. Moreels, S. Kinge, L. D. A. Siebbeles, I. Infante, and A. J. Houtepen, *Epitaxially connected PbSe quantum-dot films: Controlled neck formation and optoelectronic properties,* ACS Nano **8**, 11499 (2014), pMID: 25347299.

[21] E. Kalesaki, W. Evers, G. Allan, D. Vanmaekelbergh, and C. Delerue, *Electronic structure of atomically coherent square semiconductor superlattices with dimensionality below two,* Physical Review B **88**, 115431 (2013).

[22] J. Ye, M. F. Craciun, M. Koshino, S. Russo, S. Inoue, H. Yuan, H. Shimotani, A. F. Morpurgo, and Y. Iwasa, *Accessing the transport properties of graphene and its multilayers at high carrier density,* Proceedings of the National Academy of Sciences **108**, 13002 (2011).

6

Low-temperature transport in a two-dimensional superstructure

6.1. Introduction

Achieving the formation of conduction bands in artificial solids proofs to be a demanding endeavour. First of all, the building blocks, i.e., the PbSe nanocrystals, consist of hundreds or thousands of atoms. As opposed to single atoms, these nano-scale objects are haunted by a certain degree of imperfection. [1] The second challenge is to assemble thousands of these nano-objects into an ordered lattice, closely enough packed to allow for hybridization of their wave functions. Finally, and mostly for two dimensional assemblies, the (electrostatic) environment can be another source of disorder, leading to localization of charge carriers. The central question for nanocrystal self-assemblies is whether the level of disorder can be small enough to lead to a metallic state, in other words to a decrease of the assembly resistance when the temperature is lowered. A temperature dependent study of the electronic properties is indispensable information in this direction.
In Sec. 6.2 of this chapter first the hopping frame work will be reviewed, as hopping transport models are commonly used to describe temperature activated transport in disordered media. Next, the possibility of a metal-to-insulator transition in quantum dot solids is discussed, followed by the adaptations needed to reach a metallic state in two-dimensional electron systems. Section 6.2 concludes with a brief discussion on previously reported metallic behaviour in quantum dot solids. Section 6.3 covers the experimental results of the low-temperature study on the PbSe superlattice devices. After presenting the experimental techniques, the data sets at a ionic-liquid gate voltage of 2.0 V are presented and are fitted to hopping models. Finally the data at different gate voltages are presented. Section 6.4 discusses the most important deviations of the presently presented data and literature, and possible reasons for this deviation. This Chapter is concluded with Sec. 6.5.

6.2. Hopping and the transition to band-like transport

In this section the typical transport mechanisms observed in disordered materials will be outlined. First the family of hopping models will be discussed. In these models carriers are localized in a disordered potential landscape. This localization leads to temperature activated transport, which manifests itself in strongly temperature dependent conduction properties. Next, focus will be turned to quantum dot solids and the phenomenology of the formation of conduction bands in these systems. Because the samples presented in this chapter consist of only a monolayer of nanocrystals, also the metal to insulator transition in two dimensions is discussed. Finally, a brief summary of metallic transport behaviour observed in three-dimensional glass-like quantum dot films is presented.

6.2.1. Theoretical work on hopping transport

The conductance in many semiconducting nanoparticle assemblies can be described by a family of hopping models. All these models describe localized charge carriers in a disordered potential landscape. The conductance is non-zero because, at finite temperature, carriers can hop from one state to another. Hopping is an off-resonant tunnelling process, in which a charge carrier that is localized in a state below the Fermi energy (E_F) takes energy from a phonon and "hops" to a nearby empty state. As the temperature decreases, phonons become more scarce and the hopping probability decreases, causing the resistance to increase.
Hopping transport does not limit itself to nano-crystal supperlattices; it has been observed in many different systems, such as disordered semiconductors, molecular crystals and quantum dot solids. [2, 3] These systems have in common that disorder prevents energy bands from forming, leading to an insulating state at low temperature. The broad relevance of this problem has led to a rich field of study, both experimentally and theoretically.

Nearest neighbour hopping (NNH)

Nearest neighbour hopping was the first model proposed to explain the behavior of doped semiconductors. [4] In these materials impurities are present and cause localization of carriers; however, the density of these impurities is not high enough to form impurity bands. The localization can be described by a density of states (DoS) consisting of quantized energy levels. Furthermore, there is variation in the height of the energy levels, due to random local potentials. This variation in energy is assumed to be large enough to prevent conduction bands to form, leading to localization of charge carriers. In this model *Miller and Abrahams* [4] reasoned that a carrier under the Fermi energy could move to the next unoccupied state by emission ($E_n > E_{n+1}$) or absorption ($E_n < E_{n+1}$) of a phonon. The hopping rate

between two nearest neighbour sites is then described by:

$$\nu = \begin{cases} \nu_0 e^{-\gamma r} e^{-\frac{\Delta E}{k_B T}}, & \text{if } \Delta E > 0 \\ 1, & \text{if } \Delta E \leq 0 \end{cases} \tag{6.1}$$

where ν_0 is the attempt frequency, γ is the inverse localization radius of the sites, r the distance between neighbouring sites and ΔE the energy difference between neighbouring sites. In Eq. 6.1 the attempts going down in energy are always successful. The rate for events that go up in energy is the product of two exponential functions with a normalization constant (ν_0). The first exponent describes the fall off of the probability with distance. This typical hopping distance is assumed a constant in this model. The second exponent describes the fall off with increasing energy distance. The energy difference between neighbouring sites is allowed to vary. This model is visualized in figure 6.1, where the spread in height depicts the energy level spread. The energy taken from the system to go up in energy is assumed to come from phonons and the rate is therefore temperature dependent. This transfer frequency maps to a resistivity per square (in a two-dimensional system) as a function of temperature:

$$\rho_{\square} = \rho_0 e^{\frac{E_{a,A}}{k_b T}}, \tag{6.2}$$

where ρ_0 is the pre-factor dependent on the height of the tunnelling barriers between the sites, and $E_{a,A}$ is the NNH activation energy, given by: $E_{a,A} = \frac{k_B e^2}{32\pi r^2 \epsilon \epsilon_0}$, where e is the electron charge, r the nearest neighbour distance, ϵ the material dielectric constant and ϵ_0 the vacuum permittivity.

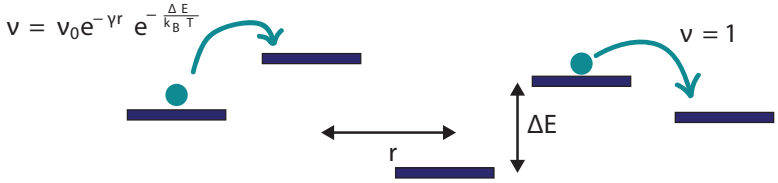

Figure 6.1: Cartoon of the nearest neighbour hopping model. The energy levels have a spread in height (energy) and are a distance r apart. Electrons can only move to an adjacent site.

Variable range hopping (VRH)

For a disordered system at very low temperatures hopping does not necessarily occour from a given site to its nearest neighbor. Mott [5] showed that the most favourable hopping event could be one over a longer distance, if there is some spread in energy levels. The optimization of the easiest path is not exclusively defined by the distance between sites. As the thermal energy ($k_B T$) decreases

Figure 6.2: Cartoon of the VRH model. Here the electron does not need to move to the next nearest site, but may optimize the hopping distance r for a minimal ΔE.

and passes the order of the magnitude of the energy spread of the levels (ΔE) the energy alignment between sites becomes an important factor.
To calculate the resistance, we start from the same hopping rate as before, given in equation 6.1. The hopping probability for $\Delta E > 0$ is given by:

$$\mathrm{P} \propto e^{-\gamma r - \frac{\Delta E}{k_B T}}, \tag{6.3}$$

where r now is a parameter that needs to be optimized. This probability contains both, a penalty for tunnelling over large distances ($e^{-r\gamma}$) and a penalty for tunnelling over large energy differences ($e^{-\frac{\Delta E}{k_B T}}$). The model assumes the energy spread to be $\Delta E = \frac{3}{4\pi} r^3 N(E_F)$ for the thee-dimensional case, with $N(E_F)$ the density of states (DoS) around the Fermi energy. We can now maximize the hopping probability for r, by calculating $\frac{dP}{dr}$. This yield a optimal hopping distance of

$$r = [\frac{1}{8}\pi N(E_F)\alpha k_B T]^{1/4}. \tag{6.4}$$

The resistivity in the Mott variable range hopping (M-VRH) model is of the form:

$$\rho = \rho_0 e^{BT^{-\nu}}, \tag{6.5}$$

where ν depends on the dimensionality of the system (d) as $\nu = \frac{1}{d+1}$. B is given by: $B = 2(\frac{3}{2\pi})^{1/4}(\frac{\alpha^3}{k_B N(E_F)})^{1/4}$. For a two-dimensional system we find for the resistivity per square:

$$\rho_\square = \rho_0 e^{(\frac{E_{a,M}}{k_B T})^{1/3}}, \tag{6.6}$$

with $E_{a,M} \propto \frac{1}{k_B g_0 a^2}$.
The next step in complexity in this VRH framework is to include electron-electron interactions. This was first calculated by *Efros and Shklovskii*. [6] The Coulomb interactions between the electrons will modify the density of states, by forming a gap near the Fermi level. In the two-dimensional case this leads to the following DoS:

$$g(\epsilon) = \alpha \frac{|\epsilon|\kappa^2}{e^4}, \tag{6.7}$$

where α is a coefficient, ϵ the energy distance from the Fermi level and κ the dielectric constant of the material.
We can now plug this DoS into equation 6.4 and obtain the temperature dependence of the resistivity for VRH-ES:

$$\rho = \rho_0 e^{(\frac{E_{a,ES}}{k_B T})^{1/2}}, \tag{6.8}$$

where $E_{a,ES} \propto \frac{e^2}{\kappa a}$. This formula is independent of dimensionality.
The above description holds for the low-bias regime, i.e., in the Ohmic part of the current-voltage characteristic. At higher bias the electric field ($\mathrm{E} > \frac{2\mathrm{k_B T}}{ea}$) will become the dominating contributor to the activation of the transport. [7, 8] For field-assisted hopping the resistivity becomes temperature independent and follows:

$$\rho(E) \propto e^{(\frac{E_0}{E})^{1/2}}, \tag{6.9}$$

where $E_0 = E_{a,ES}/2ea$.

6.2.2. The transition to band-like transport

Quantum dot solids (QD solids)

In the previous part the QD energy levels were modelled as non-interacting, quantized energy states. The hopping framework derived from these assumptions only works well for amorphous solids and quantum dot solids if the energy levels are spaced such that the individual wave functions do not overlap. This changes dramatically if the dots are brought in very close proximity and the wave functions do interact.
When the spacing (r) between the energy sites i.e., QD's, in a solid is reduced such that the wave functions overlap ($r < \frac{1}{\mathrm{k_F}}$, where k_F is the Fermi wavevector) interaction between the wave functions will enable the formation of conduction bands. Figure 6.3 illustrates this transition; when the wave functions overlap, the Pauli exclusion principle demands hybridization of the energy levels. This leads to the formation of conductions bands, in analogue to the formation of a band structure in a lattice of atoms.
For temperature dependent transport properties the formation of conduction bands will have striking consequences. As explained in Section 6.2.1 hopping transport is a temperature activated process. As the temperature decreases, less and less energy is available for hopping events resulting in an increasing resistance. In the case of band-type transport there are no energy barriers to overcome. This will lead to a decreasing resistance at lower temperatures because the limiting scattering mechanism, the interaction with phonons, will decrease on cooling. Concluding, from the temperature dependent transport characteristics a criterion for the transport mechanism can be deduced: if $\frac{\mathrm{d}\rho}{\mathrm{dT}} > 0$, transport is temperature activated, if $\frac{\mathrm{d}\rho}{\mathrm{dT}} < 0$, the formation of conduction bands in the system has been established.

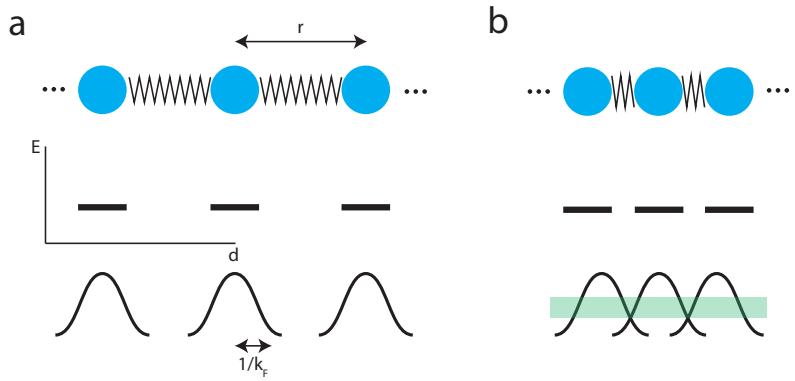

Figure 6.3: Cartoon of the transition from (a) insulating quantized energy states to (b) the formation of conduction bands in quantum dot solids, where E is the energy, d the distance between dots and k_F the Fermi vector. Quantum dots are depicted as blue circles; the spacers (organic or inorganic) are shown as zig-zag lines. If the spacing between the dots is small enough ($1/k_F > r$) energy bands (green) will form.

Metallic transport in two dimensions

Two-dimensional electron systems have long been believed to never show a metallic state at low temperatures. [9] The theoretical argument for this was that the confinement of electrons in one of the spatial directions would always cause weak localization. This weak localization stems from disorder, no matter how small. Scattering centres will cause localization because the electron will destructively interfere with its own time-reversal path at low temperature. At higher temperature a metallic state is possible, due to *inelastic* scattering with phonons that breaks the symmetry between time-reversed paths. More recent work, however, has shown experimental proof for the existance of a metallic state in two-dimensional electron systems down to the lowest temperatures. The first systems to show this were silicon samples with a low degree of disorder. [10, 11]
In contradiction to the historic paradigm, two-dimensional materials typically show a metal to insulator transition (MIT) if the level of disorder is small enough to be overcome by doping. [12] The two dimensional MIT typically follows the Ioffe-Regel criterion [13], which states that for a metallic state to arise, the mean free path (l) of the carriers should be larger than the reciprocal of the Fermi wavelength ($\frac{1}{k_F}$):

$$\begin{aligned} l < \frac{1}{k_F} \quad &: \quad \frac{d\rho}{dT} < 0 \quad \text{(insulator)} \\ l > \frac{1}{k_F} \quad &: \quad \frac{d\rho}{dT} > 0 \quad \text{(metal)} \end{aligned} \tag{6.10}$$

where l is the mean free path and n is the number of carriers. For the conductivity we have: $\sigma = \frac{ne^2\tau}{m^*}$ and the mean free path is given by: $l = \tau\frac{\hbar k_F}{m}$ and the Fermi wave vector in 2D is: $k_F = (4\pi n/\mathrm{g_s g_v})^{1/2}$, where $\mathrm{g_s}$ and $\mathrm{g_v}$ are the spin and valley degeneracy, respectively. From these definitions the following critical resistivity (ρ_c) follows, for a given carrier density, below which a two dimensional material is expected to behave as a metal:

$$\rho_\mathrm{c} = \frac{2}{\mathrm{g_s g_v}}\frac{h}{e^2}, \tag{6.11}$$

where $\frac{h}{e^2}$ is the quantum of resistance. In two-dimensional systems the resistivity is usually expressed as a resistivity per square ($\rho_\square$ or ρ_{2D}).

6.2.3. Previous experimental work on QD solids

Traditionally, QD solids are synthesized by surrounding single dots or nanocrystals by organic ligands. The dots are brought in contact, so that they assemble into a superstructure bridged by ligands. [14–17] These ligands are typically long molecules to ensure stability of the nanocrystals in suspension. The length of the ligands directly determines the interdot spacing.

By exchanging the long ligands for shorter organic or inorganic spacers the coupling between the dots can be increased. Up to date, reports on short-organic spaced solids do not show signs of extended electronic states. Thin films show low mobilities ($\mu < 1\ \mathrm{cm^2/Vs}$) in combination with temperature activated transport behaviour. [8, 18–20] The use of inorganic ligands proves to be a more successfull route. Reports show band-type transport ($\frac{\mathrm{d}\rho}{\mathrm{dT}} > 0$) in concurrence with high room-temperature mobilities ($\mu > 1\ \mathrm{cm^2/Vs}$) for assemblies of closely packed QDs capped with inorganic spacers. [21–23]

Table 6.1 summarizes the reports on metallic behaviour in QD thin films. These reports have in common that the extended electronic states are found in QD assemblies with very small inorganic spacers. Another remarkable similarity is the relatively high mobility values at room temperature, in the order of 10 $\mathrm{cm^2/Vs}$. High mobility values can thus be used as an indicator for band-like transport in glass-like QD films. It should also be noted that the films do not consist of quantum dot monolayers and that metallic-like behaviour is only found in a limited temperature range below room temperature.

	$\frac{d\rho}{dT}$	$\mu_{RT}(cm^2/Vs)$	T-scale (K)	materials
Lee *et al.* [21] (2011)	> 0	10-16	220 - 340	CdSe (3.9 nm) $In_2Se_4^{2-}$ capped
Choi *et al.* [22] (2012)	> 0	27	140 - 300	CdSe (3.9 nm), ammonium thiocyanate capped
	< 0		77 - 140	
Oh *et al.* [23] (2014)	> 0	7	200-300	PbSe (6 nm) capped with SCN and $PbCl_2$ passivated
	< 0		< 200	

Table 6.1: Summary of previous reports on metallic behaviour in QD solids. μ_{RT} is the reported room-temperature mobility.

6.3. Low-temperature transport

In this section the low-temperature transport data will be presented. First the samples will be introduced and their room-temperature mobility and square resistance are summarized. Next the preparation- and measurement procedures are outlined. Finally the temperature dependence of the square resistance of the superlattice will be presented and compared to the hopping models presented in the previous section.

6.3.1. Samples

The samples on which the temperature-dependent resistance measurements have been performed consist of PbSe nanocrystals (truncated cubes, 5 nm in diameter) that form a superlattice in which the nanocrystals are epitaxially connected. Their room-temperature properties have already been discussed in the previous chapter. The devices presented in this chapter are checked for a clear conduction channel at higher gate voltages (V_G) and the resistance at V_G = 2.0 V is measured. Table 6.2 summarizes the room-temperature four-terminal transport properties of the devices. Five devices were measured; these five devices were part of three chips (A, B and C). The three chips are fabricated using superlattices from three independent synthesis batches.

As in Chapter 5 the carrier density (n) is estimated by photo transient quenching of valence-to-conduction band optical transitions to be 8 electrons per nanocrystal (or, $n = 2.29 \times 10^{13}$ cm^{-2}) at a gate voltage of V_G = 2.0 V. We use this to calculate the mobility, $\mu = \sigma_\square / ne$ with $\sigma_\square = 1/\rho_\square$.

Sample	μ_{RT}(cm^2/Vs)	$\rho_\square$(kΩ/□)
A.1	1.4	200
B.1	9.7	28.0
B.2	1.8	151
C.1	2.2	122
C.3	1.4	188

Table 6.2: Room-temperature four-terminal mobility (μ_{RT}) and square resistance ($\rho_\square$), at V_G = 2.0 V for the devices discussed in this chapter. Note on the labelling: letters (A, B, C) are different chips, from independent syntheses.

6.3.2. Measurement procedures

Before cool-down the samples all have been in high vacuum (10^{-6} mbar) for several days. The gate-voltage of the electrolyte is kept at a particular V_G during cool-down, until the sample has reached a temperature well below the freezing point of the electrolyte (T = 220 K). From this point on, the ionic-liquid gate is frozen at the set potential, notice that the ions defining the Fermi-level on the nanocrystal superlattice are now immobile; the gate voltage can thus be switched off. The

sample is cooled down slowly (less than 1 K per second) above and in a nitrogen bath. The resistance of the sample during cool-down is recorded. After the slow nitrogen cooling through the freezing point of the ionic liquid to the nitrogen base temperature (at T = 77 K) the dip stick is transferred to a helium bath, in which it cools down to the He base temperature of 5 K. After reaching the base temperature He exchange gas is added to promote quicker thermalization of the sample during measurements.

Figure 6.4 shows the cool-down trace of the voltage drop across the inner probes of device B.1 while a current of 1 nA is set over the outer two contacts. This cool-down trace shows an initial increase in conductance (decrease in potential on the probes at set current). Around T = 260 K this increase flattens out. Cooling-down further, the next observation to note is the jumps to lower conductance, like the one seen at T = 210 K. Jumps like this are present in all cool-down traces for all samples. They appear at temperatures near the freezing point of the electrolyte (at T = 220 K). After cooling to well below the freezing point these sudden changes in resistance are not observed any more.

The source of the abrupt jumps in resistance around the freezing point of the ionic liquid is not clear. One interpretation is that the mechanical stresses induced by the solidifying of the ionic liquid locally change the morphology of the nanocrystal superlattice, either near the contacts or in the interior of the sample. Another interpretation could be that reshaping processes of the solidifying electrolyte locally increase the distance from the electrolyte to the superlattice. In the latter interpretation the gating efficiency of the liquid gate locally diminishes, leading to less conductive or insulating patches in the superlattice.

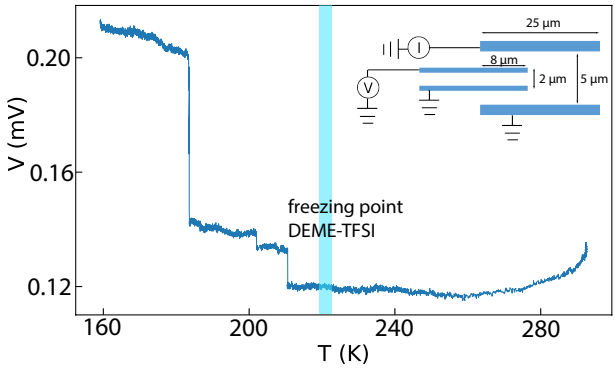

Figure 6.4: Four-probe measurement of the voltage drop across the inner probes during cool-down of a typical sample (B.1), with I = 10 nA. In this temperature range the voltage (resistance) jumps up in steps when cooling down. Inset: sample geometry.

6.3.3. Current-voltage characteristics and contact resistance

The datasets presented in this chapter consist of a series of voltage-current (*IV*) characteristics (for the two-terminal measurements) or a series of current-voltage characteristics (for the four-terminal measurements) measured at different temperatures. A typical set of four-probe *IV*-curves at low-bias between T = 20 K and T = 100 K is shown in figure 6.5 (a). The device is current-biased on the outer source-drain contacts, while the voltage drop across the inner contacts is recorded. The plot shows the forward and backward sweep of the current; only a small hysteresis effect is observed. For this bias between -1 nA and 1 nA, the curves are almost linear. The resistance is deduced by fitting a linear function to the low-bias part of the *IV* (between I = -0.2 nA and I = 0.2 nA) and is plotted as a function of temperature in Fig 6.5 (b).
Figure 6.6 shows the temperature dependence of the resistance of the two-terminal (orange) and four-terminal (blue) measurements of the same device. The two-terminal *IV*-curves are measured over the same two inner contacts by setting a voltage (typically 1 mV) over these contacts while measuring the current. The difference between the resistance of the two data sets is the contact resistance of the device. From Chapter 5 we know that at room temperature the contact resistance is significant in these devices. Figure 6.6 shows that the temperature dependence of the contact resistance is non-linear as it increases in magnitude with decreasing temperature. The two-terminal measurements and their temperature-dependence are thus dominated by the contact resistance in these devices. As four-terminal measurements discard the contact resistance they give access to the conductance properties of the superlattice itself. For this reason, the remainder of this chapter will be focussed on four-terminal measurements.

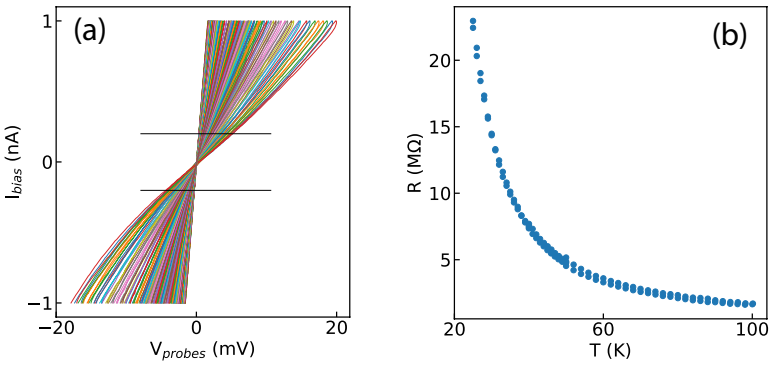

Figure 6.5: (a) Four-probe *IV* curves of device C.1 taken between T = 20 K and T = 100 K at a liquid gate voltage of V_G = 2.3 V. (b) Zero-bias resistance extracted from figure (a) by performing a linear fit through the data between I = -0.2 and +0.2 nA. Both the cooling-down and warming-up trace are plotted.

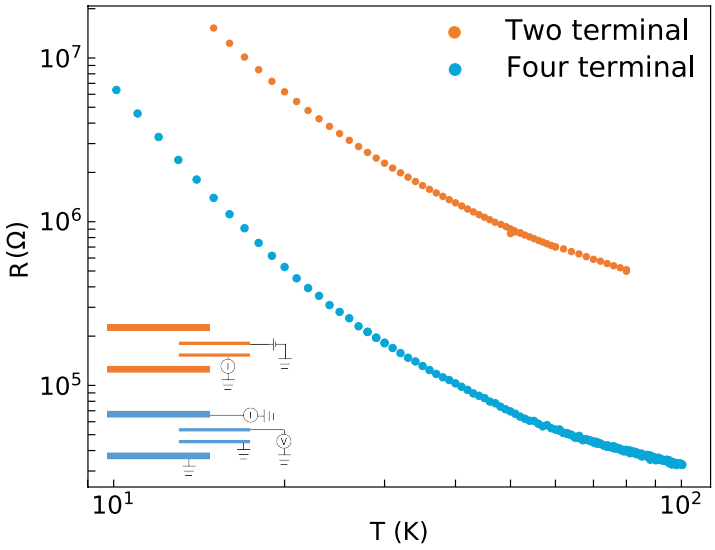

Figure 6.6: Four-terminal and two-terminal low-bias resistance against temperature for sample A.1 at V_G = 2.0 V on a double log scale. Inset: measurement configurations for the two- (orange) and four (blue) terminal measurement. Two terminal measurements are voltage biased; four-terminal measurements are current biased, as indicated by the circuit.

6.3.4. Temperature dependence of the square resistance

Figure 6.7 shows the data collected from the five devices at a gate voltage of V_G = 2.0 V on a double logarithmic scale. The data presented in this figure shows that the four-terminal resistance per square increases by orders of magnitude when cooling down in the temperature range from 100 to 5 K. The largest temperature ranges are present for samples A and B. For sample C the initial resistance (at T = 100 K) is higher than for the other two samples. Moreover the *IV*s of this sample become non-linear at temperatures below T = 60 K. Importantly, despite the high room-temperature mobility (μ >1 $\mathrm{cm^2/Vs}$), the self-assemblies are dominated by a temperature activated conduction mechanism and not by band-type transport. The temperature dependence of the resistance does hold information on the conduction mechanism involved, as discussed in the first part of this chapter. We will use the data from sample A and B to fit different hopping models.

Nearest neighbour hopping (NNH)

If the transport in these assemblies is dominated by hopping processes to the nearest neighbour we expect the square resistance to follow the behaviour as described in equation 6.2. In this case an exponential decay of the resistance is expected with increasing temperature, also known as Arrhenius behaviour. The free parameters

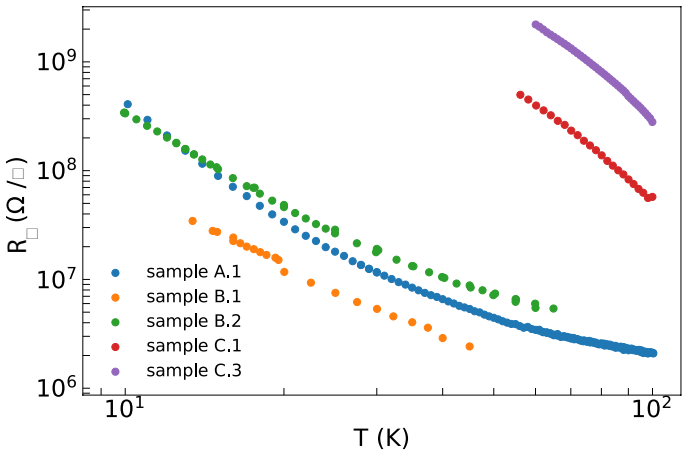

Figure 6.7: Four-terminal resistance per square versus temperature at V_G = 2.0 V on a double log scale for five devices from three samples.

in fitting the data are ρ_0 and the activation energy (E_a).
Figure 6.8 shows the same data as in figure 6.7, but now plotted on a $1/T$ versus ln($G_\square$) scale, to illustrate Arrhenius behaviour. Initially, at higher temperature (between 80 K and 100 K), the datasets follow the exponential behaviour reasonably well, as illustrated by the fits to the data for higher T of device A.1 and B.2. The activation energies (E_0) deduced from the fits are E_0 = 6.7 meV and ρ_0 = 950 kΩ (for device A.1) and E_0 = 6.1 meV and ρ_0 = 1.8 MΩ (for device B.2).
For lower temperatures a significant and increasing deviation from Arrhenius behaviour is observed. This deviation is not uncommon in disordered hopping systems and usually stems from disorder in energy levels of the hopping sites.[24] At low temperature the electron energy ($\propto k_B T$) can drop below the typical energy-level disorder (ΔE) or the charging energy of the nanocrystals ($E_c = \frac{e^2}{2C}$). In this regime the simple picture of electrons hopping to the nearest neighbouring hopping sites breaks down.

Variable range hopping (VRH)

Because NNH breaks down as a model for low-temperature behaviour of the conductivity of the assemblies, attention is turned to the other two hopping models as described in section 6.2.1. Figure 6.9 shows the same data as presented in Fig. 6.8 but now on a 2D VRH-M scale (a), and on a VRH-ES scale (b). The VRH-M plot (a) shows a clear deviation from linear behaviour for higher temperature for both device A.1 (blue) and B.2 (green). In the VRH-ES plot (b), this deviation is reduced, but still present for both devices. In the case of device B.1 the data range available

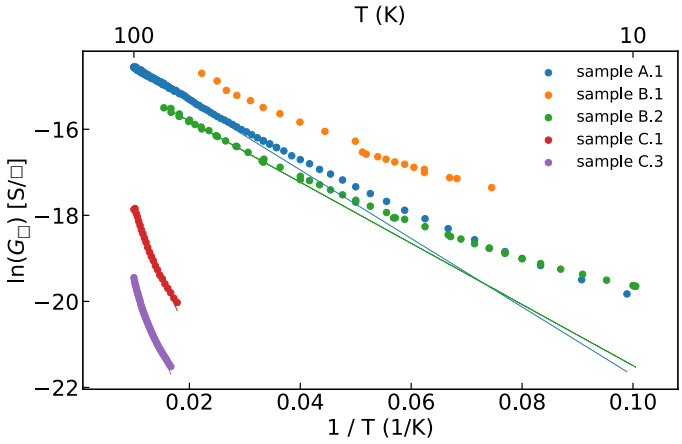

Figure 6.8: Arrhenius plot of the same data as above. Inverse temperature versus four-terminal resistance per square at V_G = 2.0 V . Fits of samples A.1 (blue) and B.2 (green) between 80 K and 100 K show deviation from Arhenius behaviour at lower temperature. The fitting parameters are: $E_{a,A}$ = 6.86 meV, ρ_0 = 948 kΩ (A.1, blue), $E_{a,A}$ = 6.12 meV, ρ_0 = 1.77 MΩ (B.2, green).

is not sufficient to discriminate between the two models. In figure 6.9(b), also the least-square fits over all data points are shown. From these fits the fitting parameters can be deduced, and are given by $E_{a,ES}$=48.1 meV, ρ_0 = 175 kΩ (device A.1, blue), $E_{a,ES}$ = 42.9 meV, ρ_0=316 kΩ (device B.2, green) and $E_{a,ES}$ = 41.5 meV, ρ_0 = 95.9 kΩ (device B.1, orange).
The low-temperature deviation from Arrhenius behaviour (figure 6.8) combined with the high-temperature deviation from VRH models (figure 6.9) is often ascribed to the transition from NNH to VRH, which in our data occurs around 30-50 K.

6.3.5. Gate dependence

For sample C.1 the measurements have been repeated at different gate voltages; the room-temperature transfer characteristics of this sample for high gate values are plotted in Fig. 6.10(a). The data shows an initial increase in square conductance for gate values above V_G = 2.0 V, however, for gate values V_G > 2.4 V the conductance decreases. This peak in conductance could be explained by the completed filling of the p-orbitals of the material, which reduces the amount of free carriers in the system for higher gate voltage. As seen in the optical absorption measurements in Chapter 5 the system is close to complete filling of the p-orbitals at V_G = 2.0 V.
To enable measurements at different gate voltages the sample is briefly warmed up to just above the freezing point of the ionic liquid, enabling turning of the Fermi level in the sample. The gate voltage is set and the sample is cooled-down following

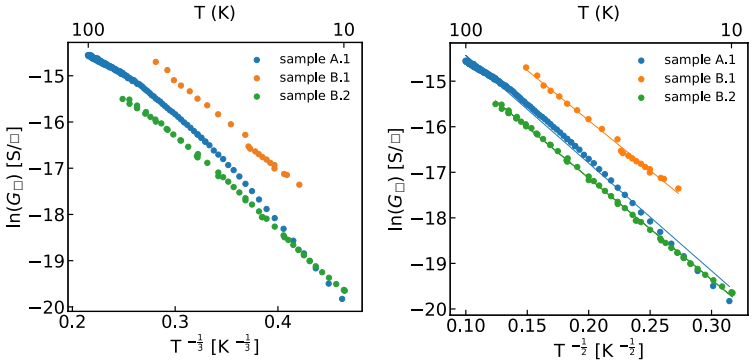

Figure 6.9: Selected data sets plotted on the (a) 2D VRH-Mott scale and (b) VRH-Efros - Shklovskii scale. Fits on the Efros - Shklovskii scale give fitting parameters of: $E_{a,ES}$=48 meV, ρ_0 = 175 kΩ (device A.1, blue), $E_{a,ES}$ = 43 meV, ρ_0=316 kΩ (device B.2, green) and $E_{a,ES}$ = 41 meV, ρ_0 = 95.9 kΩ (device B.1, orange).

	NNH		2D VRH-M		VRH-ES	
V_G (V)	ρ_0 (MΩ/□)	$E_{a,A}$ (meV)	ρ_0 (kΩ/□)	$E_{a,M}$ (meV)	ρ_0 (kΩ/□)	$E_{a,ES}$ (meV)
2.0	1.56	30.8	1.28	10.6	65.5	398
2.3	4.14	10.0	144	0.76	923	60.0
2.5	1.90	15.8	10.3	2.95	140	167

Table 6.3: Fitting parameters for the data presented in Fig. 6.10.

the same procedure as described in Sec. 6.3.2.
Figure 6.10 (b) shows the square conductance as a function of temperature. Interestingly, the data at V_G = 2.3 V show the lowest resistivity values at high temperature and the smallest temperature dependence as illustrated by the lower activation energies for all fitted hopping models of which the fitting parameters are presented in Table 6.3.

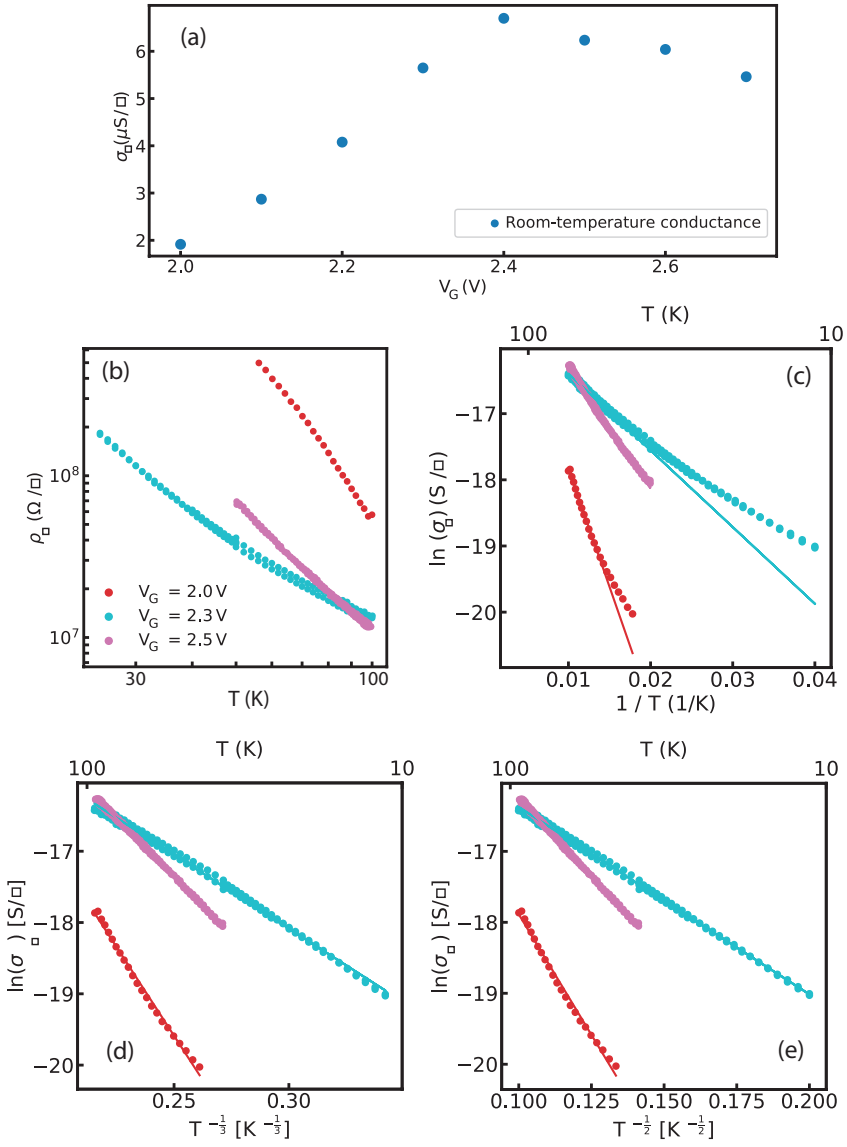

Figure 6.10: (a) Room-temperature square conductivity of sample C.1 for gate values $V_G > 2.0$ V. (b) Square resistivity versus temperature for three different gate values of sample C.1 on a double logarithmic scale. (b,c,d) Analysis of the same datasets as in (b), plotted and fitted to (c) the NNH model, (d) the 2D VRH-Mott model and (e) the VRH-ES model. Deduced fitting parameters (E_a and σ_0) are summarized in Table 6.3.

6.4. Discussion

The data presented in this chapter show clear temperature activated transport in the two-dimensional superlattices at temperatures between 10-100 K. This may be seen as a surprising finding, since the room-temperature mobilities are in the order of 1-10 cm^2/Vs. As summarized in table 6.1 this is the hallmark mobility that in previously reported studies leads to band-type transport ($\frac{d\rho}{dT} > 1$) for three-dimensional QD assemblies.

The measurements presented in this chapter differ from the previous reports in two important ways. First, we have presented measurements on a monolayer of nanocrystals, which poses the question whether transport is 2D or 3D by nature. As described in Section 6.2.2 the metal-to-insulator transition in 2D differs fundamentally from this transition in three dimensions. Most importantly, the square resistivity as a function of carrier density, and not the mobility, is the predicting physical quantity for metallic behaviour at low-temperature. Table 6.2 lists $\rho_\square$ for the presented samples and shows that this quantity is larger than the resistance quantum (ρ_c = 12.9 kΩ) for all samples. For most devices an order of magnitude higher, which indicates that when interpreting the data in a 2D framework the insulating state is not surprising. Moreover, also the gate dependence presented in Section 6.3.5 is consistent with 2D electron transport, as the smallest temperature dependence is observed at a gate value with the highest conductance and highest carrier density.

Secondly, we present data sets at very low temperatures. This is important because the question whether increasing mobility with decreasing temperature ($d\mu/dT < 0$) in a moderate temperature range is a sufficient proof for band-transport in QD superlattices is subject of healthy debate. [25] Indeed, our data shows an initial increase of the conductance when cooling down at moderate temperatures, see Fig. 6.4, while the data at very low temperature (10 K - 100 K) clearly shows temperature activated transport. From the fits of the data to the Arrhenius model we deduced E_a values of 6.1 meV and 6.7 meV. Around room temperature $k_B T$ accedes this energy, which is consistent with the initial metallic-like behaviour at very moderate temperatures. The thermal energy crosses E_a around T ≈ 150 K. This makes our data consistent with the hypothesis that at moderate temperatures QD assemblies can show $d\rho/dT > 0$, despite being dominated by hopping transport at lower temperatures.

6.5. Conclusions

To conclude, the monolayer PbSe nanocrystal superlattices presented in this work show strongly temperature activated transport at temperatures below 100 K. This behaviour is observed in five different devices, part of three independent chips, despite their relatively high room-temperature mobilities, of the order of μ = 1-10 cm^2/Vs. For the lowest temperatures, all devices deviate from the nearest neighbour hopping model and show better fits to variable range hopping models. From tuning the gate voltage in one of the devices we find that the gate value (or, carrier density) showing the highest room-temperature conductivity, shows the smallest temperature dependence (i.e., the smallest activation energy). For band-type transport to be observable in monolayer nanocrystal supperlattices, we conclude that the room-temperature resistance per square has to be at least an order of magnitude lower i.e., approaching the quantum of resistance value of 12.0 kΩ.

Acknowledgements

Synthesis of the nanocrystals and superlattice used for the devices discussed in this chapter has been performed by W.H. Evers.

References

[1] G. A. Ozin, K. Hou, B. V. Lotsch, L. Cademartiri, D. P. Puzzo, F. Scotognella, A. Ghadimi, and J. Thomson, *Nanofabrication by self-assembly,* Materials Today **12**, 12 (2009).

[2] M. Pollak and B. Shklovskii, *Hopping transport in solids*, Vol. 28 (Elsevier, 1991).

[3] C. R. Kagan and C. B. Murray, *Charge transport in strongly coupled quantum dot solids,* Nature nanotechnology **10**, 1013 (2015).

[4] A. Miller and E. Abrahams, *Impurity conduction at low concentrations,* Physical Review **120**, 745 (1960).

[5] N. Mott, *Conduction in non-Crystaline materials* (Oxford science publications, 1993).

[6] A. Efros and B. Shklovskii, *Coulomb gap and low temperature conductivity of disordered systems,* Journal of Physics C: Solid State Physics **8**, L49 (1975).

[7] N. Apsley and H. Hughes, *Temperature-and field-dependence of hopping conduction in disordered systems, ii,* Philosophical Magazine **31**, 1327 (1975).

[8] D. Yu, C. Wang, B. L. Wehrenberg, and P. Guyot-Sionnest, *Variable range hopping conduction in semiconductor nanocrystal solids,* Physical review letters **92**, 216802 (2004).

[9] S. Kravchenko and M. Sarachik, *Metal–insulator transition in two-dimensional electron systems,* Reports on Progress in Physics **67**, 1 (2003).

[10] S. V. Kravchenko, G. Kravchenko, J. Furneaux, V. M. Pudalov, and M. d'Iorio, *Possible metal-insulator transition at b= 0 in two dimensions,* Physical Review B **50**, 8039 (1994).

[11] D. Popovic, A. Fowler, and S. Washburn, *Metal-insulator transition in two dimensions: Effects of disorder and magnetic field,* Physical review letters **79**, 1543 (1997).

[12] B. Radisavljevic and A. Kis, *Mobility engineering and a metal-insulator transition in monolayer MoS_2.* Nature Materials **12** (2013).

[13] A. Ioffe, *Af ioffe and ar regel, prog. semicond. 4, 237 (1960).* Prog. Semicond. **4**, 237 (1960).

[14] A. P. Alivisatos, *Semiconductor clusters, nanocrystals, and quantum dots,* science **271**, 933 (1996).

[15] R. L. Whetten, J. T. Khoury, M. M. Alvarez, S. Murthy, I. Vezmar, Z. Wang, P. W. Stephens, C. L. Cleveland, W. Luedtke, and U. Landman, *Nanocrystal gold molecules,* Advanced materials **8**, 428 (1996).

[16] C. Murray, C. Kagan, and M. Bawendi, *Self-organization of CdSe nanocrystallites into three-dimensional quantum dot superlattices,* Science **270**, 1335 (1995).

[17] C. B. Murray, a. C. Kagan, and M. Bawendi, *Synthesis and characterization of monodisperse nanocrystals and close-packed nanocrystal assemblies,* Annual Review of Materials Science **30**, 545 (2000).

[18] D. V. Talapin and C. B. Murray, *PbSe nanocrystal solids for n-and p-channel thin film field-effect transistors,* Science **310**, 86 (2005).

[19] D. Ginger and N. Greenham, *Charge injection and transport in films of CdSe nanocrystals,* Journal of Applied Physics **87**, 1361 (2000).

[20] D. Yu, C. Wang, and P. Guyot-Sionnest, *n-Type conducting CdSe nanocrystal solids,* Science **300**, 1277 (2003).

[21] J. S. Lee, M. V. Kovalenko, J. Huang, D. S. Chung, and D. V. Talapin, *Band-like transport, high electron mobility and high photoconductivity in all-inorganic nanocrystal arrays,* Nature nanotechnology **6**, 348 (2011).

[22] J. H. Choi, A. T. Fafarman, S. J. Oh, D. K. Ko, D. K. Kim, B. T. Diroll, S. Muramoto, J. G. Gillen, C. B. Murray, and C. R. Kagan, *Bandlike transport in strongly coupled and doped quantum dot solids: a route to high-performance thin-film electronics,* Nano letters **12**, 2631 (2012).

[23] S. J. Oh, Z. Wang, N. E. Berry, J.-H. Choi, T. Zhao, E. A. Gaulding, T. Paik, Y. Lai, C. B. Murray, and C. R. Kagan, *Engineering charge injection and charge transport for high performance PbSe nanocrystal thin film devices and circuits,* Nano letters **14**, 6210 (2014).

[24] H. Liu, A. Pourret, and P. Guyot-Sionnest, *Mott and Efros-Shklovskii variable range hopping in CdSe quantum dots films,* Acs Nano **4**, 5211 (2010).

[25] P. Guyot-Sionnest, *Electrical transport in colloidal quantum dot films,* The Journal of Physical Chemistry Letters **3**, 1169 (2012).

A

Scanning μLEED: Comparison of data analysis techniques

In this appendix we will compare the two data analysis methods used in chapter 3.

A.1. On the origin of errors

Figure A.1 (a) shows the data as presented in chapter 3 of the small-scale data set. In this figure the first order spot detection is plotted against the Moiré radius detection. The figure shows that for most of the points (96%) the two analysis techniques yield the same result within a 3° accuracy. However, there are two small clusters that are not on the x=y line. Moreover, at high angles there is a small offset from the x=y line. We will discuss the cause of these mismatches next. First we we will focus our attention to the data points that do not match between the two methods, in figure A.1 (a) these points are coloured in green. These points are spread in two clusters at large angles compared to the 0° copper spot. In figure A.1 (b) the spatial locations of these points are indicated in green. It can be seen that these points are located at the boundary between two areas of graphene with a different crystalline orientation. We also observe that the two analysis methods pick up the angle that corresponds to either one of the areas.
The mismatch between the detected angles is caused by the two graphene orientations being present in the area that is probed. The points are located in the boundary between two areas. In some cases both of these orientations are picked up by the detection methods and in some cases either one of the orientations is picked up. Especially the Moire detection prefers smaller angles (compared to the copper spot).

Second, we look at the slight offset of the clusters of points at larger angles. This small offset is caused by the deformations in the Ewald sphere present in the alignment of the system. Far from the optical axis the diffraction plane shows clear signs of deformations and this causes small errors in the first order spot detection for materials with a small unit cell, like graphene.
In the next section we will focus our attention to the accuracy in the data points that match between the two methods.

A.2. Estimate of accuracy

To estimate the accuracy of the data analysis we will look at the vast majority of the data points in the small scale data set that do cluster along the x=y line. For this analysis we will assume that the different clusters of points stem from graphene areas with the same orientation, per cluster.
To analyse the external error we look at the deviations within the matching clusters. We collapse the three different clusters of points on the same origin by subtracting the clusters average.
Figure A.1 (c) shows the resulting 2D-histogram. In this histogram we observe that there is a small, weakly anisotropic spread present. The estimated external error is .75°.

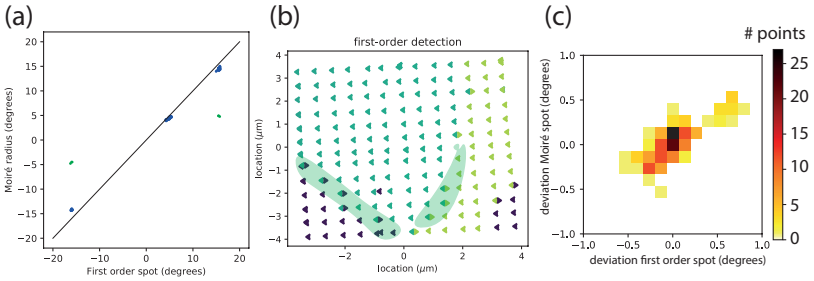

Figure A.1: A figure on the graphene angle detection error. (a) Small scale dataset first order detection versus Moiré angle detection. In green the mismatching points are indicated. (b) Spatial location of the detected angles for the firt order detection. In green the typical location of the green points in figure (a) are indicated. (c) 2D-histogram of the deviation from the average of the three matching clusters in figure (a).

B

3D-ARRES: data filtering

B.1. Origin of fluctuations

In the 3D-ARRES data sets, the intensity for every frame (i.e., energy value) shows abrupt fluctuations. These abrupt fluctuations are not a material property, as the energy values at which they occur change from measurement to measurement. They are also visible in other (spectroscopic) measurements. Because the frame-to-frame fluctuations in electron intensity obscure the band diagram plots, it is important to correct for them.
The cause of the intensity fluctuations is not perfectly clear. They are suspected to be caused by variations in the electron gun. These variations in the gun cause low-frequency dose fluctuations, leading to fluctuations from image to image.
The electron current emitted by the electron gun is currently not measured in our system, making it impossible to directly correct for this quantity. To get rid of the fluctuations present in the data we use a data filtering protocol after the experiment, that will be described in the next section.

B.2. Data filtering: MoS_2 and hBN

Figures B.1 and B.2 (a) show band diagram plots of the raw data over the high symmetry axes. The frame-to-frame fluctuations are seen in the horizontal lines running over the full energy range.
Because the fluctuations are frame-to-frame, the correction will also be determined per frame, i.e., per energy value. For this, first the mean intensity (MI) for each

row in the band diagram is calculated:

$$\langle I\rangle_k(E) = \frac{1}{n}\sum_{k_i=0}^{n} \mathrm{I}_{k_i}(\mathrm{E}), \tag{B.1}$$

where k_i is the i^{th} pixel column of the measured $\mathbf{k}_\parallel$ values. The mean intensity for the band diagrams in figure B.1 and B.2(a) are plotted in figures B.1 and B.2 (b) in blue. In this plots the fluctuations are clearly visible.
In the next step of this protocol the mean intensity in figures B.1 and B.2 (b) is filtered using a Gaussian filter with a σ= 0.5 eV (in these cases 5 data points). The filtered graph is plotted in orange. The deviation of the raw data from the filtered data is used as a correction factor:

$$\mathrm{C(E)} = \frac{\langle I_{\mathrm{smooth}}\rangle_k(\mathrm{E})}{\langle I_{\mathrm{raw}}\rangle_k(\mathrm{E})}. \tag{B.2}$$

This correction factor is now used to smoothen the data row-wise, where the filtered intensity is given by:

$$\mathrm{I}_{\mathrm{filtered}}(\mathbf{k}_\parallel, \mathrm{E}) = \mathrm{C(E)}\mathrm{I}_{\mathrm{raw}}(\mathbf{k}_\parallel, \mathrm{E}). \tag{B.3}$$

The result of this protocol is plotted in the band diagram of figures B.1 and B.2 (c) and in the figures in the main text. In the filtered data, the sharp horizontal fluctuations are removed and the band diagram features are more clearly visible.

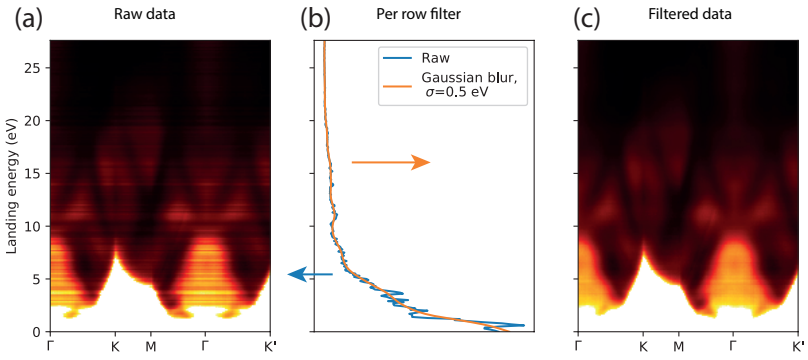

Figure B.1: 3DARRES MoS_2.

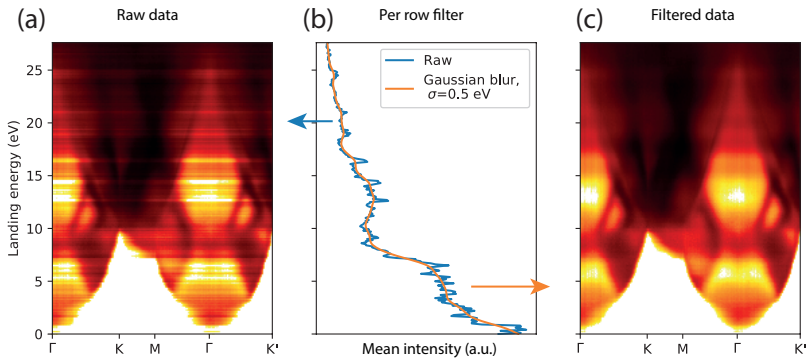

Figure B.2: 3DARRES hBN.

C

3D-ARRES: electronics

In this appendix the specifics of the electronics used to enable the 3D-ARRES measurements are presented. As explained in the main text the electronics are designed in-house. The main stability demands on the circuits are: (1) the speed at which the deflector can be scanned, or driven should be 100 kHz, and (2) the output current should be bipolar and have the option to reach $\pm$100 mA. The chosen design is based on the improved Howland circuit.

C.1. Layout of the electronics

Figure C.1 shows the schematics of the circuits used to supply the deflector coils with the desired current. The input voltage (V3) is supplied by the DAQ (*Multifunction Measurement and Control* USB-2637 DAQ), which supplies voltages from two independent channels to the circuit boards for the x direction (a) and the y direction (b) of deflector 1.

The deflector coils can be found at the output of the circuit, : Defl1-x (a) and Defl1-y (b). The two coils differ in impedance and therefore need different input voltages ($V_{\text{out-coil}}$) for the same amount of current in the coil. This is the reason for slightly different circuits for both coils.

The circuit is based on the improved Howland circuit. This circuit was chosen for high output voltages in combination with stability up to the desired frequencies. At the heart of this circuit the so-called opa548 amplifier was used, to allow high enough output voltages and bipolar operation.

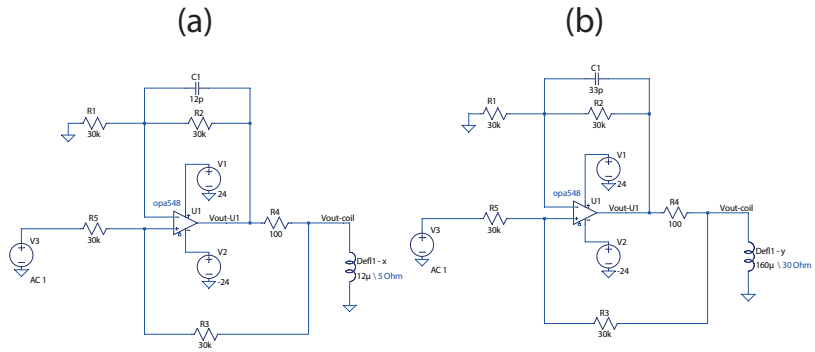

Figure C.1: Schematics of the electronics used to operate the deflector in the 3D-ARRES measurements.

C.2. Simulated performance of the electrons

Next the stability of the circuit is modelled. Figure C.2 shows the results of the simulation. The transfer curves indicate a constant and reliable output up to 100 kHz for both circuits, and an even higher stable output, up to 1 MHz for Delf1-x. The limiting factor in the maximum frequency is the coils impedance.
The simulations indicate that the circuits work up to specs. The measurements in the main text confirm this indication.

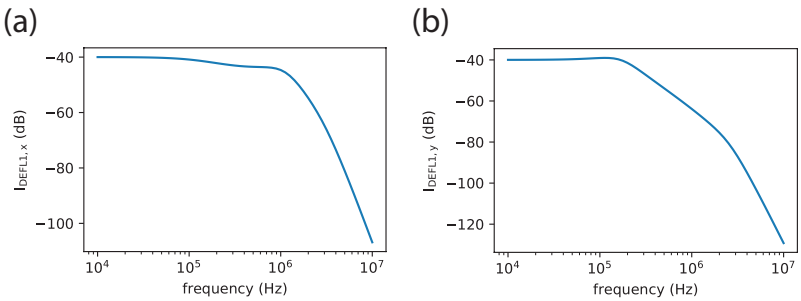

Figure C.2: Modelled transfer function of the circuits presented in figure C.1. (a) The deflector 1 coils in the x direction are stable up to a driving frequency of about 1 MHz. (b) The deflector 1 coils in the y direction are stable up to a driving frequency of about 100 kHz.

Acknowledgements

First I would like to thank the people that have played a supervisory and guiding role in the work leading to this thesis, starting with my promotors. In Delft, Herre van der Zant supervised the work on nanocrystal superlattices as described in Chapters 5 and 6. I am grateful for Sense Jan van der Molens trust, taking me into his group in Leiden and allowing me to work on his beloved Low Energy Electron Microscope (LEEM). His scientific and personal guidance kept me on track more than once.
The LEEM chapters wouldn't have been in this thesis without Johannes Jobst. He was responsible for most of the scientific guidance on the LEEM chapters (Chapters 2 to 4). His inspiring hands-on leadership guided me and helped me to push through. The scientific advise of Ruud Tromp on Chapters 2 to 4 was essential. The depth of highly specialized knowledge and experience combined with patience significantly elevated these chapters.
The high-level work on an instrument like the LEEM is a true team effort. And what a team the Leiden LEEM has! It has been an incredible experience to be part of this team of highly skilled people building and maintaining a world class facility.
I am very grateful for the possibility to work with Tobias de Jong. We were an extremely diverse team of two. I enjoyed our close collaboration, in which we could combine and give space to our very different skill sets and styles. I am indebted for all the Python help along the way, the scientific discussions and the excellent LEEM skills.
Marcel Hesselberth is the technical memory and continuity of the LEEM set-up. He brings together a rare combination of technical skill, scientific experience and teaching skills. Besides being indispensable for keeping the LEEM running, both on a daily basis and long-term, Marcel has contributed to Chapter 4 with his electronic knowledge and advice.
The Leiden Institute of Physics wouldn't be the same without the exceptional fine mechanic and electronic support. Two people are of special importance to this thesis. First, Ruud van Egmond, our specialist in *Fine* mechanical support. Second, René Overgauw who built and co-designed the electronics for the 3D-ARRES technique developed in Chapter 4. The strength of this support is both in the extreme technical skill and the ability to listen, understand and think along. More than once this resulted in a better, but very different, solution than anticipated. Additionally the technical support of Douwe Scholma and the excellent administrative and moral support of Ellie van Rijsewijk were indispensable.
I have had the chance to work with exceptional students: many thanks to Arjo Andringa, Dennis Uitenbroek and Renée van Limpt!

At the basis of Chapters 5 and 6 are the PbSe nanocrystal supperlattices, skillfully

synthesized by Wiel Evers. Besides synthesis, his wide knowledge on these systems were extremely important to the realization of this work.
Michele Buscema introduced me to clean room techniques and (2D material) device fabrication. He showed me that this work is part technical skill, part mindset. Michele also showed me operation and the measurement techniques in Chapter 5. Alexandra Fursina was responsible for the teaching of the low-temperature transport research used in Chapter 6. Nikos Papadopoulos became the 2D-material device fabrication specialist in Delft. I have enjoyed the discussions on research lines and fabrication techniques.
Some of the most important pillars in a scientific department can be found in the technical and administrative support. For technical support I am thankful to Mascha van Oossanen in the MED times and Tino Kool at the QN department. The Kavli support staff had the clean room equipment running non-stop, their dedication to this environment makes the Kavli clean room such an amazing place to work. Much needed administrative support was taken care of by Maria Roodenburg en Heleen Woldhuis.
Chapters 5 and 6 are the result of a close collaboration with the group of Daniël Vanmaekelbergh at the Debye Institute in Utrecht. Together with Maryam Alimoradi Jazi I worked on Chapter 5 and the paper that was published about this work. Additionally, the meetings with the consortium were a very inspiring contribution to this work.

Tot slot wil ik allereerst Jelmer bedanken voor zijn onuitputtende steun in de totstandkoming van dit proefschrift. Zonder hem was dit werk niet mogelijk geweest. Daarnaast heeft mijn broer, Guus, mij enorm gemotiveerd door te zetten; over een finishlijn in Oudenaarde en alles dat daarna kwam. Thérèse heeft basis gelegd voor dit werk met haar doortastendheid in het repeteren van de tafels en haar liefdevolle betrokkenheid bij een groot deel van mij jeugd. Bovenal hebben mijn ouders mij met volle overtuiging gesteund. Hun onuitputtende vertrouwen heeft hiertoe geleid en daar ben ik dankbaar voor.

Curriculum Vitæ

Vera Apolonia Emerentiana Clara Janssen

08-04-1989 Born in Papendrecht, the Netherlands.

Education

2001–2007 High school: De Lage Waard, Papendrecht

2007–2012 BSc. in Physics *Leiden University*
Thesis: *"Self assembled monolayers on extremely thin gold layers"*
Supervisor: Prof. dr. ir. S.J. van der Molen

2012–2014 MSc. Physics *Leiden University*

Thesis: *"Experimental observation of quadrupolar rearrangements in a 2D disordered foam"*
Supervisor: Prof. M. van Hecke

Thesis: *"Signatures of quantum interference in the transport through π-π stacked molecules"*
Supervisor: Prof. dr. ir. H.S.J. van der Zant

List of Publications

4. B.A.E. Lehner, **V.A.E.C. Janssen**, E.M. Spiesz, D. Benz, S.J.J. Brouns, A.S. Meyer, H.S.J. van der Zant, *Creation of Conductive Graphene Materials by Bacterial Reduction Using Shewanella Oneidensis*, ChemistryOpen **8**, 2019.

3. M. Alimoradi Jazi, **V.A.E.C. Janssen**, W.H. Evers, A. Tadjine, C. Delerue, L.D.A. Siebbeles, H.S.J. van der Zant, A.J. Houtepen, and D. Vanmaekelbergh, *Transport properties of a two-dimensional PbSe square superstructure in an electrolyte-gated transistor*, Nano Letters **17**, 2017.

2. R. Frisenda, **V.A.E.C. Janssen**, F.C. Grozema, H.S.J. van der Zant, N. Renaud, *Mechanically controlled quantum interference in individual π-stacked dimers*, Nature Chem **8**, 2016.

1. J. Kautz, **V.A.E.C. Janssen**, R.M. Tromp, S.J. van der Molen, *Differential reactivity of alkanethiols with Si (111)–Au 2D surface alloys*, Surface Science **632**, 2015.